TECTONIC PROCESSES AND CONTINENTAL HYDROCLIMATE DURING THE LARAMIDE DEFORMATION IN THE CENTRAL ROCKY MOUNTAINS

by

MIN GAO

Presented to the Faculty of the Graduate School of

The University of Texas at Arlington in Partial Fulfillment

of the Requirements

for the Degree of

DOCTOR OF PHILOSOPHY

THE UNIVERSITY OF TEXAS AT ARLINGTON

May 2017

Acknowledgements

I would first like to express my deep appreciation to Dr. Majie Fan for her continual guidance and support throughout the course of my research and the preparation of my dissertation. I appreciate the great amount of time and patience that Dr. Fan has put on teaching me field geology and lab techniques, inspiring my research thoughts, and helping me improve writing. I would also like to thank the members of my dissertation committee, Drs. Asish R. Basu, Elizabeth M. Griffith, William A. Griffith, and James P. Grover, for their time, comments, and guidance throughout the preparation and review of this dissertation.

A special thanks is extended to Dr. Robert Moucha for his contribution and helpful discussion in the first chapter. Special thanks also goes to Patricia Garay, Jackie Garcia and Lu Zhu for their great help in the field or in the laboratory. Great thanks to my parents, Kehong Zhao and Mingqian Gao, my sister, Jing Gao, and my best friend, Longfei Wu for supporting and encouraging. I also wish to thank Lu Zhu, Junjie He, Mingjia Ma, Jenna West, Ohood Al Salem and Zhiye Gao for being good friends and great support during my time at the University of Texas at Arlington.

This research was supported by grant PRF–54673–DNI8, a UTA research enhanced grant, and two Geological Society of America student research grants.

April 17, 2017

Abstract

TECTONIC PROCESSES AND CONTINENTAL HYDROCLIMATE DURING THE LARAMIDE DEFORMATION IN THE CENTRAL ROCKY MOUNTAINS

Min Gao, PhD

The University of Texas at Arlington, 2017

Supervising Professor: Majie Fan

The central Rocky Mountains in western U.S.A. is a geologic province formed by the low-angle subduction of the Farallon oceanic plate under the North American continental plate during the latest Cretaceous–early Eocene Laramide orogeny. The tectonic processes and mechanism, the paleotopography and depositional environment, and the evolution of continental hydroclimate during the Laramide deformation remain controversial. This dissertation examines the tectonic processes of the Laramide orogeny throughout the entire central Rocky Mountains, and paleotopography, depositional processes, and paleoclimate in the Greater Green River Basin in southwestern Wyoming. The first project of this study uses a 2D flexural subsidence modeling method to explore the mechanism that links the surface deformation pattern to deep mantle processes during the Laramide deformation. The stiffness of Wyoming lithosphere decreased spatially

from northeastern Wyoming (T_e=32–46 km) to southwestern Wyoming (T_e=6–9 km), while varied slightly in each basin during the ~30 Myr duration of the Laramide deformation. We attribute this southwestward weakening pattern to bending stresses, crust–mantle decoupling and end load effect. We also suggest a two-stage Laramide deformation based on the accelerated uplift of Laramide mountains during the early Eocene. The second project combines lithofacies analysis, sandstone petrography and oxygen isotope paleoaltimetry to examine the depositional environment, sediment provenance, and paleotopography of the early Paleogene Greater Green River Basin, southwestern Wyoming. The reconstructed paleoelevation of the Uinta Mountains to the south of the Greater Green River Basin was at least 3.5 km during the earliest Eocene. Surface uplift of the Uinta Mountains during the earliest Eocene resulted in changes in drainage pattern, depositional environment and sediment sources in the Greater Green River Basin. The third project uses multiple climate proxies including bulk organic carbon isotope record ($\delta^{13}C_{org}$), paleosol morphology, atmospheric CO_2 concentration (pCO_2) and mean annual precipitation (MAP) to study the continental hydroclimate characteristics in the Greater Green River Basin during the late Paleocene-early Eocene. Two negative $\delta^{13}C_{org}$ excursions were recognized, representing two early Paleogene hyperthermals: PETM and ETM-2. The climate in the basin was generally warm and humid during late Paleocene-early Eocene, but transient drying occurred during the extreme hot hyperthermals.

Table of Contents

List of Figures

List of Tables

Chapter 1 Introduction

The high–elevation, high–relief central Rocky Mountains (Rockies) in Wyoming and nearby areas in western U.S.A. is a region of Precambrian basement-cored uplifts and intervening sedimentary basins that developed during late Cretaceous–Eocene time as a result of crustal shortening and mantle dynamic processes (e.g., Dickinson and Snyder, 1978; Liu et al., 2008; Liu et al., 2010; Jones et al., 2011; Fan and Carrapa, 2014). Modern average elevation of the central Rockies is ~1.5 km, and the high mountains reach ~4 km. The region was a near–sea level continental–scale foreland basin that developed east of the North America Cordilleran thrust belt during the Late Cretaceous, and the basin was ~1000–1500 km inland from the subduction zone. The region was then partitioned into a system of basement–cored mountain ranges and intervening sedimentary basins by the subsequent Laramide orogeny during the latest Cretaceous–early Eocene (e.g., Dickinson and Snyder, 1978; Dickinson et al., 1988). Current understanding of the uplift history of the central Rockies is that the Laramide orogeny produced most of the topography, and post-Laramide subsidence, erosion and surface uplift have modified the topography to the present state (e.g., Dickinson et al., 1988; McMillan et al., 2002, 2006; Liu and Gurnis, 2010; Duller et al., 2012; Roberts et al., 2012).

The mechanism of crustal deformation in response to deep mantle processes during the ~30 Myr period of the Laramide orogeny remains enigmatic (e.g., Bird,

1988; DeCelles, 2004; Liu et al., 2008; Jones et al., 2011; Fan and Carrapa, 2014), although the low–angle subduction of the Farallon oceanic plate beneath the North American continental plate has been generally accepted as the driving force of the Laramide deformation (e.g., Livaccari et al., 1981; Tarduno et al., 1985; Liu et al., 2008; Liu et al., 2010; Jones et al., 2011). Current geodynamic hypotheses that link the surface deformation in the central Rockies and the low–angle subduction of the Farallon plate can be broadly categorized into crustal shortening and thickening induced by low–angle subduction (e.g., Bird, 1988; Livaccari, 1991; Jones et al., 1998; 2011), dynamic and isostatic responses to the removal of Farallon flat slab and/or the eclogitized oceanic plateau (e.g., Liu et al., 2008; Liu et al., 2010), or the combination of the two (Fan and Carrapa, 2014). Evaluation of these hypotheses and further understanding of the deformation mechanism require a large regional database of the timing of individual Laramide uplifts, their paleoelevation evolution histories, and the temporal and spatial deformation patterns in the region. In this dissertation, I examine the temporal and spatial deformation patterns in the central Rocky Mountains during the Laramide deformation by conducting 2D flexural subsidence modeling to the Laramide intermontane basins (Chapter 2); and study the timing and process of surface uplift of the Laramide Uinta Mountains using oxygen isotope paleoaltimetry combined with the evolution of depositional

environment and sediment provenance of the Greater Green River Basin, which is bounded by the Uinta Mountains to the south (Chapter 3).

The last portion of the Laramide orogeny occurred when the Earth was in the last greenhouse during the late Paleocene–early Eocene (LPEE, 59–50 Ma), therefore the sedimentary records in the Laramide intermontane basins archive the continental hydroclimate during this global warming. The warm LPEE climate is well expressed in high-resolution benthic foraminifera oxygen isotope records, which show that ocean bottom temperature increased ~4-6 °C during the period and another ~4 °C during the short-termed Paleocene–Eocene Thermal Maximum (PETM) (e.g., Zachos et al., 2001). However, the responses of continental climate and environment to the global warming during the LPEE remain poorly understood, in part, due to the lack of high-resolution, continuous record in continental interiors. Although many previous studies have suggested that the warm LPEE climate was associated with high atmospheric pCO_2, the magnitude of pCO_2 is still debated (e.g., Sinha and Stott 1994; Hyland et al., 2013). Previous studies also have not reached agreement on whether continental hydroclimate became wetter or drier during the extreme warm periods in the LPEE, such as the PETM (e.g., Robert and Kennett, 1994; Schmitz and Pujalte, 2003; Kraus et al., 2013). In Chapter 4 of this dissertation, I build a long and continuous bulk organic carbon isotope record for the LPEE in the Greater Green River Basin; determine the wet/dry conditions based on paleosol morphology and CIA-K proxy; and

reconstruct the atmospheric pCO_2 using the carbon isotope compositions of paleosol carbonates and accompanied organic materials.

Chapters 2-4 of this dissertation include one published paper and two manuscripts in different stages of publication.

Chapter 2, *Southwestward Weakening of Wyoming Lithosphere during the Laramide Orogeny*, presents the temporal and spatial variations of the stiffness of Wyoming lithosphere and uplift of Laramide ranges by conducting 2D flexural subsidence modeling to the four Laramide intermontane basins. We followed the standard procedure of 2D flexural subsidence modeling of foreland basins (e.g., Jordan, 1981; Turcotte and Schubert, 1982; Watts, 1992) and modeled the mountain load height and lithospheric stiffness by matching the modeled 2D subsidence profiles with the observed 2D subsidence profiles recorded in isopach maps. We documented a southwestward weakening pattern of Wyoming lithosphere during the Laramide deformation, and attributed the causes to the combined effect of the bending stresses induced by the topographic load of the Sevier fold–and–thrust belt, the crust–mantle decoupling initiated by the overthickened Sevier hinterland, and the end loads due to the low–angle subduction at the western edge of the thick Wyoming craton. The results support a two-stage Laramide deformation model that horizontal compressional stresses caused intraplate crustal deformation during the latest Cretaceous–Paleocene, and rollback of the Farallon flat slab caused accelerated surface uplift by dynamic and

isostatic processes during the early Eocene. This work has been published in *Journal of Geophysical Research-Solid Earth*.

Chapter 3, *Depositional Environment, Sediment Provenance and Oxygen Isotope Paleoaltimetry of the Early Paleogene Greater Green River Basin, Southwestern Wyoming, U.S.A.*, examines the evolution of depositional environments, drainage patterns, and elevation of the surrounding mountains in the southern part of the Greater Green River Basin during the coeval Laramide and Sevier deformations. A ~1400 m thick continuous stratigraphic section covering the Paleocene-early Eocene was carefully described in the field. Our detailed lithofacies description and interpretation, sediment provenance study based on sandstone petrography and paleocurrent direction data suggest that the depositional environment changed from low-energy distal floodplain of a meandering river to high-energy braided rivers originated from the Uinta Mountains to the south of the basin. Based on our results of oxygen isotope compositions of fluvial carbonate cement and pedogenic carbonates, we suggest that the Uinta Mountains started to gain elevation during the latest Paleocene, and reached an elevation of at least 3.5 km high during the earliest Eocene. This manuscript has been submitted to *American Journal of Science*.

Chapter 4, *Continental Hydroclimate during the Late Paleocene–Early Eocene Greenhouse in the Greater Green River Basin, Southwestern Wyoming, U.S.A.*, presents high-resolution, continuous bulk organic carbon isotope

composition, paleosol morphology and chemical index of alteration (CIA-K) records documenting the changes in continental hydroclimate during the LPEE. The PETM was identified in our section as a ~4 ‰ negative Carbon Isotope Excursion (CIE) spanning ~70 m at the Paleocene-Eocene boundary. Stratigraphically above the PETM, another ~2 ‰ CIE spanning ~100 m was identified, which most likely represents the earliest Eocene with several post-PETM hyperthemal events, such as ETM–2 at ~53.6 Ma, I-1 at ~53.3 Ma, and I-2 at ~53.2 Ma (e.g., Cramer et al., 2003; Lourens et al., 2005). Our paleosol morphology study shows that water-logged histosols and poorly drained green paleosols were developed most of the time, while well drained red-brown paleosols and carbonate-rich calcisols developed during the hyperthermals. Reconstructed mean annual precipitation (MAP) amount varied from 400 to 1600 mm, with lower values (<800 mm) occurred during the hyperthermals. Our reconstructed pCO_2 based on the carbon isotope compositions of paleosol carbonates and accompanied organic materials within the PETM is generally in the range of 600-1200 ppm, which is 2-3 times higher than preindustrial. The results suggest that the climate was generally humid and warm during the LPEE in southwestern Wyoming, but transient dry conditions were prevalent during the extreme warm hyperthermals. This manuscript is currently in preparation.

Chapter 2 Southwestward weakening of Wyoming lithosphere during the Laramide orogeny

Abstract

The mechanism of Laramide deformation in the central Rocky Mountains remains enigmatic. It is generally agreed that the deformation resulted from low–angle subduction of the Farallon plate beneath the North American plate during the latest Cretaceous–early Eocene, however, recent studies have suggested the importance of slab removal or slab rollback in causing this deformation. Here we infer Wyoming lithosphere structure and surface deformation pattern by conducting 2D flexural subsidence modeling in order to provide constraints on the mechanism of Laramide deformation. We assume that Wyoming lithosphere behaved as an infinite elastic plate subject to tectonic loading of mountain ranges, and conduct 2D flexural subsidence modeling to major Laramide basins to document lithospheric stiffness and mountain load height. Our results show that the stiffness of Wyoming lithosphere varied slightly in each basin during the ~30 Myr duration of the Laramide deformation, and decreased from northeastern Wyoming (T_e=32–46 km) to southwestern Wyoming (T_e=6–9 km). Our results also imply that the increase of equivalent load height of major Laramide ranges accelerated during the early Eocene. We propose that the bending stresses induced by the topographic load of the Sevier fold–and–thrust belt combined with crust–mantle decoupling initiated by the overthickened Sevier hinterland and the end loads due to the low angle subduction at the western edge of the thick Wyoming craton, have caused the southwestward decrease of lithospheric stiffness in

Wyoming. Moreover, we attribute the accelerated load height gain during the early Eocene to both dynamic and isostatic effects associated with slab rollback.

Keywords: 2D flexural subsidence; lithospheric stiffness; load height; Laramide deformation; low angle subduction; slab rollback

2.1 Introduction

The high–elevation, high–relief topography of the central Rocky Mountains (Rockies) in Wyoming and its nearby area in western U.S.A. is a result of crustal shortening and mantle dynamic processes [e.g., Dickinson and Snyder, 1978; Liu et al., 2008; Liu et al., 2010; Jones et al., 2011; Fan and Carrapa, 2014] (Figure 2-1). This region was situated in the Sevier foreland and near sea level during the Late Cretaceous, and then was partitioned into a system of basement–cored mountain ranges and intervening sedimentary basins by the subsequent Laramide orogeny in latest Cretaceous–early Eocene [Dickinson and Snyder, 1978; Dickinson et al., 1988]. Although it is generally accepted that the Laramide orogeny was driven by the low–angle subduction of the Farallon plate beneath western U.S.A. [e.g., Livaccari et al., 1981; Tarduno et al., 1985; Liu et al., 2008; Liu et al., 2010; Jones et al., 2011], the mechanism of crustal deformation in response to the low–angle subduction during this ~30 Myr period remains enigmatic [e.g., Bird, 1988; DeCelles, 2004; Liu et al., 2008; Jones et al., 2011; Fan and Carrapa, 2014].

Geodynamic hypotheses that link surface deformation and low–angle subduction of the Farallon plate in the central Rockies can be broadly categorized into two distinct mechanisms, including crustal shortening and thickening induced by low–angle subduction [e.g., Bird, 1988; Livaccari, 1991; Jones et al., 1998; 2011], and dynamic and isostatic responses to the removal of Farallon flat slab and/or the eclogitized oceanic plateau [e.g., Liu et al., 2008; Liu et al., 2010; Fan and Carrapa, 2014]. In support of the first mechanism, Bird [1988] and Livaccari [1991] attributed the stress that caused the crustal deformation to basal tractions at the base of the Wyoming lithosphere; Jones et al. [1998; 2011] proposed that the basal traction force was augmented by increased deviatoric horizontal stresses in the continental lithosphere as a result of "suction" between the flat slab and the Archean Wyoming lithosphere keel; McQuarrie and Chase [2000] speculated that mid–crustal ductile flow from the Sevier hinterland caused isostatic uplift of the Colorado Plateau and its surrounding Rockies. Advocating for the second mechanism, recent inverse mantle convection modeling suggests that the Laramide deformation resulted from the removal of eclogitized oceanic plateau on the Farallon plate [e.g., Liu et al., 2008; Liu et al., 2010; Liu and Gurnis, 2010]. Given geodynamic modeling studies have demonstrated that slab rollback or steepening can cause surface deformation and uplift through both dynamic and isostatic processes [e.g., Gvirtzman and Nur, 1999; Buiter et al., 2002; Göğüş et al., 2011], a westward slab rollback beneath Wyoming during ~55–48 Ma may

have resulted in the uplift of the central Rockies [Fan and Carrapa, 2014]. These two groups of hypotheses predict different spatiotemporal patterns of surface deformation, and potentially lithosphere structure because thermal heating related to slab removal may weaken lithosphere [e.g., Djomani et al., 1999; Pérez–Gussinyé and Watts, 2005].

Herein we study the temporal and spatial evolution of Wyoming lithospheric stiffness and the rate of mountain load height gain during the Laramide deformation using a suite of 2D flexural subsidence models for the Laramide intermontane basins in the central Rockies (Figure 2-1). These models assume that the reverse–fault bounded Laramide ranges caused flexural subsidence of the elastic Wyoming lithosphere, and the spatial variations of basin–fill thickness reflect subsidence patterns that are determined by range size and lithospheric stiffness [e.g., Jordan, 1981; Angevine et al., 1990; Painter and Carrapa, 2013]. We explore the controlling factors on continental lithospheric stiffness in terms of the effective elastic thickness (T_e) or the flexural rigidity (D) in order to delineate and constrain the mechanisms that weakened the Wyoming lithosphere during the Laramide deformation.

2.2 Geologic setting

2.2.1 Regional tectonics

Our study area in the central Rockies is mostly located in the state of Wyoming (Figure 2-1). During the Cretaceous, the high–angle subduction of the

Farallon plate beneath the western portion of the North American plate caused the Sevier deformation by crustal shortening and thickening [e.g., DeCelles, 2004]. The Sevier fold–and–thrust belt system propagated eastward into western Wyoming and the rest of Wyoming was situated in the foreland of the fold–and–thrust belt that was covered by the Western Interior Seaway during the late Cretaceous [e.g., Weimer, 1960; Kauffman, 1977; DeCelles, 2004]. Beginning in the Maastrichtian, the high convergence rate between the North American plate and the Farallon plate [e.g., Hamilton, 1981; Jones et al., 2011], and/or the subduction of a buoyant oceanic plateau [e.g., Livaccari et al., 1981; Tarduno et al., 1985; Liu et al., 2008; Liu et al., 2010], resulted in a low-angle subduction of the Farallon plate and triggered the Laramide deformation [e.g., Snyder et al., 1976; Coney and Reynolds, 1977; Livaccari et al., 1981; Bird, 1988; Erslev, 1993; DeCelles, 2004; Humphreys, 2009]. The Laramide deformation partitioned the Sevier foreland into a system of basement–cored mountain ranges and intervening sedimentary basins during the latest Cretaceous–early Eocene [e.g., Dickinson and Snyder, 1978; Dickinson et al., 1988; DeCelles, 2004]. The vertical structural relief created by the high magnitude of uplift and exhumation of the Laramide ranges and concurrent subsidence of the intermontane basins exceeded 10 km [e.g., Dickinson et al., 1988; DeCelles et al., 1991; Hoy and Ridgway, 1997].

2.2.2 Basin stratigraphy and age constraints

Although the uplift of some of the Laramide ranges may have begun as early as the Campanian [Hamilton, 1981], it is generally agreed upon, that the main phase of the Laramide deformation occurred during the Maastrichtian–early Eocene because the Maastrichtian Fox Hill Formation is the last marine deposition in our study area [Dickinson et al., 1988]. We briefly summarize the depositional environments, basin–fill patterns, and age constraints of the Maastrichtian–lower Eocene strata in below.

The depositional environments of the Laramide intermontane basins changed from coastal marine environment during the Maastrichtian to fluvial and lacustrine environments during the Paleocene–early Eocene. The Maastrichtian Lance Formation is composed of interbedded fine– to coarse–grained, in part conglomeratic, sandstone, black shale, and coal, with the thickness generally ranging from 0.1 km to 1.0 km, but reaching up to ~1.5 km in some local depocenters [e.g., Keefer, 1965]. The Paleocene Fort Union Formation consists of interbedded conglomerate, sandstone, shale, and coal that were predominantly deposited in fluvial environments, and the thickness varies between 0.1 km and 2.0 km [e.g., Keefer, 1965; Courdin and Hubert, 1969; Curry, 1971]. Short–lived shallow fresh lakes deposited sand rich mudstone within the Fort Union Formation in the Powder River, Wind River, and Bighorn basins [Yuretich et al., 1984; Lillegraven and Ostresh, 1988]. The lower Eocene Wasatch Formation in

the Powder River and Green River basins and its equivalents, Willwood Formation in the Bighorn Basin, Indian Meadows and Wind River formations in the Wind River Basin, were deposited in fluvial environments, and are sequences of variegated conglomerate, sandstone, siltstone, and paleosol with the preserved thickness varying between ~0.1 km and 2.0 km [e.g., Whipkey et al., 1991; Roehler, 1992; 1993; Pietras and Carroll, 2006; Fan et al., 2011]. Major long–lived lakes only occurred during the early to middle Eocene in the Green River Basin, which deposited the Green River Formation as lenticular and tabular fine–grained sandstone and interbedded shale, lignite, and argillaceous or fossiliferous limestone [Johnson, 1985; Roehler, 1992; 1993]. The lower Eocene strata are the youngest and widely preserved strata in the intermontane basins due to the widespread post–Laramide erosion [Dickinson et al., 1988].

The Maastrichtian–lower Eocene strata in the studied basins were dated mainly based on land mammal fossil assemblages and pollen biostratigraphy in the Powder River, Wind River, Green River and Bighorn basins [e.g., Morris, 1954; Keefer, 1965; Obernyer, 1979; Roehler and Martin, 1987; Pocknall, 1987; Honey, 1988]. Pollen biozones and fossil stages were calibrated to the absolute geologic time scale based on paleomagnetostratigraphy and radiometric dating of ash beds only in certain portions of the studied period [e.g., Mauger, 1977; Clyde et al., 1997; Machlus et al., 2004; Woodburne, 2004; Smith et al., 2008; Peppe et al., 2011]. The ages of the stratigraphic units in this study were assigned based on

available biostratigraphy, paleomagnetostratigraphy, and radiometric geochronology studies in each basin, and lithostratigraphic correlations.

2.3 Methodology

We model the 2D flexural subsidence of intermontane basins in the central Rockies in order to document the evolution of lithospheric stiffness and mountain load height during the Laramide deformation. The load in our modeling consists of an exhuming mountain that deflects the elastic lithosphere to form a foreland basin, and the amount of flexural subsidence of a foreland basin diminishes away from the load [e.g., Beaumont, 1981; Jordan, 1981; DeCelles and Giles, 1996]. The wavelength and magnitude of the lithospheric deflection, which is represented by the width and depth of the foreland basin, are dependent on lithospheric stiffness and size (width and height) of the mountain load [Turcotte and Schubert, 1982; Watts, 2001]. Once the influence of sediment loading on basin subsidence is accounted for, the thickness and spatial variations of the preserved strata in the foreland basin can be used to model lithospheric stiffness and corresponding size of the mountain load [e.g., Jordan, 1981; Angevine et al., 1990; Painter and Carrapa, 2013].

The Paleocene–lower Eocene strata in the Powder River, Bighorn, Wind River, and Green River basins, and the upper Cretaceous strata in the Powder River, Bighorn, and Wind River basins, all thicken towards the basin–bounding Laramide ranges [Keefer, 1965; Curry, 1971; Johnson and Andersen, 2009; Finn

et al., 2010] (Figure 2-2). This is consistent with flexural subsidence caused by the tectonic loading of the Laramide ranges [e.g., Hagen et al., 1985; Fan and Carrapa, 2014]. We note that seismic reflection has shown the basement in the northwestern Green River Basin, near the front of the Wind River thrust, to be folded and possibly faulted as a result of uneven fault slippage [King and Brewer, 1983]. Although basin–fill in the area thickens significantly towards the Wind River Range [Curry, 1973], the pattern of basin subsidence cannot be purely explained by flexural subsidence and therefore we exclude this area from our models.

2.3.1 Decompaction

We divide the uppermost Cretaceous–lower Eocene strata in the studied basins into several stratigraphic units following the published isopach maps (Figure 2-2) [Keefer, 1965; Curry, 1971; Johnson and Andersen, 2009; Finn et al., 2010], and model the flexural subsidence of each stratigraphic unit in order to estimate the lithospheric stiffness and mountain load height during each period. The strata were decompacted based on empirically derived porosity–depth relationships for various lithologies [e.g., Bond et al., 1983]. Because there is only a minor amount of conglomerate compared to sandstone and shale, for simplicity we assume the studied strata include 40 % sandstone and 60 % shale, and we adopted the original porosity and lithology constants for sandstone and shale from Sclater and Christie [1980]. In order to conduct decompaction, the thickness and

lithology of post–Laramide strata must be known. However, the post–Laramide strata are not well preserved in these basins. Therefore, following the thickness reconstructions of the post–Laramide strata by McMillan et al. [2006] and the burial history of each basin based on hydrocarbon thermal maturation modeling [e.g., Pollastro and Barker, 1986; Anna et al., 2009; Finn et al., 2010], we estimate the post–Laramide strata thickness to be 2.4 km in the Bighorn basin, 1.9 km in the Powder River basin, 2.1 km in the Wind River basin, and 2.3 km in the Green River basin.

2.3.2 2D flexural subsidence modeling

We model the flexural subsidence of the Laramide intermontane basins assuming a 2D infinite elastic plate supported by inviscid mantle [Jordan, 1981; Turcotte and Schubert, 1982; Angevine et al., 1990; Watts, 1992]. In our study area the reverse faults are generally shallower than 40 km [Smithson et al., 1979], while the globally observed lithospheric thickness of old cratons are typically larger than 70–90 km [Bechtel et al., 1990; Burov and Diament, 1995]. Therefore an infinite elastic plate approximation is valid here because the reverse faults in our study area are not deep enough to penetrate the entire Wyoming lithosphere to cause the Wyoming craton behave as a broken beam. For load shape, although a mountain belt is often complex and variable both spatially and temporally [Flemings and Jordan, 1990; Sinclair et al., 1991; DeCelles and Mitra, 1995], it can be simplified and approximated by a rectangle shape with the height of the

rectangle representing the mean height of the load (Figure 2-3) [Jordan, 1981; Angevine et al., 1990; Allen et al., 2000; Currie, 2002]. In our modeling approach, we fix the width of each studied mountain to be the present–day width because the change of width of a mountain belt bounded by high–angle reverse fault is negligible during uplift. With these assumptions, we follow the standard procedure of 2D flexural subsidence modeling of foreland basins [e.g., Jordan, 1981; Turcotte and Schubert, 1982; Watts, 1992] and model the mountain load height and lithospheric stiffness by matching the modeled 2D subsidence profile with the observed 2D subsidence profile inferred from the isopach map. The relationship between D and T_e is expressed in equation (1), where E is Young's modulus and υ is Poisson's ratio (Table 2-1).

$$D = \frac{ET_e^3}{12[1-v^2]} \tag{1}$$

One should note that the division of the stratigraphic units in this study is based purely on available isopach maps, and therefore the ability of this work to define the temporal patterns of uplift and change of lithospheric stiffness is limited by the temporal precision of isopach maps.

To calculate the load–induced 2D deflection *w* of an infinite elastic plate over mantle in the absence of horizontal tension or compression, we use equation (2) based on Turcotte and Schubert [1982] following the method outlined in

Angevine et al. [1990]. The parameters and their assigned values are summarized in Table 2-1.

$$w(x) = \begin{cases} \frac{\rho_L h_L}{2(\rho_m - \rho_s)} \left[2 - cos\left(\frac{x+L}{\alpha}\right) e^{-\left(\frac{x+L}{\alpha}\right)} - cos\left(\frac{L-x}{\alpha}\right) e^{-\left(\frac{L-x}{\alpha}\right)} \right] & |x| \le L \\ \frac{\rho_L h_L}{2(\rho_m - \rho_s)} \left[cos\left(\frac{x-L}{\alpha}\right) e^{-\left(\frac{x-L}{\alpha}\right)} - cos\left(\frac{x+L}{\alpha}\right) e^{-\left(\frac{x+L}{\alpha}\right)} \right] & |x| > L \end{cases} \quad (2)$$

Here, the rectangular mountain load is defined by height h_L and width $2L$, x represents the distance away from the load center (Figure 2-3). In this formulation, the accommodation space is created by combined mountain and sediment infill loading. We use a mountain load density ρ_L of 2800 kg/m^3 [Daly et al., 1966; Smithson, 1971] because the Laramide basement–cored ranges are predominantly composed of Archean granite and gneiss. The sediment infill load density ρ_s is assumed to be the typical original density for sediment 1950 kg/m^3 [Athy, 1930], because we have decompacted each stratigraphic unit. The flexural parameter α is given by equation (3) and the remaining model parameters are defined in Table 2-1.

$$\alpha = \sqrt[4]{\frac{4D}{(\rho_m - \rho_s)g}} \quad (3)$$

A modeled 2D flexure profile that best fits the observed 2D basin–fill profile among 10,000 simulations is reached for each stratigraphic unit by using a Monte–Carlo optimization function in Matlab, which tests different combinations

of the values of load height and lithospheric stiffness drawn from two independent uniform distributions with a fixed load width (parameter space is summarized in Table 2-1). The “goodness of fit” value is calculated as one minus the normalized root–mean–square misfit, where the resulting value of 1.0 or 100% corresponds to a perfect fit. In Figure 2-4, we demonstrate the convergence of our method using the Wasatch Formation (57–50 Ma old) in the Powder River Basin as an example with a half width of the Bighorn Mountains fixed at 40 km. Here we fully explore the parameter space of possible mountain load height (cross–sectional area) and lithospheric stiffness and observe a clear convergence to the best–fit of mountain load height and T_e as indicated by the highest goodness of fit (Figure 2-4). Therefore, the method we use here has the ability to constrain the spatial and temporal variations of the mountain load height and lithospheric stiffness. Because the isopach maps used for this study have limited spatial extent, a range of combinations can create a basin that acceptably fits the observed 2D profile based on isopach maps. We arbitrarily define the model as having an acceptable fit when the goodness of fit is higher than 70%. Our best–fits are all better than 80%. The error bars of best–fits in Table 2-2 are derived as the standard deviation of acceptable fits.

We recognize that 2D flexural modeling with the assumption of sole mountain load is a simplification and that the subsidence of a basin may be also influenced by mountains bounding the basin to the other directions, or nearby segments of

the same mountains. However, the influence of distal loads should be much smaller than the subsidence caused by the load adjacent to a depocenter. We only need to consider the influence from nearby segments of a mountain when the depocenter–bounding fault is segmented and the depocenter migrated through time, which might be the case for the Wind River Basin because the mountains bounding the basin to the north and west contain several individual structures [Keefer, 1965]. These may, to a certain degree, lead to an overestimation of the load heights of the southern Bighorn and Owl Creek mountains.

2.4 Load heights and lithospheric stiffness

The best–fit load height (h_L) and lithospheric stiffness (T_e) corresponding to each stratigraphic unit in the studied basins are shown in Figure 2-5 and summarized in Table 2-2. The results show that the major Laramide mountain range loads gained accumulative heights of 3.3±0.1–8.9±0.7 km during the Laramide deformation and, with the exception of the central Bighorn Mountain, the load height gain accelerated during the early Eocene (Figure 2-6A). We note here that, the load height inferred from our modeling is the thickness of a rectangular load, which represents the vertical distance between the load top and preexisting surface (Figure 2-3). Therefore, the estimated load height is generally higher than the mean elevation, especially for a deep basin.

Localized T_e of Wyoming lithosphere varies between 6 and 46 km during the Laramide deformation (Table 2-2). Temporally, the lithospheric stiffness was

smaller during the Larmide deformation compared to the stiffness during the Sevier deformation and at present, both of which have flexural rigidities in the range of $10^{23.0}$–$10^{24.0}$ N m [Lowry and Smith, 1994; 1995; Painter and Carrapa, 2013], corresponding to a T_e range of 25–55 km. Spatially, the stiffness of the Wyoming lithosphere gradually decreases from northeast (T_e=32–46 km) to southwest (T_e=6–9 km), but remains nearly constant throughout the Laramide deformation in each basin (Table 2-2, Figure 2-6B, Figure 2-7).

2.5 Discussion

2.5.1 Southwestward weakening of Wyoming lithosphere

Our modeling results generally show lower stiffness of the Wyoming lithosphere during the Laramide deformation. Our modeled T_e values decreased to the southwest spatially, but remained stable throughout the ~30 Myrs of deformation. Here we discuss the factors that control the flexural rigidity of a continental lithosphere in an effort to explain the observed spatiotemporal pattern during the Laramide deformation.

For an oceanic lithosphere, T_e depends primarily on the thermal age of lithosphere, which equates to the crustal age at the time of loading, and is defined as the depth to a critical lithospheric isotherm that corresponds to elastic–plastic transition [e.g., Watts et al., 1980; Bodine et al., 1981]. However, this simple relationship becomes more complicated and uncertain when applied to a continental lithosphere, where T_e and thermal age are poorly correlated [e.g.,

Watts, 1992; Burov and Diament, 1995; Jackson, 2002; Afonso and Ranalli, 2004; Burov, 2011]. Factors that might influence the rigidity of a continental lithosphere during elastic deformation include composition, thermal age and structure, preexisting mechanical heterogeneity, strain rate during the deformation, end loads at the plate boundary, bending stresses caused by flexure, and the degree of crust–mantle decoupling [e.g., Watts et al., 1982; Kusznir and Karner, 1985; Pollack, 1986; Burov and Diament, 1995; Toussaint et al., 2004; Tesauro et al., 2012].

Lithosphere composition is an important factor that influences lithospheric stiffness, especially in continents [e.g., Burov and Diament, 1995; Toussaint et al., 2004; Tesauro et al., 2012]. Although the strength of mantle lithosphere may play an important role in determining the overall lithospheric stiffness [e.g., Burov, 2011], there is no documented evidence for any lateral variation of the composition of mantle lithosphere in Wyoming during the Laramide deformation. For crustal composition, the intermontane basins we studied were all developed in the Archean Wyoming craton, which is covered by 5–6 km of Phanerozoic sedimentary rocks containing both carbonates and siliciclastics [Love and Christiansen, 1985]. Although magmatism that occurred during the late Archean may have changed the composition of the Wyoming crust on a regional scale, such changes are not widespread and do not display any spatial pattern [Chamberlain et al., 2003]. As lithosphere cools with age it strengthens [e.g.

Karner and Watts, 1983; Mouthereau et al., 2013]. The Wyoming craton was stable and experienced minimal deformation during the Paleozoic and Mesozoic. Although the late Archean magmatism and tectonism, and Proterozoic extension may have partially modified the Wyoming province [Chamberlain et al., 2003], these changes should not have caused a significant variation in the thermal age of the Wyoming lithosphere during the Laramide deformation because continental lithosphere takes 400 Ma or at most up to 750–1000 Ma to completely cool [Burov and Diament, 1995]. Therefore, it is reasonable to exclude compositional difference and thermal age and structure from being major factors that caused the spatial variation of Wyoming lithospheric stiffness during the Laramide deformation.

It is nonetheless entirely plausible that preexisting faults formed by Archean and Proterozoic tectonics may have introduced mechanical heterogeneity and weakened the lithosphere locally. However, such preexisting heterogeneity should also control the variation of the present–day lithospheric flexural rigidity in our study area, but gravity studies, aside from some slight variability, do not exhibit an up to three orders of magnitude difference or a gradual–decrease of flexural rigidity from northeastern Wyoming to southwestern Wyoming [Lowry and Smith, 1994; 1995]. Moreover, there is no recognized spatial variation in the density of faults formed during the Laramide deformation in our study area, suggesting that the rigidity of the brittle upper crust of the Wyoming lithosphere

is nearly homogenous. The derived rate of height gain of the Laramide ranges in this study also do not show a pattern of gradual–increase from northeastern Wyoming to southwestern Wyoming, suggesting that the strain rate during the Laramide deformation was not a controlling factor in changing the lithospheric stiffness. Indeed, previous studies have suggested that upper lithospheric brittle failure and variation of strain rate can only result in very small variation of lithospheric strength [e.g., Kusznir and Karner, 1985; Hopper and Buck, 1993; Burov and Diament, 1995].

Bending stresses, which develop in the lithosphere beneath large topographic loads due to flexure, reduce lithospheric stiffness [Burov and Diament, 1995; Hyndman et al., 2009]. If bending stresses, together with any existing compressional or extensional stresses, reach a local yield limit of the lithosphere, zones of inelastic (brittle or ductile) behavior will appear [Burov and Diament, 1995]. Western Wyoming was in front of the Sevier highland during the studied period, thus it is possible that the bending stresses caused by the topographic loading of the Sevier highland together with the overall compressional stress in the broad Cordillera orogen have weakened the lithosphere in southwestern Wyoming, and possibly induced lower crustal flow. Bending stresses could reduce local lithospheric stiffness and lead to a 30–80 % decrease of T_e beneath a major mountain belt, and smaller decrease in the adjacent regions [Burov and Diament, 1995]. For example, in the northern Andes, T_e decreases from ~70 km

to ~25 km across a distance of ~500 km from the margin of the foreland basin to the mountain front [Stewart and Watts, 1997], which corresponds to a ~1.3 orders magnitude decrease in D. Therefore, bending stresses caused by the Sevier fold–and–thrust belt may partially contribute to the southwestward three orders of magnitude decrease of lithospheric stiffness in Wyoming.

Crust–mantle decoupling has been suggested by many previous studies to be an important factor of causing extraordinarily low elastic thickness in some places with old lithosphere and adjacent to thickened crust, for examples, T_e is 5–30 km in the Carpathian foredeep, and as low as 5 km in the retroarc foreland basins of the central Andes along the Altiplano and Puna plateaus [e.g., McNutt et al., 1988; Burov and Diament, 1995; Stewart and Watts, 1997; Pérez–Gussinyé et al., 2008, 2009; Tesauro et al., 2012]. Middle or lower crust of most continental plates has a low–temperature activation rheology (such as quartz) [Burov and Diament, 1995], and laboratory studies of the strength of such mid– or lower crustal materials indicate that they will flow at a faster rate than mantle dunite or peridotite when subjected to flexural stresses [Carter and Tsenn, 1987; Ord and Hobbs, 1989]. Although it is very likely that crust–mantle decoupling occurred in western Wyoming because of the bending stress induced by topographic loading, mid–crustal flow from overthickened crust in the Cordilleran hinterland [McQuarrie and Chase, 2000] can equally cause a difference in lithospheric stiffness. It has also been suggested that the present crustal thickness of 45–50

kilometers in Wyoming was established during the early Cenozoic because the region was not significantly affected by Cenozoic extension [e.g., Karlstrom et al., 2002]. Such a thick crust may be caused by the eastward mid–crustal flow from the overthickened crust in the Cordilleran hinterland during the Laramide deformation [McQuarrie and Chase, 2000]. Therefore, our observed variation of lithospheric stiffness may partially reflect that the degree of crust–mantle decoupling became smaller northeastward.

End loads placed onto the North American lithosphere by the subducting Farallon oceanic plate may also contribute to the variation of lithospheric stiffness in Wyoming. Subducting oceanic plate places end loads to continental lithosphere at plate boundary, and the loads include end force and bending moment [Burov and Diament, 1995]. An end force of a typical effective weight anomaly represented by a subducting slab could lead to 20–30% T_e reduction in area 100-200 km from the margin of the continental plate; and a plate boundary bending moment has a similar effect [Burov and Diament, 1995]. Although the influence of end loads caused by subduction at plate boundary reduces significantly as it reaches Wyoming, low–angle subduction may have caused additional end force in continental interior by enhancing the mechanical coupling between the subducting slab and the overriding thick Wyoming lithosphere at the west edge of the Wyoming craton [Livaccari and Perry, 1993].

In summary, after considering possible factors that influence the stiffness of a continental lithosphere, we suggest that the southwestward decrease of T_e in Wyoming lithosphere during the Laramide deformation was caused by the combination of bending stress induced by the large topographic loading of the Sevier fold–and–thrust belt, crust–mantle decoupling that possibly initiated under the overthickened Sevier hinterland, and end loads due to the low angle subduction at the western edge of the thick Wyoming craton.

2.5.2 Implications for the geodynamics of Laramide deformation

Our results show that the rates of load height gain of four out of the five studied Laramide ranges accelerated during the early Eocene (Figure 2-6A). We note here again, that load height is not indicative of the absolute elevation of a mountain range (Figure 2-3). However, load height gain is associated with exhumation and surface uplift. The accelerated height gain during the early Eocene compared to the Maastrichtian–Paleocene documented in this study is generally consistent with pervious observations of accelerated basin subsidence, surface uplift and exhumation during the late Paleocene–early Eocene compared to the Maastrichtian–early Paleocene [Fan and Carrapa, 2014]. The difference of absolute cutoff of the age could be easily explained by errors in the ages used in each study. In particular, most of the isopach maps used in this study were divided into Paleocene and Eocene. The high load height of the southern Bighorn and Owl Creek mountains by the end of the Laramide deformation seems in contrast with

today's relatively low elevation of the two mountains. Because our load height is not elevation (Figure 2-3), we cannot estimate the relationship between the two. It is possible that we overestimate the load heights of the two mountains by attributing deep accommodation space in the depocenter of the Wind River Basin solely to one load even though the area is bounded by several structures [Keefer, 1965]. If load height is linearly related to elevation, differential erosion of mountain ranges [Foster et al., 2010] after the Laramide deformation may explain the difference between today's low topography and modeled high load height.

Based on accelerated exhumation and elevation gain of the Laramide ranges, Fan and Carrapa [2014] proposed a two–stage history of the Laramide deformation and suggested that the deformation during the Maastrichtian–early Paleocene may be attributed to the low angle subduction of Farallon plate and the accelerated deformation during the late Paleocene–early Eocene may be due to slab removal through rollback [e.g., Coney and Reynolds, 1977; Constenius, 1996], or removal of ecologitized oceanic plateau or aseismic ridges [e.g., Liu et al., 2008; Liu et al., 2010; Liu and Gurnis, 2010]. Our flexural modeling results agree with this two–stage history of Laramide deformation by showing accelerated load height gain of the Laramide ranges during the early Eocene. We note here that Gries [1983] and Chapin and Cather [1983] also suggested a two–stage Laramide deformation model by examining the structure and sedimentation in the Colorado Plateau–Rocky Mountains area and suggested that the ranges

striking N–S were uplifted earlier than the ranges striking W–E. Moreover, they suggested that the two–stage deformation was in response to a change in the subduction direction of the Farallon plate from eastward to northward.

Our results help elucidate the geodynamic processes that influenced the stiffness of the Wyoming lithosphere and thereby controlled the surface deformation patterns in the two–stage Laramide deformation model. In the Late Cretaceous, our study area was located in the foreland of the thin–skinned Sevier fold–and–thrust belt [e.g., Livaccari, 1991; DeCelles, 2004] (Figure 2-8A). The subducted Farallon oceanic plate dipped steeply during most of the Sevier deformation, but became gently inclined during the very late stage (ca. 81 Ma) [Liu et al., 2010; Jones et al., 2011; Painter and Carrapa, 2013]. The bending stresses induced by the topographic load of the Sevier fold–and–thrust belt combined with crust–mantle decoupling initiated by the overthickened Sevier hinterland and the end loads due to the low angle subduction at the western edge of the thick Wyoming craton, caused the southwestward decrease of lithospheric stiffness in Wyoming at the beginning of Laramide deformation. The uplift of the Laramide mountain ranges during the latest Cretaceous–Paleocene may be a simple response to the intra–plate compressional strain during the low angle subduction (Figure 2-8B). The acceleration of uplift during the early Eocene was likely a dynamic and isostatic response to the rollback or removal of the flat slab, probably associated with the ecologitization of an oceanic plateau on the slab, at

~55 Ma [e.g., Liu et al., 2008; Liu et al., 2010; Liu and Gurnis, 2010] (Figure 2-8C). Although it is generally perceived that dynamic effect causes long–wavelength uplift, it is not the case in the central Rockies may because that strain release preferentially occurred along preexisting faults. The slab rollback model has been suggested by many previous studies based on several lines of evidence, including the trenchward migration of igneous activity between ~55 Ma and ~47 Ma [Constenius, 1996]; the uplift and exhumation of the Laramide ranges became younger southwestward during the late Paleocene–early Eocene [Fan and Carrapa, 2014]; and the westward hydrologic ponding and unconformity development in the Greater Green River Basin during the early Eocene [Smith et al., 2014].

If our interpretation that the rollback and removal of the flat slab caused accelerated uplift is correct, the process did not cause a change of lithospheric stiffness during the Laramide deformation based on our modeling results. Numerical models of low-angle subduction suggest that the overriding lithosphere is cooled when low–angle subduction replaces hot asthenospheric wedge [Currie and Beaumont, 2011]. During the low-angle subduction of the Farallon plate, this cooling effect would have reduced the geothermal gradients during the Laramide deformation in the western Cordillera [Dumitru et al., 1991]. Subsequent mantle upwelling associated with the removal of the flat slab during the Laramide deformation should have lowered the stiffness of the Wyoming lithosphere. Instead, we found that the lithospheric stiffness remained nearly constant

throughout the removal of flat slab, which may imply that tectonically induced bending stress, end loads, and associated crust–mantle decoupling played a bigger role in determining lithospheric stiffness than mantle heating in this region.

2.6 Conclusions

Latest Cretaceous–early Eocene basin–fill in major Wyoming Laramide intermontane basins thickens towards the basin–bounding Laramide ranges, suggesting that the basins were formed due to flexural deflection of the Wyoming lithosphere. We conducted 2D flexural subsidence modeling of these basins in order to infer the spatial and temporal variations of the Wyoming lithospheric stiffness and mountain height gain during the Laramide deformation. Our modeling results show that, starting from the beginning of the Laramide deformation, the stiffness of Wyoming lithosphere exhibited a southwestward decreasing pattern (from T_e=32–46 km in northeastern Wyoming to T_e=6–9 km in southwestern Wyoming), and such pattern lasted throughout the ~30 Myr Laramide deformation. We attribute this southwestward decrease of lithospheric stiffness to the combination of bending stress induced by the large topographic loading of the Sevier fold–and–thrust belt, crust–mantle decoupling that possibly initiated under the overthickened Sevier hinterland, and end loads resulting from the low angle subduction at the western edge of the thick Wyoming craton. Our results also indicate that the height gain of the major Laramide ranges accelerated during the early Eocene. This accelerated height gain, which reflects accelerated

uplift and deformation, is consistent with the two–stage model of Laramide deformation proposed by Fan and Carrapa [2014].

Acknowledgements

This research was funded by PRF–54673–DNI8 and a GSA student research grant to Min Gao. All the data supporting the conclusions can be found in the paper and the cited references. We thank Associate Editor Giampiero Iaffaldano and three anonymous reviewers for their valuable comments that helped us to improve the manuscript.

References

Afonso, J.C. and G. Ranalli (2004), Crustal and mantle strengths in continental lithosphere: is the jelly sandwich model obsolete? Tectonophysics, 394, 221–232.

Allen, P.A., J.E. Verlander, P.M. Burgess and D.M. Audet (2000), Jurassic giant erg deposits, flexure of the United States continental interior, and timing of the onset of Cordilleran shortening, Geology, 28(2), 159-162.

Angevine, C. L., P. L. Heller, and C. Paola (1990), Quantitative Sedimentary Basin Modeling, Continuing Education Course Note Series, vol. 32, 256 pp., American Association of Petroleum Geologists, Tulsa, Okla.

Anna, L.O., T.R. Klett and P.A. Le (2009), Total petroleum systems and geologic assessment of oil and gas resources in the Powder River Basin Province, Wyoming and Montana: U.S. Geological Survey Digital Data Series DDS–69–U, 3 chaps., 1 CD-ROM. (Revised April 2010)

Athy, L.F. (1930), Density, porosity, and compaction of sedimentary rocks, AAPG Bull., 14(1), 1-24.

Beaumont, C. (1981), Foreland basins, Geophysical Journal International, 65(2), 291-329.

Bechtel, T.D., D.W. Forsyth, V.L. Sharpton and R.A. Grieve (1990), Variations in effective elastic thickness of the North American lithosphere, Nature, 343, 636-638.

Bird, P. (1988), Formation of the rocky mountains, Western United States: a continuum computer model, Science, 239(4847), 1501-1507, doi: 239/4847/1501 [pii].

Bodine, J., M. Steckler and A. Watts (1981), Observations of flexure and the rheology of the oceanic lithosphere, J.geophys.Res., 86(B5), 3695-3707.

Bond, G.C., M.A. Kominz and W.J. Devlin (1983), Thermal subsidence and eustasy in the Lower Palaeozoic miogeocline of western North America, Nature, 306, 775-779.

Buiter, S.J., R. Govers and M. Wortel (2002), Two-dimensional simulations of surface deformation caused by slab detachment, Tectonophysics, 354(3), 195-210.

Burov, E.B. (2011), Rheology and strength of the lithosphere, Marine and Petroleum Geology, 28, 1402–1443.

Burov, E.B., and M. Diament (1995), The effective elastic thickness (T_e) of continental lithosphere: What does it really mean?, Journal of Geophysical Research: Solid Earth (1978–2012), 100(B3), 3905-3927.

Carter, N.L., and M.C. Tsenn (1987), Flow properties of continental lithosphere, Tectonophysics, 136(1), 27-63.

Chamberlain, K.R., C.D. Frost and B.R. Frost (2003), Early Archean to Mesoproterozoic evolution of the Wyoming Province: Archean origins to modern lithospheric architecture, Canadian Journal of Earth Sciences, 40(10), 1357-1374.

Chapin, C.E., and S.M. Cather (1983), Eocene tectonics and sedimentation in the Colorado Plateau-Rocky Mountain area, in Lowell, J. D., ed., Rocky Mountain foreland basins and uplifts, Denver, Colorado, Rocky Mountain Association of Geologists, pp. 33–56.

Clyde, W.C., J. Zonneveld, J. Stamatakos, G.F. Gunnell and W.S. Bartels (1997), Magnetostratigraphy across the Wasatchian/Bridgerian NALMA boundary (early to middle Eocene) in the western Green River basin, Wyoming, J.Geol., 105(6), 657-670.

Coney, P.J., and S.J. Reynolds (1977), Cordilleran benioff zones, Nature, 270, 403-406.

Constenius, K.N. (1996), Late Paleogene extensional collapse of the Cordilleran foreland fold and thrust belt, Geological Society of America Bulletin, 108(1), 20-39.

Courdin, J.L., and J.F. Hubert (1969), Sedimentology and mineralogical differentiation of sandstones in the Fort Union Formation (Paleocene), Wind River Basin, Wyoming, 21st Annual Field Conference, Wyoming Geological Association Guidebook, pp. 29–37, Casper, Wyoming.

Currie, B.S. (2002), Structural Configuration of the Early Cretaceous Cordilleran Foreland–Basin System and Sevier Thrust Belt, Utah and Colorado, J.Geol., 110(6), 697-718.

Currie, C. A. and C. Beaumont (2011), Are diamond-bearing Cretaceous kimberlites related to low-angle subduction beneath western North America?, Earth and Planetary Science Letters, 303(1), 59–70.

Curry III, W.H. (1973), Late Cretaceous and early Tertiary rocks, southwestern Wyoming, Wyoming Geological Association 25th Annual Field Conference Guidebook, pp. 79-86.

Curry III, W.H. (1971), Laramide structural history of the Powder River basin, Wyoming, in Symposium on Wyoming Tectonics and Their Economic Significance, Wyoming Geological Association, 23d Annual Field Conference Guidebook, pp. 49–60.

Daly, R., G.E. Manger and S.P. Clark (1966), Section 4: Density of rocks, Geological Society of America Memoirs, 97, 19-26.

DeCelles, P.G. (2004), Late Jurassic to Eocene evolution of the Cordilleran thrust belt and foreland basin system, western USA, Am.J.Sci., 304(2), 105-168.

DeCelles, P.G., and K.A. Giles (1996), Foreland basin systems, Basin research, 8(2), 105-123.

DeCelles, P.G., and G. Mitra (1995), History of the Sevier orogenic wedge in terms of critical taper models, northeast Utah and southwest Wyoming, Geological Society of America Bulletin, 107(4), 454-462.

DeCelles, P., M. Gray, K. Ridgway, R. Cole, D. Pivnik, N. Pequera and P. Srivastava (1991), Controls on synorogenic alluvial-fan architecture, Beartooth Conglomerate (Palaeocene), Wyoming and Montana, Sedimentology, 38(4), 567-590.

Dickinson, W.R., M.A. Klute, M.J. Hayes, S.U. Janecke, E.R. Lundin, M.A. McKITTRICK and M.D. Olivares (1988), Paleogeographic and paleotectonic setting of Laramide sedimentary basins in the central Rocky Mountain region, Geological Society of America Bulletin, 100(7), 1023-1039.

Dickinson, W.R., and W.S. Snyder (1978), Plate tectonics of the Laramide orogeny, Geological Society of America Memoirs, 151, 355-366.

Djomani, Y.H.P., J.D. Fairhead and W.L. Griffin (1999), The flexural rigidity of Fennoscandia: reflection of the tectonothermal age of the lithospheric mantle, Earth Planet.Sci.Lett., 174(1), 139-154.

Dumitru, T. A., P. B. Gans, D. A. Foster, and E. L. Miller (1991), Refrigeration of the western Cordilleran lithosphere during Laramide shallow-angle subduction, Geology, 19(11), 1145-1148.

Erslev, E.A. (1993), Thrusts, back-thrusts, and detachment of Rocky Mountain foreland arches, in Laramide Basement Deformation in the Rocky Mountain Foreland of the Western United States, Geological Society of America Special Paper 280, edited by C. J. Schmidt, 339-358.

Fan, M., and B. Carrapa (2014), Late Cretaceous–early Eocene Laramide uplift, exhumation, and basin subsidence in Wyoming: Crustal responses to flat slab subduction, Tectonics, 33(4), 509-529.

Fan, M., P.G. DeCelles, G.E. Gehrels, D.L. Dettman, J. Quade and S.L. Peyton (2011), Sedimentology, detrital zircon geochronology, and stable isotope geochemistry of the lower Eocene strata in the Wind River Basin, central Wyoming, Geological Society of America Bulletin, 123(5-6), 979-996.

Finn, T., M. Kirschbaum, S. Roberts, S. Condon, L. Roberts and R. Johnson (2010), Cretaceous–Tertiary Composite Total Petroleum System (503402), Bighorn Basin, Wyoming and Montana, US Geol.Surv., Digital Data Ser. DDS-69-V, pp. 157.

Flemings, P.B., and T.E. Jordan (1990), Stratigraphic modeling of foreland basins: Interpreting thrust deformation and lithosphere rheology, Geology, 18(5), 430-434.

Foster, D., S. H. Brocklehurst and R. L. Gawthorpe (2010), Glacial–topographic interactions in the Teton Range, Wyoming, Journal of Geophysical Research: Earth Surface, 115(F1).

Göğüş, O.H., R.N. Pysklywec, F. Corbi and C. Faccenna (2011), The surface tectonics of mantle lithosphere delamination following ocean lithosphere subduction: Insights from physical–scaled analogue experiments, Geochem. Geophys. Geosyst., 12(5), Q05004, doi:10.1029/2010GC003430.

Gries, R. (1983), North-south compression of Rocky Mountain foreland structures, In: Lowell, D., ed., Rocky Mountain Foreland Basins and Uplifts. Rocky Mountain Association of Geologists Guidebook, Denver, Colorado, pp. 9–32.

Gvirtzman, Z., and A. Nur (1999), Plate detachment, asthenosphere upwelling, and topography across subduction zones, Geology, 27(6), 563-566.

Hagen, E.S., M.W. Shuster and K.P. Furlong (1985), Tectonic loading and subsidence of intermontane basins: Wyoming foreland province, Geology, 13(8), 585-588.

Hamilton, W. (1981), Plate-tectonic mechanism of Laramide deformation, Contributions to Geology-University of Wyoming, Laramie, 19(2), 87-92.

Honey, J. (1988), A mammalian fauna from the base of the Eocene Cathedral Bluffs Tongue of the Wasatch Formation, Cottonwood Creek area, southeast Wasatch Basin, Wyoming: US Geological Survey Bulletin C., 1669, 1-13.

Hopper, J.R., and W.R. Buck (1993), The initiation of rifting at constant tectonic force: role of diffusion creep, Journal of Geophysical Research: Solid Earth (1978–2012), 98(B9), 16213-16221.

Hoy, R.G., and K.D. Ridgway (1997), Structural and sedimentological development of footwall growth synclines along an intraforeland uplift, east-central Bighorn Mountains, Wyoming, Geological Society of America Bulletin, 109(8), 915-935.

Humphreys, E. (2009), Relation of flat subduction to magmatism and deformation in the western United States, Geological Society of America Memoirs, 204, 85-98.

Hyndman, R., C. Currie, S. Mazzotti and A. Frederiksen (2009), Temperature control of continental lithosphere elastic thickness, T_e vs V_s, Earth Planet.Sci.Lett., 277(3), 539-548.

Jackson, J. (2002), Strength of the continental lithosphere: time to abandon the jelly sandwich? GSA Today, 12 (9), 4–10, doi:10.1130/1052-5173.

Johnson, P.L., and D.W. Andersen (2009), Concurrent growth of uplifts with dissimilar orientations in the southern Green River Basin, Wyoming Implications for Paleocene–Eocene patterns of foreland shortening, Rocky Mountain Geology, 44(1), 1-16.

Johnson, R.C. (1985), Early Cenozoic history of the Uinta and Piceance Creek basins, Utah and Colorado, with special reference to the development of Eocene Lake Uinta, in Flores, R.M., and Kaplan, S.S., eds., Cenozoic paleogeography of the west central United States: Rocky Mountain Section, Society of Economic Paleontologists and Mineralogists, Rocky Mountain Paleogeography Symposium 3, pp. 247–276.

Jones, C.H., G.L. Farmer, B. Sageman and S. Zhong (2011), Hydrodynamic mechanism for the Laramide orogeny, Geosphere, 7(1), 183-201.

Jones, C.H., L.J. Sonder and J.R. Unruh (1998), Lithospheric gravitational potential energy and past orogenesis: Implications for conditions of initial Basin and Range and Laramide deformation, Geology, 26(7), 639–642.

Jordan, T.E. (1981), Thrust loads and foreland basin evolution, Cretaceous, western United States, AAPG Bull., 65(12), 2506-2520.

Karlstrom, K., Bowring, S. A., Chamberlain, K. R., Dueker, K. G., Eshete, T., Erslev, E. A., Farmer, G. L., Hiezler, M., Humphreys, E. D., Johnson, R. A., Keller, G. R., Kelley, S. A., Levander, A., Magnani, M. B., Matzel, J. P., McCoy, A. M., Miller, K. C., Morozova, E. A., Pazzaglia, F. J., Prodehl, C., Rumpel, H. M., Shaw, C. A., Sheehan, A. F., Shoshitaishvili, E., Smithson, S. B., Snelson, C. M., Stevens, L. M., Tyson, A. R., and Williams, M. L. (2002), Structure and evolution of the lithosphere beneath the Rocky Mountains: Initial results from the CD-ROM experiment, GSA Today, 12, 4–9.

Karner, G., and A. Watts (1983), Gravity anomalies and flexure of the lithosphere at mountain ranges, Journal of Geophysical Research: Solid Earth (1978–2012), 88(B12), 10449-10477.

Kauffman, E.G. (1977), Geological and biological overview: Western Interior Cretaceous basin, The Mountain Geologist, 14, 75–99.

Keefer, W.R. (1965), Stratigraphy and geologic history of the uppermost Cretaceous, Paleocene, and lower Eocene rocks in the Wind River Basin, Wyoming, U.S. Geological Survey Professional Paper, 495-A, pp. 77.

Keefer, W.R., T.M. Finn, R.C. Johnson and C.W. Keighin (1998), Regional stratigraphy and correlation of Cretaceous and Paleocene rocks, Bighorn Basin, Wyoming and Montana, Wyoming Geological Association 49th Annual Field Conference Guidebook, 1–30.

King, G., and J. Brewer (1983), Fault related folding near the Wind River thrust, Wyoming, USA, Nature, 306(5939), 147–150.

Kusznir, N., and G. Karner (1985), Dependence of the flexural rigidity of the continental lithosphere on rheology and temperature, Nature, 316, 138–142.

Lillegraven, J., and L. Ostresh (1988), Evolution of Wyoming Early Cenozoic topography and drainage patterns, National Geographic Research, 4(3), 303-327.

Liu, L., and M. Gurnis (2010), Dynamic subsidence and uplift of the Colorado Plateau, Geology, 38(7), 663-666.

Liu, L., M. Gurnis, M. Seton, J. Saleeby, R.D. Müller and J.M. Jackson (2010), The role of oceanic plateau subduction in the Laramide orogeny, Nature Geoscience, 3(5), 353-357.

Liu, L., S. Spasojevic and M. Gurnis (2008), Reconstructing Farallon plate subduction beneath North America back to the Late Cretaceous, Science, 322(5903), 934-938, doi: 10.1126/science.1162921 [doi].

Livaccari, R.F. (1991), Role of crustal thickening and extensional collapse in the tectonic evolution of the Sevier-Laramide orogeny, western United States, Geology, 19(11), 1104-1107.

Livaccari, R.F., K. Burke and A. Şengör (1981), Was the Laramide orogeny related to subduction of an oceanic plateau?, Nature, 289, 276–278.

Livaccari, R. F. and F. V. Perry (1993), Isotopic evidence for preservation of Cordilleran lithospheric mantle during the Sevier–Laramide orogeny, western United States. Geology, 21(8), 719–722.

Love, J.D., and A.C. Christianson (1985), Geologic map of Wyoming, U.S. Geological Survey, scale 1:500 000.

Lowry, A.R., and R.B. Smith (1995), Strength and rheology of the western US Cordillera, JOURNAL OF GEOPHYSICAL RESEARCH-ALL SERIES-, 100, 17,947-17,947.

Lowry, A.R., and R.B. Smith (1994), Flexural rigidity of the Basin and Range-Colorado Plateau-Rocky Mountain transition from coherence analysis of

gravity and topography, JOURNAL OF GEOPHYSICAL RESEARCH-ALL SERIES-, 99, 20,123-20,123.
Machlus, M., S.R. Hemming, P.E. Olsen and N. Christie-Blick (2004), Eocene calibration of geomagnetic polarity time scale reevaluated: Evidence from the Green River Formation of Wyoming, Geology, 32(2), 137-140.
Mauger, R.L. (1977), K-Ar ages of biotites from tuffs in Eocene rocks of the Green River, Washakie, and Uinta basins, Utah, Wyoming, and Colorado, Rocky Mountain Geology, 15(1), 17-41.
McMillan, M.E., P.L. Heller and S.L. Wing (2006), History and causes of post-Laramide relief in the Rocky Mountain orogenic plateau, Geological Society of America Bulletin, 118(3-4), 393-405.
McNutt, M., M. Diament and M. Kogan (1988), Variations of elastic plate thickness at continental thrust belts, Journal of Geophysical Research: Solid Earth (1978–2012), 93(B8), 8825-8838.
McQuarrie, N., and C.G. Chase (2000), Raising the Colorado plateau, Geology, 28(1), 91-94.
Morris, W.J. (1954), An Eocene fauna from the Cathedral Bluffs Tongue of the Washakie Basin, Wyoming, J. Paleontol., 28, 195-203.
Mouthereau, F., A.B. Watts and E. Burov (2013), Structure of orogenic belts controlled by lithosphere age, Nature geoscience, 6(9), 785-789.
Obernyer, S.L. (1979), Basin-margin depositional environments of the Fort Union and Wasatch Formations (Tertiary) in the Buffalo-Lake De Smet area, Johnson County, Wyoming, U.S. Geological Survey Open-File Report 79-712, pp. 116.
Ord, A., and B. Hobbs (1989), The strength of the continental crust, detachment zones and the development of plastic instabilities, Tectonophysics, 158(1), 269-289.
Painter, C.S., and B. Carrapa (2013), Flexural versus dynamic processes of subsidence in the North American Cordillera foreland basin, Geophys.Res.Lett., 40(16), 4249-4253.
Peppe, D.J., D.L. Royer, B. Cariglino, S.Y. Oliver, S. Newman, E. Leight, G. Enikolopov, M. Fernandez–Burgos, F. Herrera and J.M. Adams (2011), Sensitivity of leaf size and shape to climate: global patterns and paleoclimatic applications, New Phytol., 190(3), 724-739.
Pérez–Gussinyé, M., and A.B. Watts (2005), The long-term strength of Europe and its implications for plate-forming processes, Nature, 436(7049), 381-384.
Pérez–Gussinyé, M., A. Lowry, J. Phipps Morgan and A. Tassara (2008), Effective elastic thickness variations along the Andean margin and their relationship to subduction geometry, Geochem. Geophys. Geosyst., 9(2), doi:10.1029/2007GC001786.

Pérez–Gussinyé, M., C. Swain, J. Kirby and A. Lowry (2009), Spatial variations of the effective elastic thickness, T_e, using multitaper spectral estimation and wavelet methods: examples from synthetic data and application to South America, Geochem. Geophys. Geosyst., 10(4), Q04005. http://dx.doi.org/10.1029/2008GC002229.

Pietras, J.T., and A.R. Carroll (2006), High-resolution stratigraphy of an underfilled lake basin: Wilkins Peak member, Eocene Green River Formation, Wyoming, USA, Journal of Sedimentary Research, 76(11), 1197-1214.

Pocknall, D.T. (1987), Palynomorph biozones for the Fort Union and Wasatch Formations (upper Paleocene–lower Eocene), powder river basin, Wyoming and Montana, USA, Palynology, 11(1), 23-35.

Pollack, H.N. (1986), Cratonization and thermal evolution of the mantle, Earth Planet.Sci.Lett., 80(1), 175-182.

Pollastro, R.M., and C.E. Barker (1986), Application of clay-mineral, vitrinite reflectance, and fluid inclusion studies to the thermal and burial history of the Pinedale anticline, Green River basin, Wyoming, In: Gautier, D.L. ed., Roles of Organic Matter in Sediment Diagenesis, SEPM, pp. 73-83, Special Publication, 32.

Roehler, H.W. (1993), Eocene climates, depositional environments, and geography, greater Green River Basin, Wyoming, Utah, and Colorado, U. S. Geological Survey Professional Paper, 1506-F, pp. 74.

Roehler, H.W. (1992), Correlation, composition, areal distribution, and thickness of Eocene stratigraphic units, Greater Green River Basin, Wyoming, Utah, and Colorado, U. S. Geological Survey Professional Paper, 1506-E, pp. 49.

Roehler, H.W., and P. Martin (1987), Geological investigations of the Vermillion creek coal bed in the Eocene Niland tongue of the wasatch formation, Sweetwater County, Wyoming, U. S. Geological Survey Professional Paper, 1314 A-L, pp. 1–202.

Sclater, J.G., and P. Christie (1980), Continental stretching: An explanation of the post-mid-Cretaceous subsidence of the central North Sea basin, Journal of Geophysical Research: Solid Earth (1978–2012), 85(B7), 3711-3739.

Sinclair, H., B. Coakley, P. Allen and A. Watts (1991), Simulation of foreland basin stratigraphy using a diffusion model of mountain belt uplift and erosion: an example from the central Alps, Switzerland, Tectonics, 10(3), 599-620.

Smith, J.J., S.T. Hasiotis, M.J. Kraus and D.T. Woody (2008), Naktodemasis bowni: new ichnogenus and ichnospecies for adhesive meniscate burrows (AMB), and paleoenvironmental implications, Paleogene Willwood

Formation, Bighorn Basin, Wyoming, Journal of Paleontology 82(2), 267–278.
Smith, M. E., A. R. Carroll, B. R. Jicha, E. J. Cassel and J. J. Scott (2014), Paleogeographic record of Eocene Farallon slab rollback beneath western North America, Geology, 42(12), 1039–1042.
Smithson, S.B. (1971), Densities of metamorphic rocks, Geophysics, 36(4), 690-694.
Smithson, S.B., J. Brewer, S. Kaufman, J. Oliver and C.A. Hurich (1979), Structure of the Laramide Wind River uplift, Wyoming, from COCORP deep reflection data and from gravity data, Journal of Geophysical Research: Solid Earth (1978–2012), 84(B11), 5955-5972.
Snyder, W., W. Dickinson and M. Silberman (1976), Tectonic implications of space-time patterns of Cenozoic magmatism in the western United States, Earth Planet.Sci.Lett., 32(1), 91-106.
Stewart, J., and A. Watts (1997), Gravity anomalies and spatial variations of flexural rigidity at mountain ranges, JOURNAL OF GEOPHYSICAL RESEARCH-ALL SERIES-, 102, 5327-5352.
Tarduno, J.A., M. McWilliams, M.G. Debiche, W.V. Sliter and M. Blake (1985), Franciscan Complex Calera limestones: Accreted remnants of Farallon plate oceanic plateaus, Nature, 317, pp. 345–347, doi:10.1038/317345a0.
Tesauro, M., P. Audet, M.K. Kaban, R. Bürgmann and S. Cloetingh (2012), The effective elastic thickness of the continental lithosphere: Comparison between rheological and inverse approaches, Geochem. Geophys. Geosyst., 13 (9), Q09001, http://dx.doi.org/10.1029/2012GC004162.
Toussaint, G., E. Burov, and L. Jolivet (2004), Continental plate collision: Unstable vs. stable slab dynamics, Geology, 32, 33–36, doi: 10.1130/G19883.1.
Turcotte, D., and G. Schubert (1982), Geodynamics: Applications of continuum physics to geological problems, 450 pp., John Wiley, New York.
Watts, A. (1992), The effective elastic thickness of the lithosphere and the evolution of foreland basins, Basin Research, 4(3-4), 169-178.
Watts, A., J. Bodine and M. Steckler (1980), Observations of flexure and the state of stress in the oceanic lithosphere, Journal of Geophysical Research: Solid Earth (1978–2012), 85(B11), 6369-6376.
Watts, A., G. Karner and M. Steckler (1982), Lithospheric flexure and the evolution of sedimentary basins, Philosophical Transactions of the Royal Society of London A: Mathematical, Physical and Engineering Sciences, 305(1489), 249-281.
Watts, A.B. (2001), Isostasy and Flexure of the Lithosphere, Cambridge University Press, Cambridge.

Weimer, R.J. (1960), Upper cretaceous stratigraphy, rocky Mountain area, AAPG Bull., 44(1), 1-20.
Whipkey, C., V.V. Cavaroc and R.M. Flores (1991), Uplift of the Bighorn Mountains, Wyoming and Montana–a sandstone provenance study, U. S. Geol. Surv. Bull., 19, 17-D.
Woodburne, M.O. (2004), Late Cretaceous and Cenozoic mammals of North America: biostratigraphy and geochronology, Columbia University Press, New York.
Yuretich, R.F., L.J. Hickey, B.P. Gregson and Y. Hsia (1984), Lacustrine deposits in the Paleocene Fort Union Formation, northern Bighorn Basin, Montana, Journal of Sedimentary Research., 54(3), 836–852.

Figures and tables

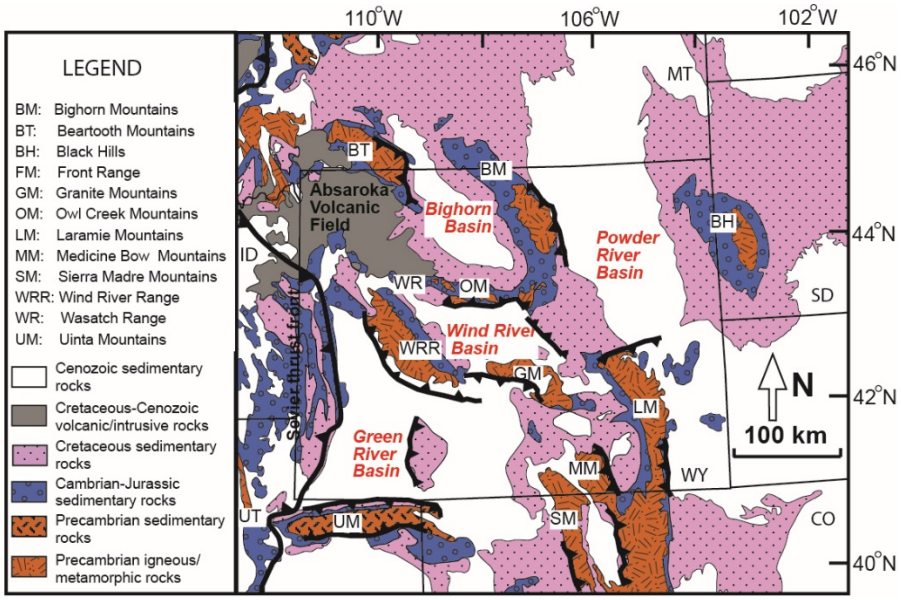

Figure 2-1 Structural units of the study area in the central Rockies and location of the studied intermontane basins, modified after Fan and Carrapa [2014].

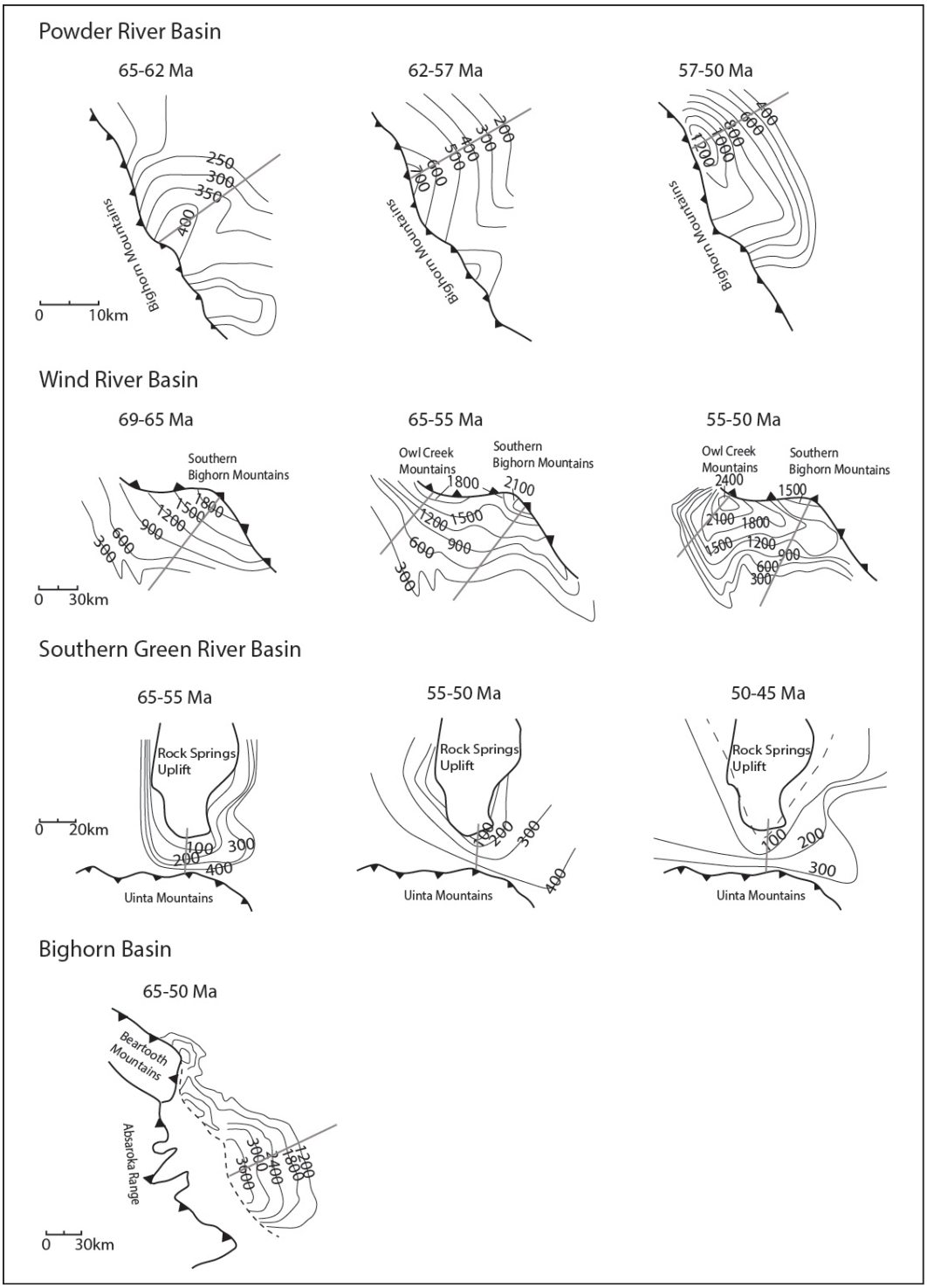
Powder River Basin
65-62 Ma
62-57 Ma
57-50 Ma
Bighorn Mountains
0 10km
Wind River Basin
69-65 Ma
65-55 Ma
55-50 Ma
Southern Bighorn Mountains
Owl Creek Mountains
0 30km
Southern Green River Basin
65-55 Ma
55-50 Ma
50-45 Ma
Rock Springs Uplift
Uinta Mountains
0 20km
Bighorn Basin
65-50 Ma
Beartooth Mountains
Absaroka Range
0 30km

Figure 2-2 Isopach maps used in 2D flexural subsidence modeling, modified from Keefer [1965], Curry [1971], Johnson and Andersen [2009], and Finn et al. [2010]. Unit of contour intervals is meter. The strata in the Bighorn Basin are further divided into three stratigraphic units for modeling based on local thickness data in Keefer et al. [1998]. Straight grey lines represent the 2D transects used for modeling in Figure 2-5.

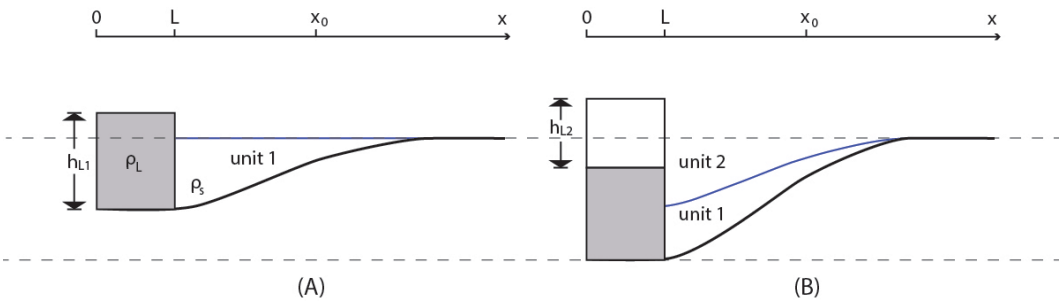

Figure 2-3 Conceptual models showing two stages of flexural subsidence of a basin. During the first stage (A), a mountain load with height of h_{L1} caused flexural subsidence of an elastic plate, and stratigraphic unit 1 filled the resultant flexure. During the second stage (B), the load gained a height of h_{L2} and caused additional flexural subsidence to accommodate stratigraphic unit 2. Note that unit 1 was compacted by unit 2, and load height is different from elevation.

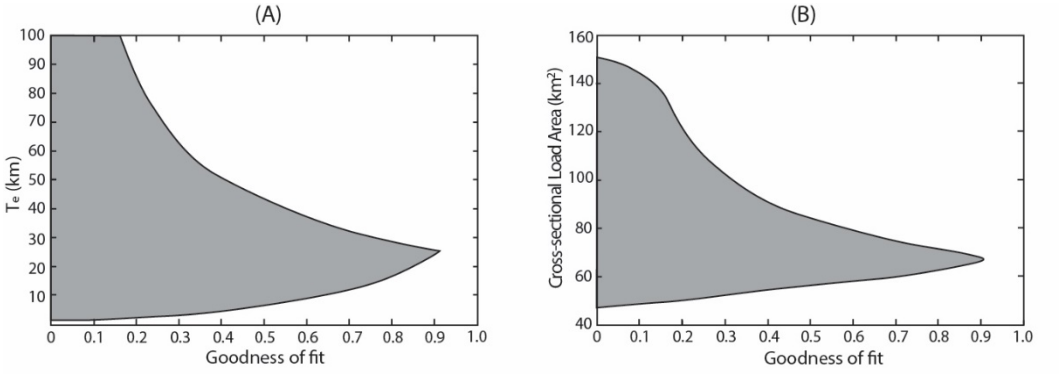

Figure 2-4 Convergence of (A) effective elastic thickness and (B) cross–sectional load area corresponding to high goodness of fit (see text) for the Wasatch Formation in Powder River Basin for a fixed 40 km half–width load. Shaded area represents the results of 10,000 models of flexural subsidence compared to the observed profile. The cross–sectional load area is product of load height and width. Because we use a fixed mountain width (present–day width) in the model, (B) also depicts the convergence of mountain load height to high goodness of fit.

(A) Powder River Basin -- Central Bighorn Mountains

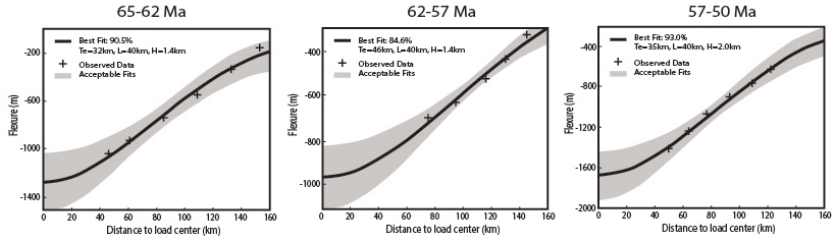

(B) Bighorn Basin -- Washakie Range

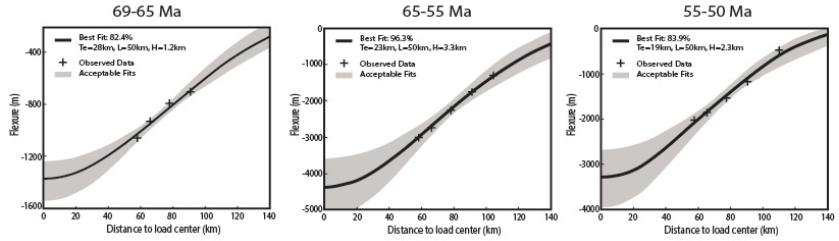

(C) NE Wind River Basin -- Southern Bighorn Mountains

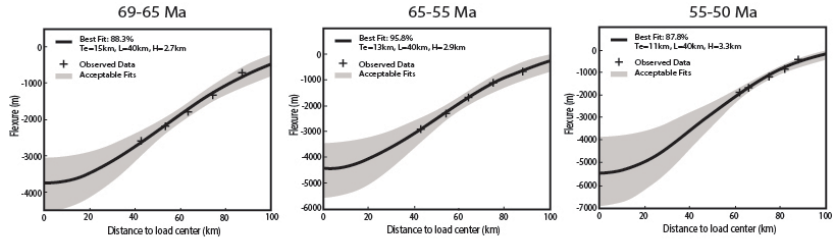

(D) N Wind River Basin -- Owl Creek Mountains

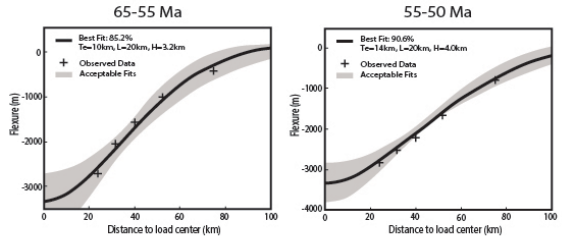

(E) S Green River Basin -- Uinta Mountains

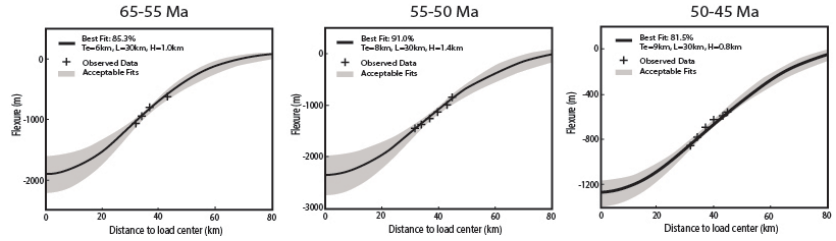

Figure 2-5 Acceptable fits and best–fits (as defined in text) of modeled 2D subsidence profile compared with subsidence profile derived from isopach patterns (represented by black crosses). The percentage number is the goodness of fit. Profile locations are shown in Figure 2-2.

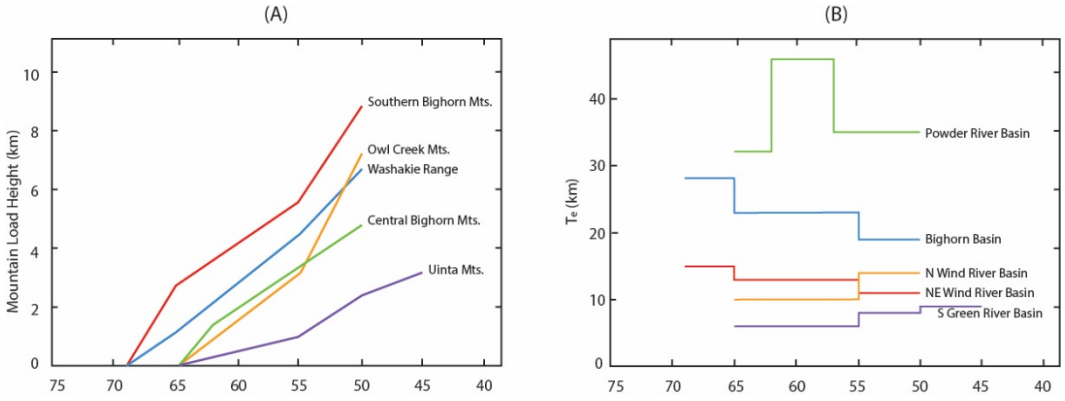

Figure 2-6 (A) Histories of load height gain of the studied mountain ranges; (B) Temporal variations of Te in the studied basins. Plotted based on Table 2-2.

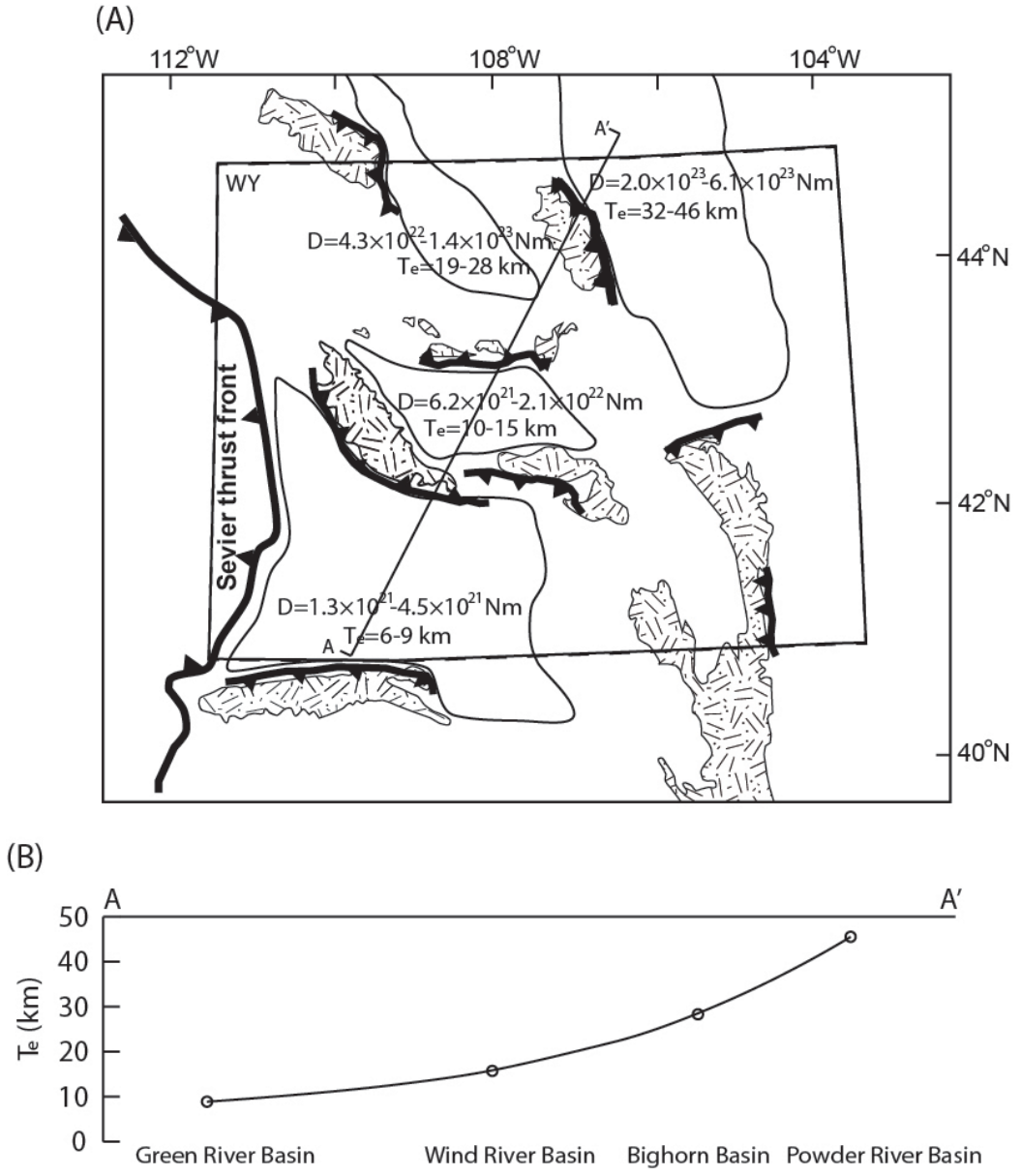

Figure 2-7 (A) Inferred spatial variations of lithospheric stiffness in Wyoming during the Laramide deformation; (B) Change in T_e from southwest Wyoming to northeast Wyoming (circles indicating T_e values derived from this modeling study).

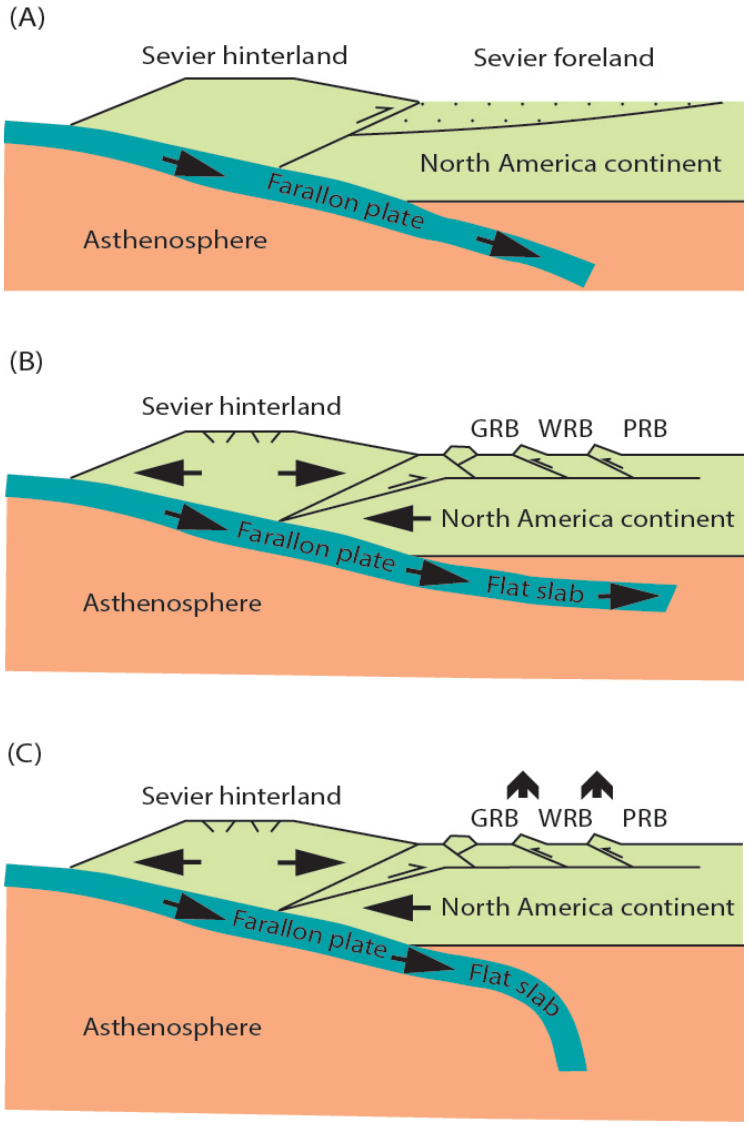

Figure 2-8 Schematic cross–sections illustrating the principal mechanisms of the two–stage Laramide deformation model discussed in text. (A) Pre–Laramide deformation during the Late Cretaceous, the study area was located in the foreland of the Sevier fold–and–thrust belt, and the subducting oceanic plate gradually changed from high angle to low angle; (B) Laramide deformation during the latest Cretaceous–Paleocene, horizontal compressional stresses caused intra–plate crustal deformation; (C) Laramide deformation during the early Eocene, rollback of the flat slab caused accelerated surface uplift by dynamic and isostatic processes. GRB: Green River Basin; WRB: Wind River Basin; PRB: Powder River Basin. Figures are modified after Fan and Carrapa [2014].

Table 2-1 Parameters and their assigned values in the 2D flexural subsidence model

Symbol	Symbol interpretation	Value used in the model
x	distance from the mountain center	
w(x)	deflection of the lithosphere	
h_L	height of the mountain load	200m – 4000m
L	half width of the mountain load	
T_e	Effective elastic thickness	1 km – 100 km
α	flexural parameter, has a relationship with flexural rigidity D	
ρ_L	density of mountain load	2800kg/m^3
ρ_m	density of mantle	3300kg/m^3
ρ_s	density of basin fill	1950kg/m^3
E	Young's modulus	70GPa
v	Poisson's ratio	0.25

Table 2-2 Load heights and lithospheric stiffness derived from the model

Basin–Mountain Pair	Duration (Ma)	D (N m)	T_e (km)	Load Height (m)	Accumulative Load Height (m)	Rate of Height Gain (mm/yr)
Powder River Basin	65–62	$2.0\times10^{23}\pm5.0\times10^{20}$	32±4	1421±96	1421±96	0.47
(Central Bighorn Mts.)	62–57	$6.1\times10^{23}\pm7.5\times10^{20}$	46±5	1371±44	2792±140	0.27
	57–50	$2.7\times10^{23}\pm5.6\times10^{20}$	35±4	1995±87	4787±227	0.29
Bighorn Basin	69–65	$1.4\times10^{23}\pm1.5\times10^{20}$	28±3	1185±27	1185±27	0.30
(Washakie Range)	65–55	$7.6\times10^{22}\pm1.9\times10^{20}$	23±3	3290±135	4475±162	0.33
	55–50	$4.3\times10^{22}\pm9.3\times10^{19}$	19±2	2263±110	6738±272	0.45
NE Wind River Basin	69–65	$2.1\times10^{22}\pm5.3\times10^{19}$	15±2	2665±133	2665±133	0.67
(Southern Bighorn Mts.)	65–55	$1.4\times10^{22}\pm4.9\times10^{19}$	13±2	2902±195	5567±328	0.29
	55–50	$8.3\times10^{21}\pm7.9\times10^{18}$	11±1	3318±358	8885±686	0.66
N Wind River Basin	65–55	$6.2\times10^{21}\pm5.1\times10^{18}$	10±1	3190±191	3190±191	0.32
(Owl Creek Mts.)	55–50	$1.7\times10^{22}\pm2.2\times10^{19}$	14±2	3996±84	7186±275	0.80
S Green River Basin	65–55	$1.3\times10^{21}\pm3.3\times10^{18}$	6±1	1032±43	1032±43	0.10
(Uinta Mts.)	55–50	$3.2\times10^{21}\pm7.0\times10^{18}$	8±1	1421±45	2453±88	0.28
	50–45	$4.5\times10^{21}\pm2.8\times10^{18}$	9±1	826±17	3279±105	0.17

Chapter 3 Depositional environment, sediment provenance and oxygen isotope paleoaltimetry of the early Paleogene Greater Green River Basin, southwestern Wyoming, U.S.A.

Abstract

Depositional process, sediment provenance, and paleotopography are critical to paleogeographic reconstruction during the coeval Laramide and Sevier deformations in the Cordillera orogenic system. Here we conduct lithofacies analysis, sediment provenance and paleoelevation studies to the fluvial lower Paleogene Fort Union and the main body of the Wasatch formations in the center of the Greater Green River Basin in order to reconstruct paleogeography. We document that the depositional environment changed from low-energy distal floodplain of a meandering river during the Paleocene to high-energy, braided rivers during the earliest Eocene. The lowermost Eocene strata have more Precambrian basement-derived feldspar grains compared to the Paleocene strata. This change in sediment provenance was associated with the dominant northward paleoflow direction, suggesting major uplift of the Laramide Uinta Mountains during the earliest Eocene. The $\delta^{18}O$ values of authigenic carbonates were stable during the early Paleocene, but decreased gradually from -10 ‰ during the late Paleocene to -18 ‰ during the earliest Eocene, suggesting the lack of highland precipitation in the basin catchment during the early Paleocene, and significant surface uplift and arrival of highland precipitation from the Uinta Mountains

during the earliest Eocene. The reconstructed paleoelevation of the Uinta Mountains was at least 3.5 km, possibly 3.5-4.5 km, and the paleorelief between the Greater Green River Basin and Uinta Mountains was ~4 km during the earliest Eocene. Our record of the earliest Eocene establishment of high topography of the Uinta Mountains is 4-6 Myr older than previously thought. Our record also adds to the growing body of evidence that suggests the Sevier hinterland had rugged topography during the early Paleogene.

Keywords: paleogeography, lithofacies, provenance, paleoaltimetry, oxygen isotopes, precipitation, early Paleogene, Greater Green River Basin

3.1 Introduction

The Rocky Mountain orogenic plateau in Wyoming and nearby area is an extensive region of high relief bounding the east side of the North American Cordillera (Figure 3-1A). The region sat in the foreland of the thin-skinned Sevier fold-and-thrust belt during the Late Jurassic-Cretaceous (DeCelles, 2004), and was partitioned by the thick-skinned Laramide deformation into a sequence of Precambrian basement-cored mountain ranges and intermontane basins during the latest Cretaceous-early Eocene (e.g., Dickinson and Snyder, 1978; Dickinson et al., 1988; DeCelles, 2004). The Sevier orogeny continued to the early Paleogene (e.g., DeCelles, 2004), and overlapped with the Laramide orogeny during the latest Cretaceous-earliest Eocene. The coeval Sevier and Laramide deformations may have both influenced drainage patterns and depositional environment in

western Wyoming. Although it is generally agreed that eastward-flowing rivers from the Sevier hinterland was interrupted by the Laramide orogeny during the Late Campanian and Maastrichtian (e.g., Lawton, 1986; Dickinson et al., 1988; DeCelles, 1994; Goldstrand, 1994; Janecke et al., 2000; DeCelles, 2004; Gierlowski-Kordesch et al., 2008), when and how did the Laramide orogeny establish new drainage patterns and depositional environment during the coeval Sevier-Laramide orogenies are still poorly understood.

The Greater Green River Basin in southwestern Wyoming, bounded by the Sevier fold-and-thrust belt to the west and several Laramide ranges to the other sides, is an ideal place to understand the influence of the two orogenies on paleogeography. Previous studies suggested that the rapid surface uplift of the basin-bounding Laramide ranges and rapid subsidence of the Greater Green River Basin did not start until the early middle Eocene, based on basin subsidence reconstruction, and sedimentology and stable isotope studies only to the lower and lower middle Eocene strata (e.g., Kauffman, 1977; Crews and Ethridge, 1993; Norris et al., 1996; Fan and Carrapa, 2014). Recent high-resolution geochemical studies, focused on the early and early middle Eocene Greater Green River Basin, Uinta Basin and Piceance Creek Basin, brought detailed understanding to the sedimentary and hydrologic evolutions of the Green River lake system (e.g., Carroll et al., 2008; Davis et al., 2008, 2009a and 2009b). None of the studies had

examined the depositional environment and paleoelevation of the basin-bounding mountain ranges during the entire early Paleogene.

In this work, we study the depositional environments, sediment provenance, and stable isotope signatures of the ~1400 m thick Paleocene and lowermost Eocene strata in the center of the Greater Green River Basin in order to reconstruct paleogeography and uplift history of the local mountain ranges. The results of this study are discussed with previously published results in a larger geological context to help understand the large-scale reorganization of drainage patterns during the Sevier-Laramide transition in the central North American Cordillera.

3.2 Regional geology

The Greater Green River Basin in southwestern Wyoming is bounded by the Sevier fold-and-thrust belt to the west, the Wind River Range and Granite Mountains to the north, the Rawlins uplift and Sierra Madre Mountains to the east, and the Uinta Mountains to the south (Figure 3-1B). The basin is divided into the Green River, Great Divide, Washakie, and Sand Wash subbasins by several intrabasinal anticlines, including the Rock Springs uplift, the Wamsutter arch, and the Cherokee Ridge (Fidlar, 1950). The field work location of this study is to the southeast of the Rock Springs Uplift (Figure 3-1B and C).

The Greater Green River Basin was located in the western part of the Western Interior Seaway during the Cretaceous, and the Seaway was formed under the

combined effect of flexural subsidence caused by the Sevier orogenic belt and dynamic subsidence caused by the subduction of an oceanic plateau on the Farallon oceanic plate (e.g., Kauffman, 1977; Levey, 1985; Gurnis, 1992; DeCelles, 2004; Liu and Nummedal, 2004; Liu et al., 2011). The basin became an isolated intermontane basin when the Laramide orogeny disrupted the Sevier orogeny during the latest Cretaceous-early Eocene (Dickinson et al., 1988; DeCelles, 2004; Gao et al., 2016). It is generally agreed that the change from the Sevier orogeny to the Laramide orogeny was associated with the change from high-angle, normal subduction to low-angle subduction of the Farallon oceanic plate beneath the western U.S.A. (e.g., Livaccari et al., 1981; Liu et al., 2008 and 2010; Jones et al., 2011).

The Cretaceous sedimentary rocks in the Greater Green River Basin include several regressive-transgressive sequences deposited during the interactions between tectonic movements of the Sevier fold-and-thrust belt and sea level fluctuations of the Western Interior Seaway (Jordan, 1981). The periodic uplifts of the Sevier fold-and-thrust belt produced pulses of massive eastward incursions of terrigenous clastics into the western part of the Western Interior Basin (e.g., Weimer, 1960; McGookey et al., 1972; Kauffman, 1977; Levey, 1985). The final withdrawal of the Western Interior Seaway occurred during the latest Cretaceous, and the Maastrichtian Fox Hill Formation formed in a shoreface environment recorded the last marine deposition in the study area (Dickinson et al., 1988).

The Paleogene strata in the Greater Green River Basin include the Paleocene Fort Union Formation and the lower Eocene Wasatch and Green River formations deposited in alluvial, fluvial, and lacustrine depositional environments (e.g., Love 1970; Hansen 1986; Dickinson et al., 1988; Shuster and Steidtmann, 1988; Roehler 1992; Pietras et al., 2003). The Fort Union and Wasatch formations consist of mainly interbedded sandstone, siltstone, mudstone, carbonaceous shale, and coal (Roehler, 1992) (Figure 3-2). Started from the Tipton Shale Member of the Green River Formation deposited during the early middle Eocene, the Lake Gosiute deposited a sequence of oil shale and interbedded sandstone, siltstone, dolomite, limestone, and tuff beds (Shuster and Steidtmann, 1988; Roehler, 1992). This lacustrine environment lasted until the deposition of the middle Eocene Bridger Formation, when fluvial environment dominated the area again (Roehler, 1992). Interbedded sandstone and conglomerate in coarsening- and fining-upward megasequences were mainly developed near the northern flank of the Uinta Mountains during the early Eocene, and were interpreted to be deposited in alluvial environments prior to the development of the Lake Gosiute (Crews and Ethridge, 1993).

The lower Paleogene strata in the Greater Green River Basin are dated mainly based on land mammal fossil assemblages, which were calibrated to the absolute geologic time scale based on paleomagnetostratigraphy and radiometric dating of ash beds in other basins (e.g., Clyde, 1997). Mammal fossils of *Diacodon*,

Gelastops, Mixodectes, *Paleotomus, Promioclaenus*, etc., typical to the early Torrejonian land mammal stage (To_2, ~61.3-62.3 Ma), were found in the Fort Union Formation ~8 km south of our studied locality (Rigby et al., 1980). Age-diagnostic fossils were previously documented at several stratigraphic levels in other measured sections of the Wasatch Formation near our studied section (Roehler, 1992). These stratigraphic levels can be correlated to our section based on their levels in the Paleocene and lowermost Eocene sequences and lithostratigraphic correlations. The presence of *Hyracotherium, Hyopsodus, Haplomylus, Diacodexis,* etc. in the main body of the Wasatch Formation in several localities places the deposition during the early and middle Wasatchian stage (Wa_0-Wa_5, ~55.0-53.4 Ma), and the presence of *Heptodon, Lambdotherium, Meniscotherium,* etc. in the Niland Tongue of the Wasatch Formation, stratigraphically above our studied section, places the upper limit of the top of the main body of the Wasatch Formation to the late Wasatchian stage (Wa_6-Wa_7, ~52.9-52.6 Ma) (e.g., Roehler, 1992; Tauxe et al., 1994).

3.3 Lithofacies and depositional environments

Lithofacies and depositional environments of the Paleocene and lowermost Eocene strata in the Greater Green River Basin have not been described in detail in previous studies. This paper presents interpretation of depositional environments based on lithofacies associations in a ~1400 m thick outcrop section of the Paleocene Fort Union Formation and lower Eocene Wasatch Formation to

the southeast of the Rock Springs Uplift (figs. 1 and 2). Lithofacies are divided based on lithology, sedimentary structures, and stacking patterns of the strata. The lithofacies in the studied lower Paleogene strata are typical of fluvial deposits and are well understood in terms of depositional processes (summaries in Miall, 1978 and 1996). Here we briefly summarize the common depositional processes and focus on interpreting depositional environment.

3.3.1 Fort Union Formation: Sandy Meandering River Association

Description

The Paleocene Fort Union Formation consists of multiple fining-upward sequences of fine- to medium-grained sandstone, mudstone, carbonaceous shale, and coal, totaling ~780 m in thickness at the studied site (Figure 3-2). The contact relationship between the Fort Union Formation and the underlying upper Cretaceous Lance Formation is a slight angular unconformity. The Fort Union Formation gently dips to southeast with a dip angle of ~11˚, while the underlying Lance Formation has a higher dip angle of ~14˚. It has been suggested that the Rock Springs Uplift experienced uplift and folding during the latest Cretaceous, which caused this angular unconformity and southerly truncation of the Lance Formation by the overlying Fort Union Formation (Breithaupt, 1982). In the area where the Fort Union Formation exposes, small hills capped by well-cemented sandstones and valleys containing mudstone, siltstone and coals with reliefs of 10-30 m characterize the landscape (Figure 3-3).

The measured section of the Fort Union Formation is characterized by an overbank lithofacies assemblage, shown as lithofacies changing from very fine- to medium-grained sandstone (S_h, S_l, S_m) to interlayered mudstone and siltstone (F_m), shale (F_l), paleosol (F_p) and coal (C) in each fining-upward sequence (Figure 3-2, Table 3-1). The sandstone units that start each fining-upward sequence are usually in grey to tan color, and 1-5 m thick. The sedimentary structures in the sandstone beds mainly include horizontal beddings, ripple and planar laminations (Figure 3-3). The sandstone beds have different cementing degree, and well-cemented light brown sandstone beds typically cap small hills. Interlayered tan, green, purple mudstone, shale and paleosol, and dark-grey carbonaceous shale and coal beds are deposited above the sandstone beds. The paleosols are identified mainly based on the mottled color, presence of life traces, and platy, blocky and peds soil structures (Retallack, 1997). The mottled color displays mainly as irregular patches of yellow or brown in a matrix of gray or green. Thin sheet-like very fine- to fine-grained sandstone (S_r, S_l, S_m) up to 0.3 m thick and limestone (L) beds of ~0.5 m thick are occasionally present in the fine-grained deposits. The limestone beds do not contain shell fragments. Coal beds are common, with thickness varying between 0.2 m and 4 m.

Interpretation

The fining-upward sequences in the Fort Union Formation are typical of floodplain deposition of a sandy meandering river system (Miall, 1985; Wright

and Marriott, 1993). Depositional processes on floodplains typically reflect the interaction of vertical and lateral accretions (e.g., Nanson, 1986; Rice, 1988). Lateral accretion is dominated by point bar migration, which typically deposits thick, stacked, cross-bedded sandstone with large accretionary sets (Nanson and Croke, 1992). Vertical accretion occurs during floods on overbank and typically presents as fine-grained sediments that are influenced by pedogenesis (Nanson and Croke, 1992; Moddy et al., 1999). The Fort Union Formation at the study site is dominated by vertical accretion during rising and waning flood stages, which is commonly documented as fining-upward sequences (Bridge, 1984). The sandstone beds at the base of each sequence are interpreted as crevasse splays rather than point bars because of the lack of lateral accretionary sets and cross stratifications. The sparse limestone lenses and abundant coal beds are formed in swamp environment, which is commonly developed on floodplains or in abandoned channels (Wright and Marriott, 1993). There are mainly two types of paleosol in this formation based on prominent pedogenic features. All the coal beds are of histosol because each coal originates as a waterlogged surface horizon containing a high concentration of plant debris, which meets the description of histic epipedon (Soil Survey Staff, 1975; Buol et al., 1980; Mack et al., 1993). The paleosols showing color mottling are gleysol, which commonly forms under alternating oxidation and reduction environments in regions of markedly

fluctuating water table (Mack et al., 1993). Both of these two types of paleosol indicate periodically flushed environments that were common on floodplains.

3.3.2 Wasatch Formation: Sandy Braided River Association

Description

The measured lowermost Eocene Wasatch Formation consists of variegated sandstone, siltstone, mudstone, shale, and paleosols, totaling ~650 m in thickness. The formation overlies the Fort Union Formation conformably. The formation is better exposed in outcrop than the Fort Union Formation because of the high abundance of sandstone units. In the study area, the Wasatch Formation was subdivided into the main body, the Niland Tongue, and the Cathedral Bluffs Tongue by Roehler (1987), and only the main body part is examined here.

The main body part of the Wasatch Formation consists of interlayered lenticular tan and yellow fine- to coarse-grained sandstone (S_t, S_h, S_r, S_l, S_m), grey, tan, and brown siltstone and mudstone (F_m), shale (F_l), and paleosol (F_p) (Figure 3-2, Table 3-1). The sandstone units are generally tens of centimeters to up to 15 m thick, showing no obvious grading. A ~0.5 m thick very coarse-grained sandstone bed containing mudclasts, chert granules and pebbles, and wood debris is present at the bottom of the formation. Thin lenticular sandstone beds less than 2 m thick are of lithofacies S_l, S_r, and S_m, and are encased in intervals of lithofacies F_m, F_l, and F_p. Sandstone units of 2-15 m thick present as stacked individual sandstone beds of lithofacies S_m, S_t, and S_r, and these units

sometimes change to lithofacies S_l upward. The sandstone units are usually not well cemented at the bottom, but become carbonate-cemented ledge formers at the top. The siltstone, mudstone, shale, and paleosols are all sandy. The paleosols are mottled, containing peds structures, root traces. Scattered carbonate nodules present in some of the paleosols. In the fine-grained deposits in the upper part of the section, large gypsum crystals and thin limestone lenses less than 0.5 m thick with abundant snail fossils occasionally present (Figure 3-3). Paleocurrent directions were estimated by measuring the orientations of limbs of trough cross-stratifications at seven stratigraphic levels in the formation. When possible, 10 measurements were made from each limb.

Interpretation

We interpret this portion of the Wasatch Formation to be deposited in sandy braided rivers. The stacked, thick lenticular sandstone units nested in fine-grained lithofacies are interpreted to be frequently migrating bars, which are typical of channel deposits in braided river systems (Miall, 1977). The thin sandstone layers are most likely of crevasse splay deposits. The sandstone units with lithofacies S_t, S_h changing to S_r and S_l upward were deposited on the tops or flanks of bars during waning flow or in abandoned channels (e.g., Rust, 1972; Miall, 1978). The occurrence of floating mudclasts, chert pebbles and wood debris in some sandstone beds indicates cutbank erosion caused by the spill out of sandy mudflows from channels onto the preexisting channel levees or floodplain

deposits (e.g., Pierson, 1981; DeCelles et al., 1991). The presence of carbonate nodules suggests development of calcisols (Mack et al., 1993), which is typical of floodplain deposition under relatively low sedimentation rates (Kraus, 1999). The paleoflow directions in this formation are generally northwestward to northward (Figure 3-2).

Overall, the depositional environment in the studied lower Paleogene stratigraphic section evolved from distal floodplain of a meandering river to braided rivers. The change of depositional environment is associated with the dominant northward paleoflow direction in the Wasatch Formation, suggesting adjustment of regional drainage system. We infer that the early Eocene uplift of the Uinta Mountains resulted in the birth of the braided rivers draining northward and established the new drainage pattern and depositional environment.

3.4 Sandstone petrography

3.4.1 Methods and Description

Standard petrographic thin sections were made from 23 sandstone samples. The thin sections were stained for K-feldspar and plagioclase, and were point-counted (400 counts per slide) using a modified Gazzi-Dickinson method, in which crystals larger than silt size within lithic fragments are counted as monocrystalline grains (Ingersoll et al., 1984). The modal composition data are then plotted on ternary plots to infer sediment provenance. Potential source terranes are inferred by comparing the sandstone modal compositions with

compositions of potential source rocks in the study area and at different geologic settings (Dickinson and Suczek, 1979).

Monocrystalline quartz is the most dominant composition of all the sandstone samples (Figure 3-4, Table 3-2 and Table 3-3). Feldspar mainly consists of potassium feldspar and plagioclase, with a K/P ratio varying between 1 and 3. Lithic grains contain predominantly chert, sandstone and siltstone fragments, and a small amount of limestone and volcanic grains. Biotite and muscovite are the most common accessory minerals, constituting less than 5% of the total grains. The sandstones in the Fort Union and Wasatch formations have average modal compositions of Q_m:F:L_t=48:22:30, Q_tFL=47:21:32; and Q_m:F:L_t=45:35:20, Q_t:F:L=48:34:18, respectively (Figure 3-5, Table 3-2 and Table 3-3). The sandstones in the Wasatch Formation have higher amount of feldspar grains (up to 20% higher), particularly plagioclase, than the ones in the Fort Union Formation. The monocrystalline quartz grains in the Fort Union Formation are moderately-well rounded, very fine- to fine-grained; while the ones in the Wasatch Formation are angular to subangular, and medium- to coarse-grained (Figure 3-4). The sandstones are usually cemented by carbonate and hematite, and contain variable amount of matrix. Samples from the Fort Union Formation contain more hematite cement compared to the ones from the Wasatch Formation.

3.4.2 Interpretation

The sandstone modal compositions show that the sandstones in the Paleocene Fort Union Formation were derived from a recycled orogenic provenance, and the sandstones in the lower Eocene Wasatch Formation have contributions from both recycled orogen and continental block (Figure 3-5). Sediment sources in a recycled orogen provenance could be deformed and uplifted strata in subduction zones, along collision orogens or within fold-and-thrust belts; and sediment sources in a continental block provenance could be shields, platforms, or faulted basement blocks (Dickinson and Suczek, 1979). Potential source terranes of the study area include Paleozoic and Mesozoic sedimentary rocks exposed in both the Sevier fold-and-thrust belt and Laramide ranges and Precambrian basement rocks distributed in the cores of Laramide ranges. The sedimentary rocks include the Cretaceous sandstone, siltstone, and chert-pebble conglomerate; Jurassic and Triassic eolian sandstone and marine limestone; Jurassic–Upper Permian glauconitic siltstone, sandstone, and limestone; Permian–Upper Cambrian limestone, dolostone, and sandstone, Middle-Upper Cambrian micaceous shale, and Cambrian quartzite (Love and Christiansen, 1985). The core of the Uinta Mountains in the Wyoming-Utah-Colorado border contains Neoproterozoic metasedimentary rocks of the Uinta Mountain Group, which includes arkosic sandstone, shale, and conglomerate (Dehler et al., 2005). Archean and Proterozoic

igneous and metamorphic rocks are exposed in the cores of other Laramide ranges surrounding the Greater Green River Basin (Love and Christiansen, 1985).

The lithic fragments of sandstone, siltstone and limestone were derived from the exposed Phanerozoic sedimentary strata around the basin. The small grain size, high sorting and rounding degree in the Fort Union Formation likely suggest relatively long transport distance from the source area. Sediments in this formation were most likely derived from the Sevier fold-and-thrust belt, consistent with the active movement of the Hogsback thrust during the Paleocene to early Eocene (DeCelles, 2004). Multiple previous studies have suggested that the Uinta Mountains was not a major topographic feature before the early middle Eocene (e.g., Norris et al., 1996; Wolfe et al., 1998; Fan and Dettman, 2009), thus not the primary source of sediments during the Paleocene. However, the abundant feldspar grains in the Wasatch Formation and northward paleoflow directions in our records suggest that Uinta Mountains experienced uplift, and the arkosic sandstones and conglomerates in the Uinta Mountain Group, which are distributed in the north part of the Uinta Mountains (Dehler et al., 2005), were exposed for erosion during the earliest Eocene. The feldspar grains are not from the other basin-bounding Laramide ranges because the Wasatch Formation does not contain much Precambrian basement lithics. This interpretation is consistent with the observation that the sediments in the Wasatch Formation have poor sorting and rounding and were likely deposited in a more proximal setting (Figure 3-4).

3.5 Oxygen isotope paleoaltimetry

Bulk carbonates and pedogenic carbonate nodules were collected from the measured stratigraphic sections for paleotopography study. The bulk carbonates in sandstone samples should be completely carbonate cement, thus we classify this group of samples as sandstone cement. The bulk carbonates in mudstone and siltstone samples were mostly deposited in floodplain environments and have experienced various degree of pedogenesis, and we classify this group of samples as mudstone cement. The mudstone cements contain a mixture of pedogenic carbonate and fluvial carbonate cement. These carbonates were characterized using cathodoluminescence microscope and X-ray diffraction (XRD) to evaluate diagenesis, and determine dominant carbonate species.

3.5.1 Methods

The bulk carbonate samples and pedogenic nodules were powdered using a ceramic mortar and pestle. Ten samples were taken from one sandstone specimen (FU-373) in the Fort Union Formation using hand drill to evaluate the possible influence of marine limestone clasts on bulk carbonate $\delta^{18}O$ value. Powdered samples were weighed and loaded into sample vials. After flushing the vials using ultrapure helium, dehydrated phosphoric acid was injected into the vials to react with the samples at 70 °C. The $\delta^{18}O$ values of the resulted CO_2 were analyzed using a Gasbench II and a Delta V Advantage Mass Spectrometer. The isotope ratios are calibrated using NBS-19, NBS-18, and an in house standard. The

precision of $\delta^{18}O$ and $\delta^{13}C$ is better than ±0.2 ‰ (1σ) based on repeated analysis of standards. All the isotope values of carbonate are reported relative to VPDB.

XRD was performed on 11 representative samples to evaluate carbonate species. Samples were powdered using a ceramic mortar and pestle and analyzed by a Bruker D8 Advance Diffractometer equipped with Cu(Kα) radiation at 40 keV and 40 mA to show diffraction patterns. Samples were scanned from 20 to 70 2θ at 0.02 steps. Carbonate mineralogy, including high-magnesium calcite, low-magnesium calcite, and dolomite were determined based on the position of d(104) peak. If more than one type of carbonate occurred, the ratios of different types of carbonate were estimated semi-quantitatively based on the peak heights of each type of carbonate.

In order to characterize carbonate texture, polished thin sections were made from four sandstone samples and two pedogenic carbonate samples, and were examined using both polarizing and cathodoluminescence microscopes. A reliotron cold cathodoluminoscope was operated at an acceleration voltage of 7–9 kV and a beam current intensity of 0.3–0.5 mA to inspire the luminescence of carbonate.

3.5.2 Results

XRD results show that samples in the Fort Union Formation and the lower Wasatch Formation contain predominantly low-magnesium calcite with less than 30% dolomite, while samples in the upper 200 m of the main body of the Wasatch

Formation have amount of dolomite varying from 50% to 100% (Figure 3-6). The $\delta^{18}O$ values of carbonates seem to be positively related to dolomite content (Figure 3-6).

The pedogenic carbonate nodules are mostly micritic with a small amount of spars up to 60 μm in diameter under a polarizing microscope (Figure 3-7F and H). The micrite displays clotted fabrics of variable degree of red luminescence, and the variation seems to be related to clay content (Figure 3-7E and G). The intergranular carbonate cements in the Fort Union Formation and the lower part of the Wasatch Formation are mainly micritic, and the ones in the upper part of the Wasatch Formation contain spars (Figure 3-7B and D). Under cathodoluminescence light, the micritic carbonate cements in the sandstone samples show red luminescence without prominent intensity difference and the spars do not have zonation (Figure 3-7A and C). No rhomboid dolomite crystals present in any of the studied thin sections.

The Paleocene Fort Union Formation has no pedogenic carbonate. The $\delta^{18}O$ values of sandstone cements in the Fort Union Formation vary between -13.2 ‰ and -7.6 ‰ (Figure 3-8A). The $\delta^{18}O$ and $\delta^{13}C$ values of the pedogenic carbonate in the lower Eocene Wasatch Formation range from -9.8 ‰ to -8.5 ‰, and from -8.0 ‰ to -6.6 ‰, respectively (Figure 3-8B). The $\delta^{18}O$ values of sandstone cements and mudstone cements in the lower Eocene Wasatch Formation range from -18.1 ‰ to -10.3 ‰, and from -13.9 ‰ to -4.4 ‰, respectively (Figure 3-

8B). The lowest $\delta^{18}O$ values show a clear decreasing trend through time after ~60 Ma (Figure 3-9). The variation of $\delta^{18}O$ values of the sandstone specimen (FU-373) used to evaluate limestone clasts influence is less than 1 ‰ (Table 3-4).

3.5.3 Interpretation

Screening carbonate diagenesis

Diagenesis needs to be evaluated before interpreting isotope compositions of carbonates. Carbonate cements of siliciclastic sedimentary rocks were classified as eodiagenetic, mesodiagenetic, and telodiagenetic carbonates (Choquette and Pray, 1970). Eodiagenesis is early diagenesis, and takes place before sediments are buried and compacted, and the stable isotope compositions of eodiagenetic carbonates record surface temperature and water isotope compositions soon after the deposition of silisiclastic grains (Choquette and Pray, 1970). Mesodiagenesis occurs after burial, under elevated temperature and pressure, and the stable isotope compositions of mesodiagenetic carbonate might reflect the temperature and isotope compositions of diagenetic fluid deep in sedimentary basins (Choquette and Pray, 1970; Brand and Veizer, 1981). Telodiagenesis occurs near the surface, but during post-burial uplift and associated erosion, and the stable isotope compositions of telodiagenetic carbonate record the most recent surface temperature and water isotopic compositions (e.g., Morad, 1998). Therefore, only eodiagenetic carbonate cement can be used to infer paleoelevation during the deposition.

Several lines of evidence suggest that the carbonates in our samples were formed primarily during eodiagenesis. First, undeformed ductile grains such as muscovite, biotite and unaltered feldspar grains present in the sandstone samples (Figure 3-4). These minerals tend to be altered to clay minerals if mesogenesis occurred (e.g., Morad, 1998). Second, carbonate cement accounts for about 40% of the rock volume in some sandstone samples, which is equivalent to the average original porosity of sandstone (Sclater and Christie, 1980), suggesting that the samples had not been compacted by deep burial when the carbonate cement was formed. Third, carbonate samples at nearby stratigraphic levels and of different type show distinct isotope compositions indicating that there was no mesodiagenesis and eodiagnesis. This inference is based on that diagenesis tends to reset the original isotope compositions to similar values. Fourth, numerous studies have suggested that the carbonates in the middle Eocene Green River Formation, which overlies the Wasatch Formation and was deposited in both hydrologically open and closed lacustrine environments, have preserved original lake water isotope compositions (Carroll et al., 2008). Therefore, the carbonates in our samples were formed *in situ* or as eodiagenetic cements, and their isotope compositions should retain the ancient surface water isotope compositions.

We suggest that our carbonate cements were formed in both vadose zone and phreatic zone. Vadose zone cement usually displays dense micritic fabric, while phreatic cement has blocky spar filling isolated vugs and the remaining pore

spaces surrounded by micrite (Wright and Tucker, 1991; Beckner and Mozley, 1998). Our samples from the Fort Union Formation and the lower part of the Wasatch Formation mainly contain micritic cement, indicating deposition of carbonate in vadose zone. The cement in the upper part of the Wasatch Formation contains more spars, indicating carbonate formation in both vadose and phreatic zones when groundwater level fluctuated. Minor chemical constituents control cathodoluminescence intensity. Mn^{2+} and possibly rare earth elements activate luminescence, and Fe^{2+} quenches luminescence (Habermann et al., 2000; Machel, 2000). The presence of these elements is related to redox and pH conditions of fluid, and therefore one can use the color of luminescence to infer the condition under which the carbonate precipitated (Machel and Burton, 1991; Solomon and Walkden, 1985). The vadose zone is usually an oxidizing environment and contains low levels of divalent Mn and Fe, resulting in carbonate with low-intensity luminescence. In contrast, phreatic zone in reducing environment likely contains high levels of divalent Mn, and carbonate formed only when the divalent Fe concentration is low displays bright luminescence. However, carbonate formed in vadose zone may have bright luminescence when Mn^{2+} content exceeds Fe^{2+} content. Our sandstone cements and paleosol carbonates all have bright luminescence. We suggest that the bright luminescence in the micritic carbonate formed in vadose zone reflect higher abundance of Mn^{2+} than Fe^{2+}.

Presence of dolomite

Varying amount of dolomite present in many of our samples (Figure 3-6), and we suggest the dolomite were authigenic. Dolomite can be diagenetic or authigenic. Original high-magnesium calcites or "protodolomite" can be replaced by dolomite, and dolomitization can also occur through the reaction of limestone with basinal brines during deep burial (Warren, 2000). Such diagenetic dolomite usually exhibits coarse, rhombic crystals with chemical zonation caused by water–sediment interaction (e.g., Solomon and Walkden, 1985; Driese and Mora, 1993). Because we did not observe these features, the dolomite in our samples was not likely caused by diagenesis. Authigenic dolomite can be deposited in lacustrine environments when Mg/Ca ratio of lake water is high due to evaporation (e.g., Kohut et al., 1995; Capo et al., 2000; Last et al., 2012); in saline soils or soils developed on basalt when Mg/Ca ratio of soil water is high due to evaporation or bedrock dissolution (VanDeVelde et al., 2013); and by low-temperature microbial precipitation (Roberts et al., 2004; Sánchez-Román et al., 2008). Our carbonate cement samples in the fluvial Fort Union Formation and the lower part of the Wasatch Formation contain a small amount of dolomite, and the dolomite are associated with pedogenic features like leached soil horizons and peds structures, suggesting saline soil or low-temperature microbial precipitation of these dolomites. Dolomites in the upper part of the Wasatch Formation are

associated with gypsum, and high $\delta^{13}C$ values, suggesting saline lake origin of these dolomites.

Carbonate and water $\delta^{18}O$ values

Pedogenic carbonates were formed in isotopic equilibrium with soil water during warm seasons, and therefore their $\delta^{18}O$ values record the $\delta^{18}O$ values of ancient local precipitation ($\delta^{18}O_p$) with potential bias to summer time (e.g., Quade and Cerling, 1993; Quade et al., 2007; Breeker et al., 2009; Hough et al., 2014). Fluvial carbonate cements were formed under equilibrium with groundwater, and therefore their $\delta^{18}O$ values record the $\delta^{18}O$ values of ancient groundwater (e.g., Talbot, 1990; Quade and Roe, 1999). Groundwater is a mixture of local basinal precipitation and distal precipitation or snowmelt on surrounding mountains. These two types of water have distinct $\delta^{18}O$ values because the isotopic fractionation associated with Rayleigh distillation resulting in a progressive depletion of ^{18}O in the remaining vapor when the vapor mass is lifted to across high elevation (e.g., Dansgaard, 1953; Garzione and Rowley, 2007). The small variation of $\delta^{18}O$ values in the sandstone specimen FU-373 suggests that the cement samples were not influenced by marine limestone grains, which is consistent with our observation that limestone grains count only a small component (less than 1%) in our samples.

The variations of the $\delta^{18}O$ values of our sandstone and mudstone cements show that the samples can be divided into three groups (Figure 3-8B). The first

group has similar isotope compositions to those of the pedogenic carbonates, suggesting that this group of carbonates were formed in equilibrium with basinal precipitation or groundwater dominated by basinal precipitation. The second group has isotope values higher than those of pedogenic carbonates, suggesting that the group was formed in water that experienced variable degree of evaporation. The last group has lower $\delta^{18}O$ values than those of pedogenic carbonates, suggesting that this group of carbonates were formed in equilibrium with groundwater or river water charged by a mixture of highland precipitation or snowmelt and basinal precipitation. Therefore, the lowest $\delta^{18}O$ values in this group represent carbonate formation in highland precipitation, with minimum influence of basinal precipitation. The carbonates with variable $\delta^{18}O$ values between the lowest $\delta^{18}O$ values and pedogenic carbonate $\delta^{18}O$ values were deposited by water with variable degree of mixing between highland precipitation and basinal precipitation.

By using the oxygen isotope fractionation relationship between water and calcite (Kim and O'Neil, 1997), and soil carbonate formation temperature of 35 °C based on a clumped-isotope temperature study in the lower Eocene Willwood Formation in the Bighorn Basin (Snell et al., 2013), the $\delta^{18}O$ value of soil water is estimated to be in the range of -5.5 ‰ to -4.2 ‰. These values are consistent with the reconstructed surface water $\delta^{18}O$ values from the group of mudstone and sandstone cements formed in basinal precipitation (Figure 3-9), and thus should

be very close to the mean annual precipitation $\delta^{18}O$ on the basin floor. This temperature estimate is 18 °C higher than the mean annual temperature estimated from leaf margin analysis (Wing et al., 2000 and 2005) because pedogenic carbonate precipitation favors summer season in the central Rockies (Hough et al., 2014). Although there is no published estimate of crystallization temperature for groundwater carbonate cement, it is generally agreed that shallow-ground water carbonate precipitates between mean annual and mean warm season temperatures (e.g., Roe and Quade, 1999). One early middle Eocene lacustrine oolitic limestone in the Green River Formation experienced early diagenesis, and its clumped isotope temperature is 32 °C (Fan et al., 2014), suggesting eodiagenetic carbonate cement may bias toward warm seasons. Here we consider both scenarios of warm season and mean annual carbonate precipitation temperatures when estimating $\delta^{18}O$ values of groundwater based on mudstone and sandstone cement $\delta^{18}O$ values. The calculated water $\delta^{18}O$ values range from -13.8 ‰ to 0 ‰, and from -17.4 ‰ to -3.6 ‰, respectively.

High earliest Eocene paleorelief between the Uinta Mountains and Greater Green River Basin

We reconstruct the paleorelief between the Uinta Mountains and Greater Green River Basin during the earliest Eocene using two approaches. The first approach constrains paleorelief based on a thermodynamic model of Rayleigh condensation (Figure 3-10A; Rowley, 2007). Atmospheric thermodynamics of a

simple air parcel predicts a polynomial regression between $\Delta(\delta^{18}O_p)$ and elevation, and the $\Delta(\delta^{18}O_p)$ is the difference in isotopic compositions of highland precipitation and sea-level precipitation (Rowley et al., 2001; Rowley, 2007). The model considers all possible sea-surface temperature and relative humidity, which determine water vapor concentration of the starting air mass (Rowley, 2007). The regression is verified by modern $\Delta(\delta^{18}O_p)$ values and elevation data in the Himalaya and eastern flank of Andes in Bolivia where initial starting condition of the air mass is simple (Rowley and Garzione, 2007). In this study, the $\delta^{18}O$ values of basinal precipitation and highland precipitation were calculated from paleosol carbonate $\delta^{18}O$ values and lowest fluvial cement $\delta^{18}O$ values, respectively; and the differences between their isotopic compositions were used to constrain the paleorelief between the Greater Green River Basin and the Uinta Mountains.

Before calculating paleorelief using the modern empirical $\Delta(\delta^{18}O_p)$-elevation relationship, we evaluate the assumptions influencing this practice. The assumptions to use $\Delta(\delta^{18}O_p)$ values to constrain the paleorelief between the Greater Green River Basin and the Uinta Mountains include that 1) the moistures in our study site were from low latitude (<35°) where temperature and relative humidity of ocean water are well represented in the thermodynamic model; 2) the waters in both lowland and highland were from the same air parcel and no other vapor of different isotopic compositions were mixed (Rowley and Garzione,

2007). During the early Paleogene, the North American Cordillera was at least at moderate elevation because of prolonged crustal shortening and thickening during the Cretaceous-early Paleogene (e.g., DeCelles, 2004; Chamberlain et al., 2012), and the Mississippian embayment was farther north than today (Stearns, 1957), leading to strong summer monsoon derived from the Gulf of Mexico (Sewall and Sloan, 2006; Chamberlain et al., 2012; Feng et al., 2013). The paleoclimate in Wyoming was humid during the early Paleogene based on a paleofloras study and the estimated mean annual precipitation is more than 1 m (Wilf, 2000). Vapor recycling was very unlikely a major source of water vapor in the study area. Therefore, the paleogeography, humid climate, and strong Paleogene monsoon derived from low latitude favor the application of the regression in our study site.

We use the average value of the soil water $\delta^{18}O$ values, -5.0 ‰, to represent the low elevation precipitation $\delta^{18}O$ value. We then use the lowest river water $\delta^{18}O$ value, -13.8 ‰ under warm season carbonate precipitation temperature, and -17.4 ‰ under mean annual carbonate precipitation temperature, to represent the highland precipitation isotopic composition. Based on the thermodynamic-based Rayleigh model and using the $\Delta(\delta^{18}O_p)$ values of -8.8 ‰ based on warm season carbonate cement precipitation temperature or -12.4 ‰ based on mean annual carbonate cement precipitation temperature, the paleorelief is estimated to be 3.3-4.7 km, or 3.9-5.7 km (Figure 3-10A). Given that clumped isotope temperature data supports warm-season bias of early diagenetic cement (Fan et al., 2014), the

paleorelief between the Uinta Mountains and the greater Green River basin is most likely on the order of 4 km.

Although the thermodynamic model of Rayleigh condensation suggests the paleorelief between the Greater Green River Basin and Unita Mountains maybe more than 4 km during the early Eocene, this practice may overestimate the paleorelief due to two climate factors that are not considered in a simple Rayleigh distillation model. First, snow, which is the main form of precipitation on highlands, is more depleted in ^{18}O compared to other precipitation types, and the subsequent isotopic exchange between snowfall and environment through evaporation, mixing, and recondensation is significantly reduced (Jouzel and Merlivat, 1984; Gat, 2010; Lechler and Niemi, 2010). Second, convective precipitation is enriched in ^{18}O compared to large-scale precipitation, and convective precipitation is common on lowlands and highland flanks but not on highland top during the early Eocene (Feng et al., 2013). The net influence of ^{18}O-depleted snow and convective precipitation on highlands can reduce the total $\delta^{18}O_p$ value 2-6 ‰ (Feng et al., 2013).

The second approach considers vapor mixing caused by vertical and horizontal advection of air masses and recycling in the eastern flank of the Cordillera during the Paleogene (Feng et al., 2013). By comparing our estimated water $\delta^{18}O$ values with modeled precipitation $\delta^{18}O$ values at various elevations using isotope-enabled global climate model at our studied latitude, we constrain

the paleoelevations of the mountains and basin floor based on the absolute $\delta^{18}O$ values of the highland and basinal precipitations (Figure 3-10B). Our reconstructed soil water $\delta^{18}O$ value is -5.0 ‰, which is at least 2.5 ‰ higher than the modeled sea-level mean annual precipitation $\delta^{18}O$ values at our studied latitude (Feng et al., 2013), suggesting the basin floor elevation was low, no more than ~500 m. Our highland precipitation $\delta^{18}O$ value (-13.8 ‰ based on warm season carbonate precipitation temperature or -17.4 ‰ based on mean annual carbonate precipitation temperature) leads to a paleoelevation estimate of at least 3.5 km, possibly 3.5-4.5 km for the Uinta Mountains during the earliest Eocene. Therefore, both approaches suggest that the paleorelief between the Uinta Mountains and the Greater Green River Basin was high, on the order of ~4 km during the earliest Eocene. This result shows that the high elevation of the Uinta Mountains established during ~55-53 Ma, which is 4-6 Myr older than the previous records of ~49 Ma (Norris et al., 1996; Wolfe et al., 1998; Fan and Dettman, 2009).

3.6 Discussion

Our oxygen isotopic trend suggests that the Uinta Mountains started to gain elevation during the late Paleocene, after ~61 Ma (Figure 3-9), and a high elevation of ~4 km was attained by 53 Ma. The establishment of high topography of the Uinta Mountains during the earliest Eocene was coeval with the changes to proximal braided river depositional environment, the generally northward

paleoflow directions, and the presence of Proterozoic-basement derived sediments, suggesting that surface uplift was associated with rock uplift and unroofing of the Proterozoic basement in the Uinta Mountains during this period. A similar study in the Wind River Basin, to the north of the Greater Green River Basin, suggests that surface uplift and unroofing of the Wind River Range also occurred during the early Eocene (Fan et al., 2011). These observations support a previous hypothesis that the Laramide ranges experienced accelerated deformation during the late Paleocene-early Eocene (Fan and Carrapa, 2014). The elevation gain of the Wind River Range and Uinta Mountains during the early Eocene is younger than that of the Bighorn Mountains during the late Paleocene (Fan and Dettman, 2009).

The intensified earliest Eocene Laramide deformation and an earlier initiation of the deformation are consistent with the exhumation records of the Wind River Range to the north of the Greater Green River Basin. Several recent theromochronology studies have suggested that the Wind River Range experienced fast exhumation during 65-50 Ma (Peyton et al., 2012; Fan and Carrapa, 2014; Stevens et al., 2016). The direct consequence of the intense surface uplift and exhumation of the Laramide mountain ranges during the early Eocene is that Precambrian basement controlled early and early middle Eocene river and lake water geochemistry (e.g., Rhodes et al., 2002; Carroll et al., 2006; Davis et al., 2008; Fan et al., 2011b).

Our results also contribute to the understanding of the topography of Sevier orogen. Substantial amount of structural evidence supports the existence of a broad Nevadaplano with at least moderate elevation before the early Eocene (e.g., DeCelles, 2004; DeCelles and Coogan, 2006). A recent paleoelevation reconstruction of the Nevadaplano, based on carbonate clumped isotope temperatures, supports the existence of a plateau higher than 2 km during the latest Cretaceous (Snell et al., 2014). Therefore, it is very likely that the rivers or groundwater from the Sevier orogenic front, and possibly hinterland, dominated surface water $\delta^{18}O$ values in the Greater Green River Basin before the uplift of the Laramide mountain ranges. A high Nevadaplano in warm Paleogene climate, and northward location of the Mississippian embayment should favor strong monsoonal climate during the early Paleogene (Sewall and Sloan, 2006; Chamberlain et al., 2012), influencing highland precipitation and dominating river water or groundwater $\delta^{18}O$ values in the Greater Green River Basin. Such a scenario has been documented in several studies in the Miocene Himalayan foreland basin. With high basin-bounding topography and strong monsoon climate, the Miocene Himalayan foreland basin had similar tectonic and climate settings to the early Paleogene Cordilleran foreland. The $\delta^{18}O$ values of sandstone cements formed in water derived from the Himalaya highland are ~6 ‰ lower than those of pedogenic carbonates formed in basinal precipitation (e.g., Singh et al., 2014). However, the sandstone cement $\delta^{18}O$ values are consistently high in

our record during the early Paleocene, suggesting the lack of high topography in the Sevier orogen to the west of Wyoming. Such an inference is consistent with the interpretation of stable isotope records from the Axehandle Basin and Uinta Basin in Utah and the Sage Creek Basin in southwest Montana (Davis et al., 2008; Chamberlain et al., 2012; VanDevelde and Bowen, 2014), and a clumped isotope record in the Sheep Pass Basin in east-central Nevada (Lechler et al., 2013). This interpretation seems to support the hypothesis that the Cordilleran orogen had rugged topography during the early Paleocene and maximum hinterland elevation was gained to the west of Wyoming after the early Eocene (Mix et al., 2001; Chamberlain et al., 2012; Lechler et al., 2013). We note that it is possible that our samples from the Fort Union Formation were too far from the truck streams originated on the Sevier orogen, and we simply missed the stable isotopic signals of the water derived from the Sevier.

Our results provide new paleogeographic reconstructions to the Greater Green River Basin during the earliest Eocene, and thereby help to understand the large-scale drainage reorganization in the North American Cordilleran system during the Sevier-Laramide transition. During the Late Cretaceous, the Greater Green River Basin had rivers draining northeastward from Utah and Colorado and southeastward from Montana and Idaho (e.g., Hansen, 1965, 1985; Steidtmann, 1969; Dorr Jr. et al., 1977; Stanley and Collinson, 1979; Moncure and Surdam, 1980; Cole, 1985; Sklenar and Anderson, 1985; Roehler, 1993) (Figure 3-11A).

During the late Paleocene, our $\delta^{18}O$ record shows that the Uinta Mountains start to gain topography. Given that the exhumation of the Wind River Range during the early Paleocene (Peyton et al., 2012; Fan and Carrapa, 2014; Stevens et al., 2016), the range may be at moderate elevation during the late Paleocene. Surface uplifts of the Uinta Mountains and Wind River Range changed the generally eastward-flowing river system by adding northward and southward rivers in the basin (Figure 3-11B). During the earliest Eocene, as the Uinta Mountains reached high topography (~4 km), the Greater Green River Basin experienced rapid subsidence (e.g., Fan and Carrapa, 2014; Gao et al., 2016). The Wind River Range also reached high topography (~3.5 km) during this period (Fan et al., 2011a). Northward-flowing braided rivers from the Uinta Mountains may dominate the drainage pattern in the southern part of the basin, while southward-flowing rivers from the Wind River Range may dominate the drainage pattern in the northern part of the basin during the earliest Eocene (Surdam and Wolfbauer, 1975; Carroll et al., 2008; Davis et al., 2008) (Figure 3-11C).

3.7 Conclusions

The western portion of the central Rocky Mountains in Wyoming was influenced by the contemporary thin-skinned Sevier and thick-skinned Laramide orogenies during the latest Cretaceous-early Eocene. Studies of depositional environments, sediment provenance and paleoelevation are critical to the understanding of paleogeography and influence of each orogeny on basin

evolution. Here we conduct lithofacies analysis, sediment provenance and paleoelevation studies to the lower Paleogene Fort Union and the main body of the Wasatch formations in the center of the Greater Green River Basin in order to reconstruct paleogeography and paleotopography in southwestern Wyoming during the entire early Paleogene. The depositional environment evolved from a low-energy meandering river to high-energy braided rivers from the Paleocene to the earliest Eocene. Sandstone petrography results show that the sandstones in the Paleocene strata are all dominated by monocrystalline quartz gains, while the lowermost Eocene Wasatch Formation has larger grain size, poorer sorting and rounding, and more feldspar grains. The change in sediment provenance and presence of dominant northward paleoflow direction suggest that the Uinta Mountains to the south of the Greater Green River Basin controlled the fluvial drainage pattern during the earliest Eocene. Our authigenic carbonate $\delta^{18}O$ values were stable and high during the early Paleocene, became lower during the late Paleocene and reached the lowest values during the earliest Eocene. By using both Rayleigh condensation model and predictions of Eocene precipitation isotope values using an isotope-enabled global climate model, we estimated the paleoelevation of the Uinta Mountains was on the order of 4 km during the earliest Eocene. Put our data and previous published data together, we suggest that the accelerated uplift of the Uinta Mountains adjusted the fluvial drainage pattern in the center of the Greater Green River Basin during the earliest Eocene.

The consistently high $\delta^{18}O$ values and lack of high topography during the early Paleocene suggest that the Cordilleran orogen to the west of Wyoming may have rugged hinterland topography during the Paleocene.

Acknowledgements

We thank Patricia Garay and Lu Zhu for field assistance and Jackie Garcia for laboratory assistance. This research was funded by a Geological Society of America student research grant.

References

Beck, R.A., Vondra, C.F., Filkins, J.E., and Olander, J.D., 1988, Syntectonic sedimentation and Laramide basement thrusting, Cordilleran foreland; timing of deformation: Geological Society of America Memoirs, v. 171, p. 465-488.

Beckner, J., and Mozley, P., 2009, Origin and spatial distribution of early vadose and phreafic calcite cements in the Zia Formation, Albuquerque Basin, New Mexico, USA: Carbonate Cementation in Sandstones: Distribution Patterns and Geochemical Evolution (Special Publication 26 of the IAS), v. 72, p. 27.

Brand, U., and Veizer, J., 1981, Chemical diagenesis of a multicomponent carbonate system-2: stable isotopes: Journal of Sedimentary Research, v. 51, .

Breecker, D., Sharp, Z., and McFadden, L.D., 2009, Seasonal bias in the formation and stable isotopic composition of pedogenic carbonate in modern soils from central New Mexico, USA: Geological Society of America Bulletin, v. 121, p. 630-640.

Breithaupt, B.H., 1982, Paleontology and paleoecology of the Lance Formation (Maastrichtian), east flank of Rock Springs Uplift, Sweetwater County, Wyoming: Rocky Mountain Geology, v. 21, p. 123-151.

Bridge, J.S., 1984, Large-scale facies sequences in alluvial overbank environments: Journal of Sedimentary Research, v. 54, .

Buol, S., Hole, F., and McCracken, R., 1980, Soil genesis and classification: Iowa University: .

Capo, R.C., Whipkey, C.E., Blachère, J.R., and Chadwick, O.A., 2000, Pedogenic origin of dolomite in a basaltic weathering profile, Kohala peninsula, Hawaii: Geology, v. 28, p. 271-274.

Carroll, A.R., Chetel, L.M., and Smith, M.E., 2006, Feast to famine: Sediment supply control on Laramide basin fill: Geology, v. 34, p. 197-200.

Carroll, A.R., Doebbert, A.C., Booth, A.L., Chamberlain, C.P., Rhodes-Carson, M.K., Smith, M.E., Johnson, C.M., and Beard, B.L., 2008, Capture of high-altitude precipitation by a low-altitude Eocene lake, western US: Geology, v. 36, p. 791-794.

Cerling, T.E., and Quade, J., 1993, Stable carbon and oxygen isotopes in soil carbonates: Climate Change in Continental Isotopic Records, p. 217-231.

Cerveny, P.F., and Steidtmann, J.R., 1993, Fission track thermochronology of the Wind River Range, Wyoming: evidence for timing and magnitude of Laramide exhumation: Tectonics, v. 12, p. 77-91.

Chamberlain, C.P., Mix, H.T., Mulch, A., Hren, M.T., Kent-Corson, M.L., Davis, S.J., Horton, T.W., and Graham, S.A., 2012, The Cenozoic climatic and topographic evolution of the western North American Cordillera: American Journal of Science, v. 312, p. 213-262.

Choquette, P.W., and Pray, L.C., 1970, Geologic nomenclature and classification of porosity in sedimentary carbonates: AAPG Bulletin, v. 54, p. 207-250.

Clyde, W.C., Zonneveld, J., Stamatakos, J., Gunnell, G.F., and Bartels, W.S., 1997, Magnetostratigraphy across the Wasatchian/Bridgerian NALMA boundary (early to middle Eocene) in the western Green River basin, Wyoming: The Journal of Geology, v. 105, p. 657-670.

Crews, S.G., and Ethridge, F.G., 1993, Laramide tectonics and humid alluvial fan sedimentation, NE Uinta Uplift, Utah and Wyoming: Journal of Sedimentary Research, v. 63, .

Dansgaard, W., 1953, The abundance of O18 in atmospheric water and water vapour: Tellus, v. 5, p. 461-469.

Davis, S.J., Mix, H.T., Wiegand, B.A., Carroll, A.R., and Chamberlain, C.P., 2009, Synorogenic evolution of large-scale drainage patterns: Isotope paleohydrology of sequential Laramide basins: American Journal of Science, v. 309, p. 549-602.

Davis, S.J., Mulch, A., Carroll, A.R., Horton, T.W., and Chamberlain, C.P., 2009, Paleogene landscape evolution of the central North American Cordillera: Developing topography and hydrology in the Laramide foreland: Geological Society of America Bulletin, v. 121, p. 100-116.

Davis, S.J., Wiegand, B.A., Carroll, A.R., and Chamberlain, C.P., 2008, The effect of drainage reorganization on paleoaltimetry studies: An example from the Paleogene Laramide foreland: Earth and Planetary Science Letters, v. 275, p. 258-268.

DeCelles, P.G., 2004, Late Jurassic to Eocene evolution of the Cordilleran thrust belt and foreland basin system, western USA: American Journal of Science, v. 304, p. 105-168.

DeCelles, P.G., Gray, M., Ridgway, K., Cole, R., Pivnik, D., Pequera, N., and Srivastava, P., 1991, Controls on synorogenic alluvial-fan architecture, Beartooth Conglomerate (Palaeocene), Wyoming and Montana: Sedimentology, v. 38, p. 567-590.

Dehler, C.M., Sprinkel, D.A., and Porter, S.M., 2005, Neoproterozoic Uinta Mountain Group of northeastern Utah: Pre-Sturtian geographic, tectonic, and biologic evolution: Field Guides, v. 6, p. 1-25.

Dickinson, W.R., Beard, L.S., Brakenridge, G.R., Erjavec, J.L., Ferguson, R.C., Inman, K.F., Knepp, R.A., Lindberg, F.A., and Ryberg, P.T., 1983, Provenance of North American Phanerozoic sandstones in relation to tectonic setting: Geological Society of America Bulletin, v. 94, p. 222-235.

Dickinson, W.R., Klute, M.A., Hayes, M.J., Janecke, S.U., Lundin, E.R., McKITTRICK, M.A., and Olivares, M.D., 1988, Paleogeographic and paleotectonic setting of Laramide sedimentary basins in the central Rocky Mountain region: Geological Society of America Bulletin, v. 100, p. 1023-1039.

Dickinson, W.R., and Snyder, W.S., 1978, Plate tectonics of the Laramide orogeny: Geological Society of America Memoirs, v. 151, p. 355-366.

Dickinson, W.R., and Suczek, C.A., 1979, Plate tectonics and sandstone compositions: AAPG Bulletin, v. 63, p. 2164-2182.

Driese, S.G., and Mora, C.I., 1993, Physico-chemical environment of pedogenic carbonate formation in Devonian vertic palaeosols, central Appalachians, USA: Sedimentology, v. 40, p. 199-216.

Fan, M., and Carrapa, B., 2014, Late Cretaceous–early Eocene Laramide uplift, exhumation, and basin subsidence in Wyoming: Crustal responses to flat slab subduction: Tectonics, v. 33, p. 509-529.

Fan, M., DeCelles, P.G., Gehrels, G.E., Dettman, D.L., Quade, J., and Peyton, S.L., 2011, Sedimentology, detrital zircon geochronology, and stable isotope geochemistry of the lower Eocene strata in the Wind River Basin, central Wyoming: Geological Society of America Bulletin, v. 123, p. 979-996.

Fan, M., and Dettman, D.L., 2009, Late Paleocene high Laramide ranges in northeast Wyoming: Oxygen isotope study of ancient river water: Earth and Planetary Science Letters, v. 286, p. 110-121.

Fan, M., Hough, B.G., and Passey, B.H., 2014, Middle to late Cenozoic cooling and high topography in the central Rocky Mountains: Constraints from

clumped isotope geochemistry: Earth and Planetary Science Letters, v. 408, p. 35-47.
Fan, M., Quade, J., Dettman, D., and DeCelles, P.G., 2011, Widespread basement erosion during the late Paleocene–early Eocene in the Laramide Rocky Mountains inferred from 87Sr/86Sr ratios of freshwater bivalve fossils: Geological Society of America Bulletin, v. 123, p. 2069-2082.
Feng, R., Poulsen, C.J., Werner, M., Chamberlain, C.P., Mix, H.T., and Mulch, A., 2013, Early Cenozoic evolution of topography, climate, and stable isotopes in precipitation in the North American Cordillera: American Journal of Science, v. 313, p. 613-648.
Fidlar, M.M., 1950, Structural Features of the Green River Basin: .
Gao, M., Fan, M., and Moucha, R., 2016, Southwestward weakening of Wyoming lithosphere during the Laramide orogeny: Journal of Geophysical Research: Solid Earth, v. 121, p. 6219-6234.
Gat, J.R., 2010, Isotope hydrology: a study of the water cycle: World Scientific, .
Graham, S.A., Ingersoll, R.V., and Dickinson, W.R., 1976, Common provenance for lithic grains in Carboniferous sandstones from Ouachita Mountains and Black Warrior Basin: Journal of Sedimentary Research, v. 46, .
Gurnis, M., 1992, Rapid continental subsidence following the initiation and evolution of subduction: Science, v. 255, p. 1556.
Habermann, D., Götte, T., Meijer, J., Stephan, A., Richter, D., and Niklas, J., 2000, High resolution rare-earth elements analyses of natural apatite and its application in geo-sciences: combined micro-PIXE, quantitative CL spectroscopy and electron spin resonance analyses: Nuclear Instruments and Methods in Physics Research Section B: Beam Interactions with Materials and Atoms, v. 161, p. 846-851.
Hansen, W., 1986, History of faulting in the eastern Uinta Mountains, Colorado and Utah: New Interpretations of Northwest Colorado Geology: Rocky Mountain Association of Geologists, p. 5-17.
Hough, B.G., Fan, M., and Passey, B.H., 2014, Calibration of the clumped isotope geothermometer in soil carbonate in Wyoming and Nebraska, USA: Implications for paleoelevation and paleoclimate reconstruction: Earth and Planetary Science Letters, v. 391, p. 110-120.
Ingersoll, R.V., Bullard, T.F., Ford, R.L., Grimm, J.P., Pickle, J.D., and Sares, S.W., 1984, The effect of grain size on detrital modes: a test of the Gazzi-Dickinson point-counting method: Journal of Sedimentary Research, v. 54, p. 103-116.
Jones, C.H., Farmer, G.L., Sageman, B., and Zhong, S., 2011, Hydrodynamic mechanism for the Laramide orogeny: Geosphere, v. 7, p. 183-201.
Jordan, T.E., 1981, Thrust loads and foreland basin evolution, Cretaceous, western United States: AAPG Bulletin, v. 65, p. 2506-2520.

Jouzel, J., and Merlivat, L., 1984, Deuterium and oxygen 18 in precipitation: Modeling of the isotopic effects during snow formation: Journal of Geophysical Research: Atmospheres, v. 89, p. 11749-11757.

Kauffman, E.G., 1977, Geological and biological overview: Western Interior Cretaceous basin: The Mountain Geologist, .

Kim, S., and O'Neil, J.R., 1997, Equilibrium and nonequilibrium oxygen isotope effects in synthetic carbonates: Geochimica Et Cosmochimica Acta, v. 61, p. 3461-3475.

Kohut, C., Dudas, M., and Muehlenbachs, K., 1995, Authigenic dolomite in a saline soil in Alberta, Canada: Soil Science Society of America Journal, v. 59, p. 1499-1504.

Kraus, M.J., 1999, Paleosols in clastic sedimentary rocks: their geologic applications: Earth-Science Reviews, v. 47, p. 41-70.

Last, F.M., Last, W.M., and Halden, N.M., 2012, Modern and late Holocene dolomite formation: Manito Lake, Saskatchewan, Canada: Sedimentary Geology, v. 281, p. 222-237.

Lechler, A.R., and Niemi, N.A., 2011, Controls on the spatial variability of modern meteoric δ18O: empirical constraints from the western US and East Asia and implications for stable isotope studies: American Journal of Science, v. 311, p. 664-700.

Lechler, A.R., Niemi, N.A., Hren, M.T., and Lohmann, K.C., 2013, Paleoelevation estimates for the northern and central proto–Basin and Range from carbonate clumped isotope thermometry: Tectonics, v. 32, p. 295-316.

Levey, R.A., 1985, Depositional model for understanding geometry of Cretaceous coals: major coal seams, Rock Springs Formation, Green River Basin, Wyoming: AAPG Bulletin, v. 69, p. 1359-1380.

Liu, L., Gurnis, M., Seton, M., Saleeby, J., Müller, R.D., and Jackson, J.M., 2010, The role of oceanic plateau subduction in the Laramide orogeny: Nature Geoscience, v. 3, p. 353-357.

Liu, L., Spasojevic, S., and Gurnis, M., 2008, Reconstructing Farallon plate subduction beneath North America back to the Late Cretaceous: Science (New York, N.Y.), v. 322, p. 934-938, doi: 10.1126/science.1162921 [doi].

Liu, S., and Nummedal, D., 2004, Late Cretaceous subsidence in Wyoming: Quantifying the dynamic component: Geology, v. 32, p. 397-400.

Liu, S., Nummedal, D., and Liu, L., 2011, Migration of dynamic subsidence across the Late Cretaceous United States Western Interior Basin in response to Farallon plate subduction: Geology, v. 39, p. 555-558.

Livaccari, R.F., Burke, K., and Şengör, A., 1981, Was the Laramide orogeny related to subduction of an oceanic plateau?

Love, J., and Christiansen, A., 1985, Geologic map of Wyoming, explanation for the geologic map, and principal sources of geologic data and references cited for geologic map of Wyoming: US Geologic Survey, .

Love, J.D., 1970, Cenozoic Geology of the Granite Mountains Area, Central Wyoming, .

Machel, H.G., 2000, Application of cathodoluminescence to carbonate diagenesis, in Cathodoluminescence in geosciences: Springer, p. 271-301.

Machel, H.G., and Burton, E.A., 1991, Factors governing cathodoluminescence in calcite and dolomite, and their implications for studies of carbonate diagenesis: .

Mack, G.H., James, W.C., and Monger, H.C., 1993, Classification of paleosols: Geological Society of America Bulletin, v. 105, p. 129-136.

McGookey, D.P., Haun, J., Hale, L., Goodell, H., McCubbin, D., Weimer, R., and Wulf, G., 1972, Cretaceous system: Geologic Atlas of the Rocky Mountain Region: Rocky Mountain Association of Geologists, p. 190-228.

Miall, A., 1996, The geology of fluvial deposits: Sedimentary Facies, Basin Analysis, and Petroleum Geology, .

Miall, A., 1978, Fluvial Sedimentology, vol. 5: Canadian Society of Petroleum Geologists Memoir, p. 1-859.

Miall, A.D., 1985, Architectural-element analysis: a new method of facies analysis applied to fluvial deposits: .

Miall, A.D., 1977, Lithofacies types and vertical profile models in braided river deposits: a summary: .

Mix, H.T., Mulch, A., Kent-Corson, M.L., and Chamberlain, C.P., 2011, Cenozoic migration of topography in the North American Cordillera: Geology, v. 39, p. 87-90.

Moody, J.A., Pizzuto, J.E., and Meade, R.H., 1999, Ontogeny of a flood plain: Geological Society of America Bulletin, v. 111, p. 291-303.

Nanson, G., and Croke, J., 1992, A genetic classification of floodplains: Geomorphology, v. 4, p. 459-486.

Nanson, G.C., 1986, Episodes of vertical accretion and catastrophic stripping: a model of disequilibrium flood-plain development: Geological Society of America Bulletin, v. 97, p. 1467-1475.

Norris, R.D., Jones, L.S., Corfield, R.M., and Cartlidge, J.E., 1996, Skiing in the Eocene Uinta Mountains? Isotopic evidence in the Green River Formation for snow melt and large mountains: Geology, v. 24, p. 403-406.

Peyton, S.L., Reiners, P.W., Carrapa, B., and DeCelles, P.G., 2012, Low-temperature thermochronology of the northern Rocky Mountains, western USA: American Journal of Science, v. 312, p. 145-212.

Pietras, J., Carroll, A., Singer, B., and Smith, M., 2003, 10 ky depositional cyclicity in the early Eocene: Stratigraphic and 40Ar/39Ar evidence from the lacustrine Green River Formation: Geology, v. 31, p. 593-596.

Quade, J., Garzione, C., and Eiler, J., 2007, Paleoelevation reconstruction using pedogenic carbonates: Reviews in Mineralogy and Geochemistry, v. 66, p. 53-87.

Quade, J., and Roe, L.J., 1999, The stable-isotope composition of early ground-water cements from sandstone in paleoecological reconstruction: Journal of Sedimentary Research, v. 69, .

Retallack, G.J., 1997, Colour guide to paleosols. John Wiley & Sons Ltd, .

Rhodes, M.K., Carroll, A.R., Pietras, J.T., Beard, B.L., and Johnson, C.M., 2002, Strontium isotope record of paleohydrology and continental weathering, Eocene Green River Formation, Wyoming: Geology, v. 30, p. 167-170.

Rigby, J.K., 1980, Swain Quarry of the Fort Union Formation, Middle Paleocene (Torrejonian), Carbon County, Wyoming, Geologic Setting and Mammalian Fauna: Evolutionary Monographs, University of Chicago, .

Roberts, J.A., Bennett, P.C., González, L.A., Macpherson, G., and Milliken, K.L., 2004, Microbial precipitation of dolomite in methanogenic groundwater: Geology, v. 32, p. 277-280.

Roehler, H.W., 1993, Eocene climates, depositional environments, and geography, greater Green River Basin, Wyoming, Utah, and Colorado: United States Geological Survey, Professional Paper, .

Roehler, H.W., 1992, Correlation, Composition, Areal Distribution, and Thickness of Eocene Stratigraphic Units, Greater Green River Basin, Wyoming, Utah, and Colorado.

Roehler, H.W., 1991, Revised stratigraphic nomenclature for the Wasatch and Green River formations of Eocene age, Wyoming, Utah, and Colorado: .

Roehler, H.W., 1965, Early Tertiary depositional environments in the Rock Springs uplift area: .

Roehler, H.W., and Martin, P., 1987, Geological Investigations of the Vermillion Creek Coal Bed in the Eocene Niland Tongue of the Wasatch Formation, Sweetwater County, Wyoming, .

Rowley, D.B., 2007, Stable isotope-based paleoaltimetry: Theory and validation: Reviews in Mineralogy and Geochemistry, v. 66, p. 23-52.

Rowley, D.B., and Garzione, C.N., 2007, Stable isotope-based paleoaltimetry: Annu.Rev.Earth Planet.Sci., v. 35, p. 463-508.

Rowley, D.B., Pierrehumbert, R.T., and Currie, B.S., 2001, A new approach to stable isotope-based paleoaltimetry: implications for paleoaltimetry and paleohypsometry of the High Himalaya since the Late Miocene: Earth and Planetary Science Letters, v. 188, p. 253-268.

Rust, B.R., 1972, Structure and process in a braided river: Sedimentology, v. 18, p. 221-245.

Sánchez-Román, M., Vasconcelos, C., Schmid, T., Dittrich, M., McKenzie, J.A., Zenobi, R., and Rivadeneyra, M.A., 2008, Aerobic microbial dolomite at the nanometer scale: Implications for the geologic record: Geology, v. 36, p. 879-882.

Sclater, J.G., and Christie, P., 1980, Continental stretching; an explanation of the post-Mid-Cretaceous subsidence of the central North Sea basin: Journal of Geophysical Research, v. 85, p. 3711-3739.

Sewall, J.O., and Sloan, L.C., 2006, Come a little bit closer: A high-resolution climate study of the early Paleogene Laramide foreland: Geology, v. 34, p. 81-84.

Shuster, M.W., 1987, Fluvial-sandstone architecture and thrust-induced subsidence, northern Green River Basin, Wyoming: .

Shuster, M.W., 1986, The origin and sedimentary evolution of the northern Green River Basin, western Wyoming: .

Shuster, M.W., and Steidtmann, J.R., 1988, Tectonic and sedimentary evolution of the northern Green River basin, western Wyoming: Geological Society of America Memoirs, v. 171, p. 515-530.

Singh, S., Parkash, B., Awasthi, A., and Kumar, S., 2014, Do stable isotopes in carbonate cement of Mio-Pleistocene Himalayan sediments record paleoecological and paleoclimatic changes? Palaeogeography, Palaeoclimatology, Palaeoecology, v. 399, p. 363-372.

Snell, K.E., Thrasher, B.L., Eiler, J.M., Koch, P.L., Sloan, L.C., and Tabor, N.J., 2013, Hot summers in the Bighorn Basin during the early Paleogene: Geology, v. 41, p. 55-58.

Solomon, S.T., and Walkden, G.M., 1985, The application of cathodoluminescence to interpreting the diagenesis of an ancient calcrete profile: Sedimentology, v. 32, p. 877-896.

Stearns, R.G., 1957, Cretaceous, Paleocene, and lower Eocene geologic history of the northern Mississippi embayment: Geological Society of America Bulletin, v. 68, p. 1077-1100.

Stevens, A.L., Balgord, E.A., and Carrapa, B., 2016, Revised exhumation history of the Wind River Range, WY, and implications for Laramide tectonics: Tectonics, v. 35, p. 1121-1136.

Talbot, M., 1990, A review of the palaeohydrological interpretation of carbon and oxygen isotopic ratios in primary lacustrine carbonates: Chemical Geology: Isotope Geoscience Section, v. 80, p. 261-279.

United States. Soil Conservation Service, 1975, Soil Taxonomy: A basic system of soil classification for making and interpreting soil surveys: US Department of Agriculture, Soil Conservation Service.

VanDeVelde, J.H., and Bowen, G.J., 2014, Isotope hydrology of early paleogene Lake Flagstaff, central Utah: Implications for Cordilleran evolution: American Journal of Science, v. 314, p. 1436-1461.

VanDeVelde, J.H., Bowen, G.J., Passey, B.H., and Bowen, B.B., 2013, Climatic and diagenetic signals in the stable isotope geochemistry of dolomitic paleosols spanning the Paleocene–Eocene boundary: Geochimica Et Cosmochimica Acta, v. 109, p. 254-267.

Warren, J., 2000, Dolomite: occurrence, evolution and economically important associations: Earth-Science Reviews, v. 52, p. 1-81.

Weimer, R.J., 1960, Upper cretaceous stratigraphy, rocky Mountain area: AAPG Bulletin, v. 44, p. 1-20.

Wilf, P., 2000, Late Paleocene–early Eocene climate changes in southwestern Wyoming: Paleobotanical analysis: Geological Society of America Bulletin, v. 112, p. 292-307.

Wing, S.L., Harrington, G.J., Smith, F.A., Bloch, J.I., Boyer, D.M., and Freeman, K.H., 2005, Transient floral change and rapid global warming at the Paleocene-Eocene boundary: Science (New York, N.Y.), v. 310, p. 993-996, doi: 310/5750/993 [pii].

Wolfe, J.A., Forest, C.E., and Molnar, P., 1998, Paleobotanical evidence of Eocene and Oligocene paleoaltitudes in midlatitude western North America: Geological Society of America Bulletin, v. 110, p. 664-678.

Wright, V.P., and Marriott, S.B., 1993, The sequence stratigraphy of fluvial depositional systems: the role of floodplain sediment storage: Sedimentary Geology, v. 86, p. 203-210.

Wright, V.P., and Tucker, M.E., 1991, Calcretes: Blackwell Scientific Publications.

Figures and tables

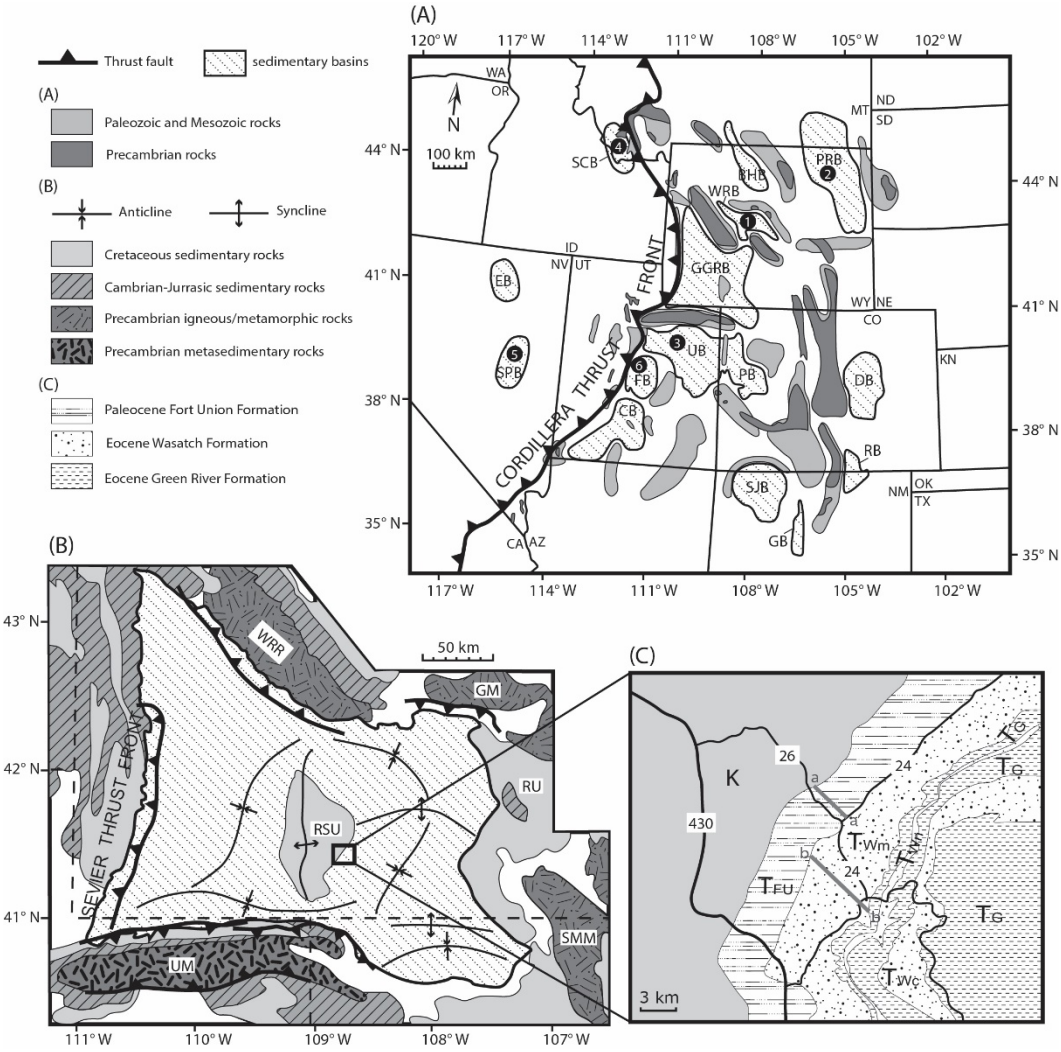

Figure 3-1 A: Major Paleogene structures in the central North American Cordillera. Modified after Davis et al. (2008); B: Location of the study area and major structural features in the Greater Green River Basin. Modified after Roehler (1992); C: Detailed geologic map of the field area (Geologic map courtesy of USGS). a-a': measured section of the Fort Union Formation (starts at 41. 42856ºN, 108. 80006ºW, elevation 2136 m, ends at 41. 40243ºN, 108. 76283ºW, elevation 2154 m); b-b': measured section of the main body of the Wasatch Formation (starts at 41.36864ºN, 108.80663ºW, elevation 2176 m, ends at 41.32883ºN, 108.73188ºW, elevation 2278 m). Nominations: K, Cretaceous; T_{FU}, Fort Union Formation; T_{Wm}, the main body of the Wasatch Formation; T_{Wn}, the

Niland Tongue of the Wasatch Formation; T_{Wc}, the Cathdrewl Tongue of the Wasatch Formation; T_G, Green River Formation; BHB, Bighorn Basin; CB, Claron Basin; DB, Denver Basin; EB, Elko Basin; FB, Flagstaff Basin (note the Axhandle Basin is in the northwestern part of the Flagstaff Basin); GB, Galisteo Basin; GGRB, Greater Green River Basin; PB, Piceance Creek Basin; PRB, Powder River Basin; RB, Raton Basin; SCB, Sage Creek Basin; SJB, San Juan Basin; SPB: Sheep Pass Basin; UB, Uinta Basin; WRB, Wind River Basin; GM: Granite Mountains; RSU: Rock Springs Uplift; RU: Rawlins Uplift; SM: Sierra Madre Mountains; UM: Uinta Mountains; WRR: Wind River Range. Black circles represent previous studies mentioned in our discussion, for examples: ① Fan et al. (2011); ②Fan and Dettman (2009); ③ Davis et al. (2008); ④ Chamberlain et al. (2012); ⑤ Lechler et al. (2013); ⑥ Chamberlain et al. (2012).

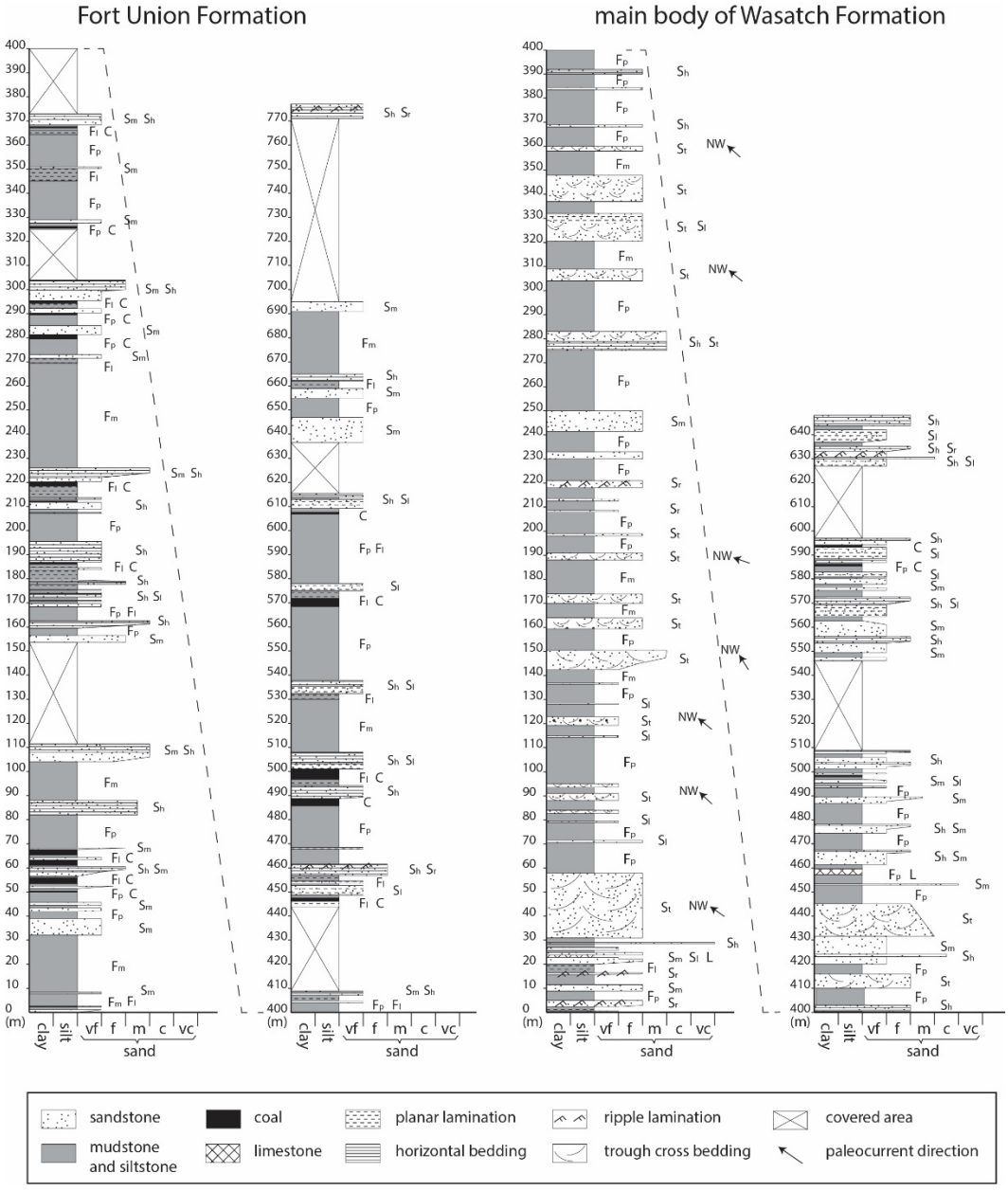

Figure 3-2 Measured stratigraphic sections of the Paleocene Fort Union Formation (A) and the lowermost Eocene Wasatch Formation (B). Section locations are shown in Figure 3-1.

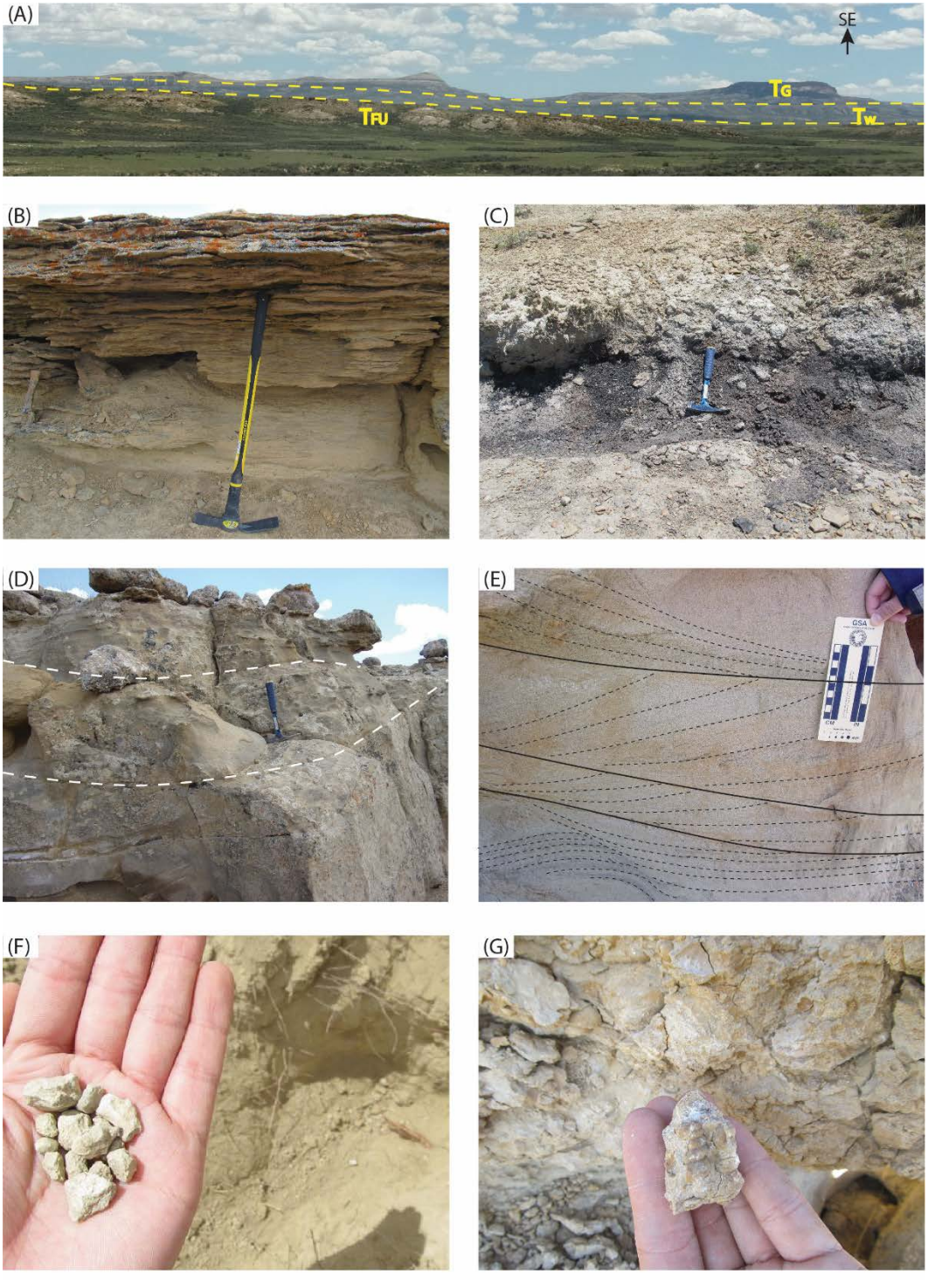
(A)
SE
TG
TFU
TW
(B)
(C)
(D)
(E)
(F)
(G)

Figure 3-3 Outcrop photographs of the measured strata. A: Overview of the field area showing the spatial relationship of formations (T_{FU}- Fort Union Formation, T_W- Wasatch Formation, T_G- Green River Formation), taken in the middle part of section a-a' on Rd 26 (Figure 3-1), facing to SE; B: Sandstone beds in the Fort Union Formation, showing that sedimentary structures change from massive bedding at the bottom to planar and ripple laminations at the top; C: Fine-grained floodplain deposits in the Fort Union Formation containing a coal bed; D: Thickly-bedded sandstone unit in the Wasatch Formation; E: River channel sandstone in the Wasatch Formation showing trough cross-beddings; F: Pedogenic carbonate nodules in the Wasatch Formation; G: A thin limestone lens containing fresh water snails in the upper part of the main body of Wasatch Formation.

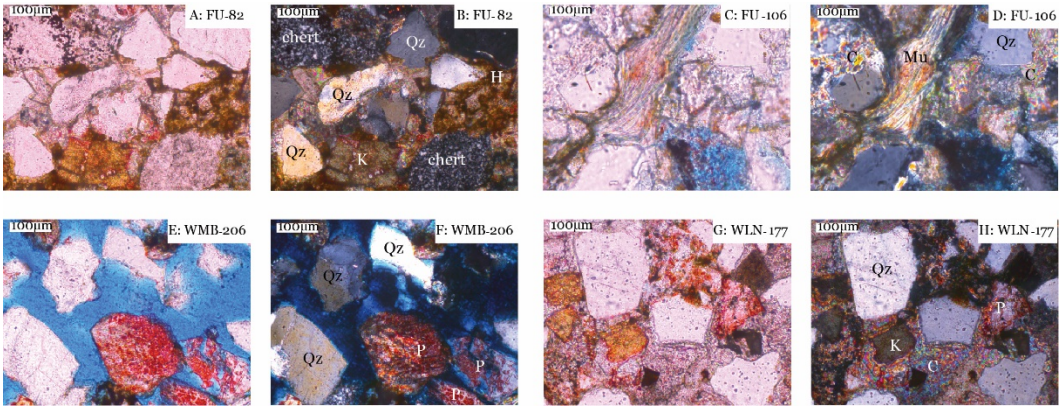

Figure 3-4 Photomicrographs of four sandstone samples under plane-polarized light and cross-polarized light. Scale bar is 100 μm. Note the relatively high abundance of chert grains in the Fort Union Formation (A-D), and high abundance of feldspar grains in the Wasatch Formation (E-H). A large muscovite grain is shown in C and D. The sandstones have large intergranular space that is filled by cement and matrix. The large volumes of pore space in E and F are likely resulted from dissolution of carbonate cement. Nominations: Qz: quartz, K: K-feldspar, P: plagioclase, C: carbonate cement, H: hematite cement, Mu: muscovite.

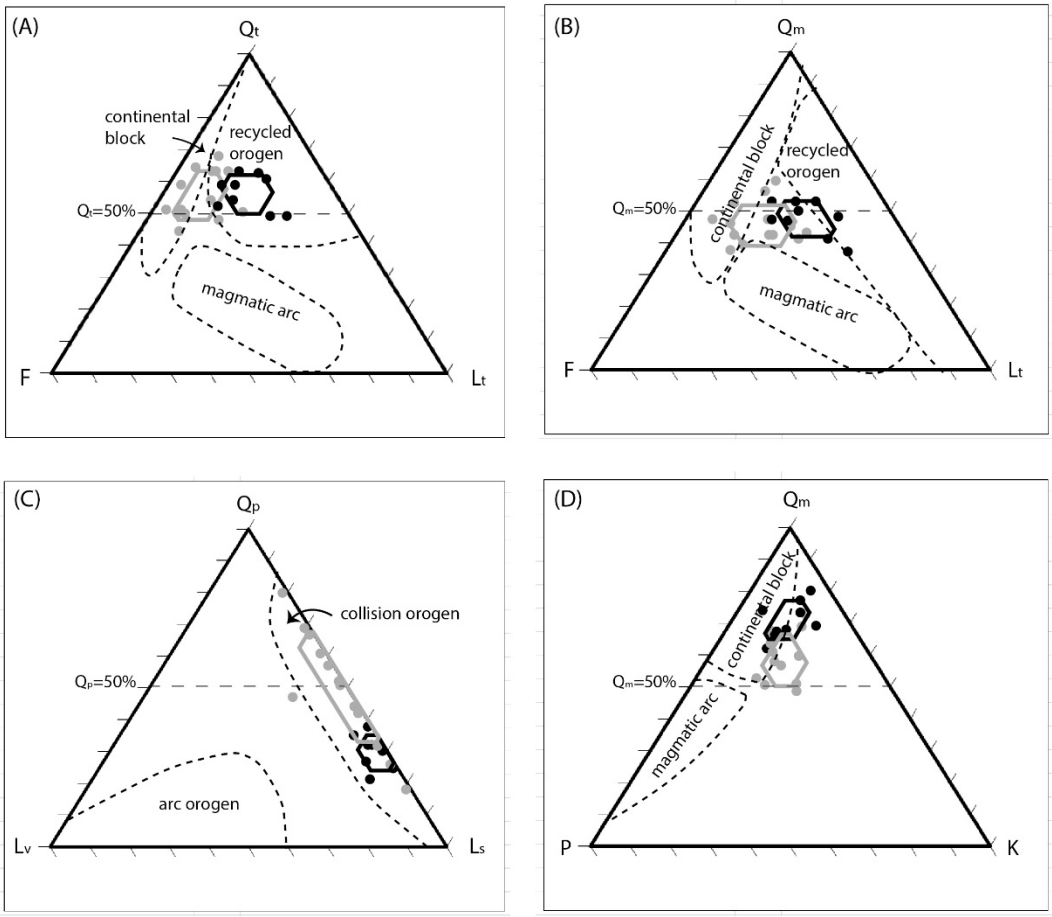

Figure 3-5 Ternary plots of the studied sandstone samples. Black dots represent the samples from the Fort Union Formation; grey dots represent the samples from the Wasatch Formation; polygons represent the mean and standard deviation (1σ) of all samples analyzed in each formation; regions outlined by dashed lines show estimated provenance data in different geologic setting based on Dickinson and Suczek (1979).

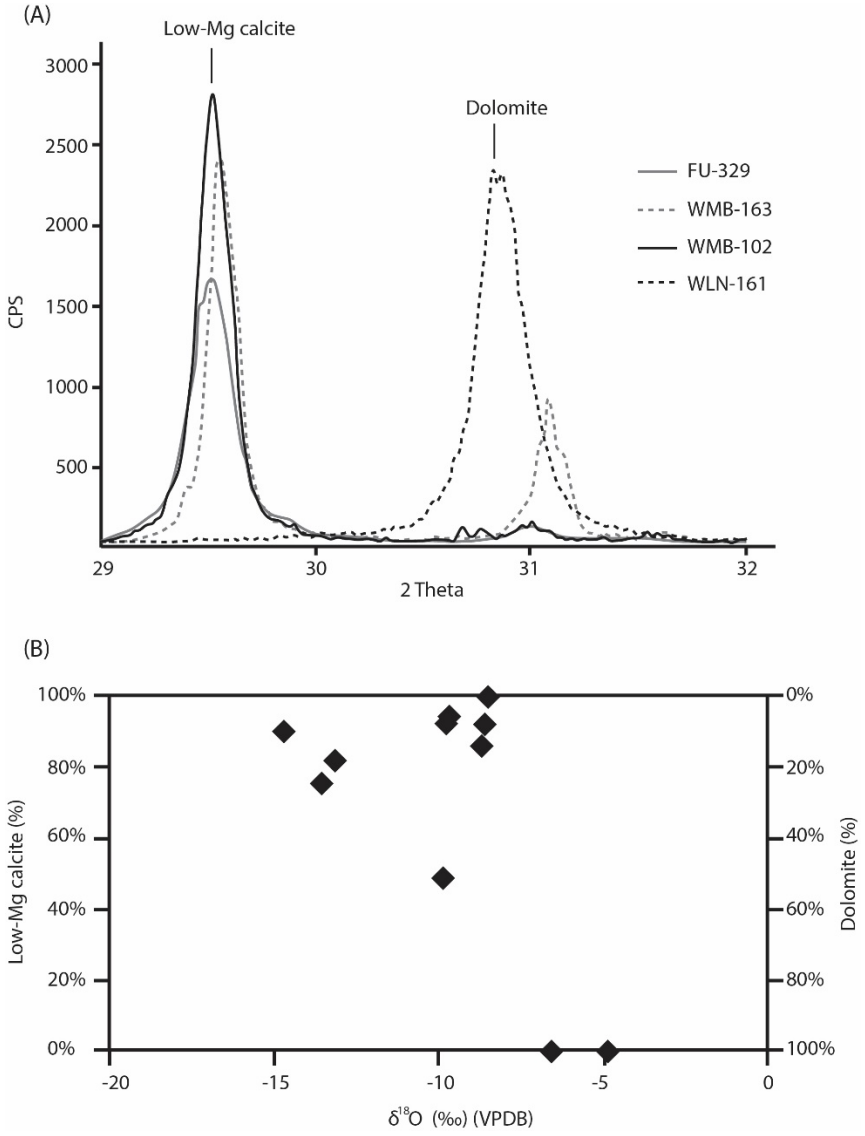

Figure 3-6 A: Graphs showing X-ray diffraction results of four studied samples. Most sandstone samples have carbonate cement dominated by low-magnesium calcite with a small amount of dolomite (for example, samples FU-329 and WMB-163). Sandstone samples from the upper 200 m of the main body of the Wasatch Formation has more dolomite cement (sample WLN-161 has pure dolomite). Pedogenic carbonate nodule samples contain predominantly low-magnesium calcite and a small amount of dolomite (for example, sample WMB-102). B: Correlation of carbonate mineralogy and $\delta^{18}O$ values showing that samples dominated by dolomite have high $\delta^{18}O$ values.

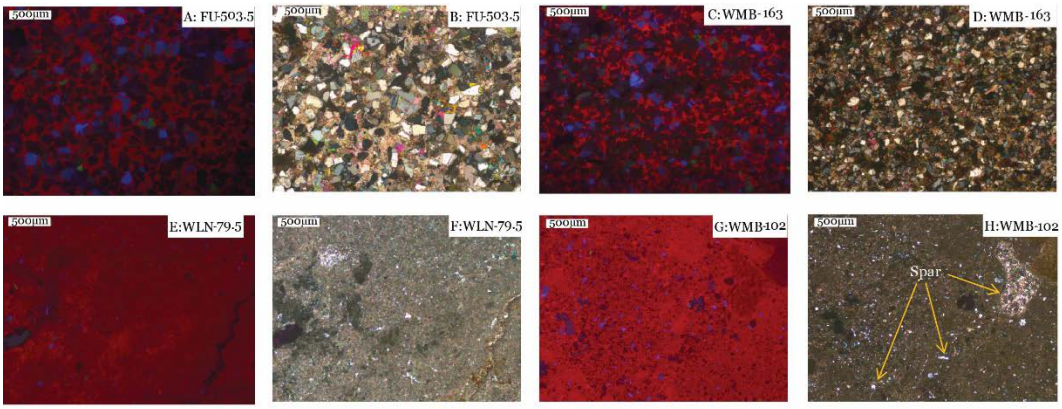

Figure 3-7 Photomicrographs of four studied carbonate samples under cathodoluminescence and cross-polarized light. Scale bars are 500 μm. A and C: Carbonate cements in two sandstone samples show micritic texture under cross-polarized light, and B and D: The intergranular micritic calcite of the same samples show red luminescence under cathodoluminescent light; E and G: Carbonates in two pedogenic nodules show micritic texture and scattered small spars under cross-polarized light, and F and H: Red luminescence and clotted fabric under cathodoluminescent light. Luminescence in clay-rich regions is brighter than luminescence in carbonate-rich regions. Feldspar displays blue luminescence; polycrystalline quartz displays green luminescence, and the minerals without luminescence are mostly quartz.

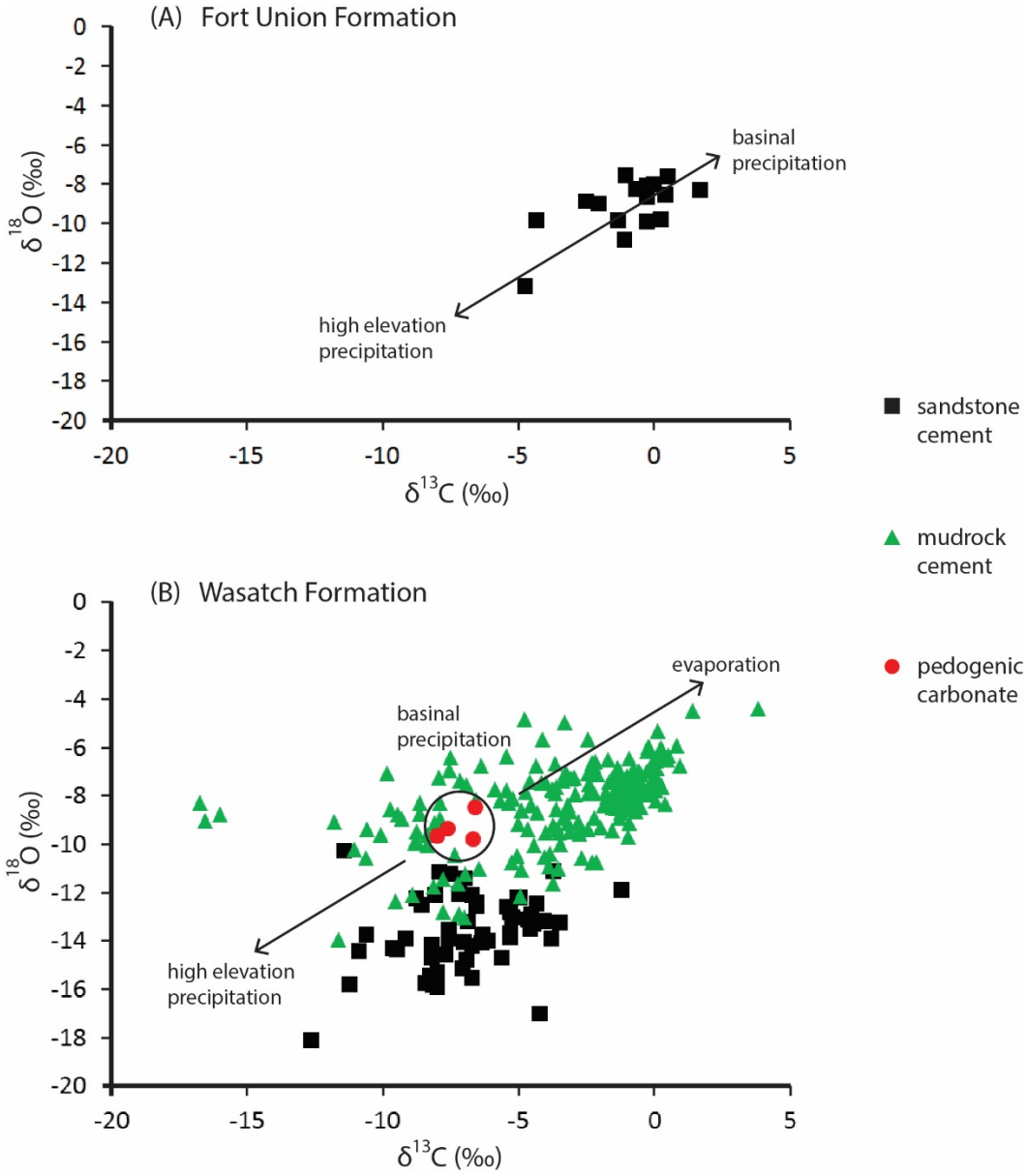

Figure 3-8 Results of stable isotope analysis of different types of carbonate. Note pedogenic carbonate and bulk mudstone samples only present in the Wasatch Formation.

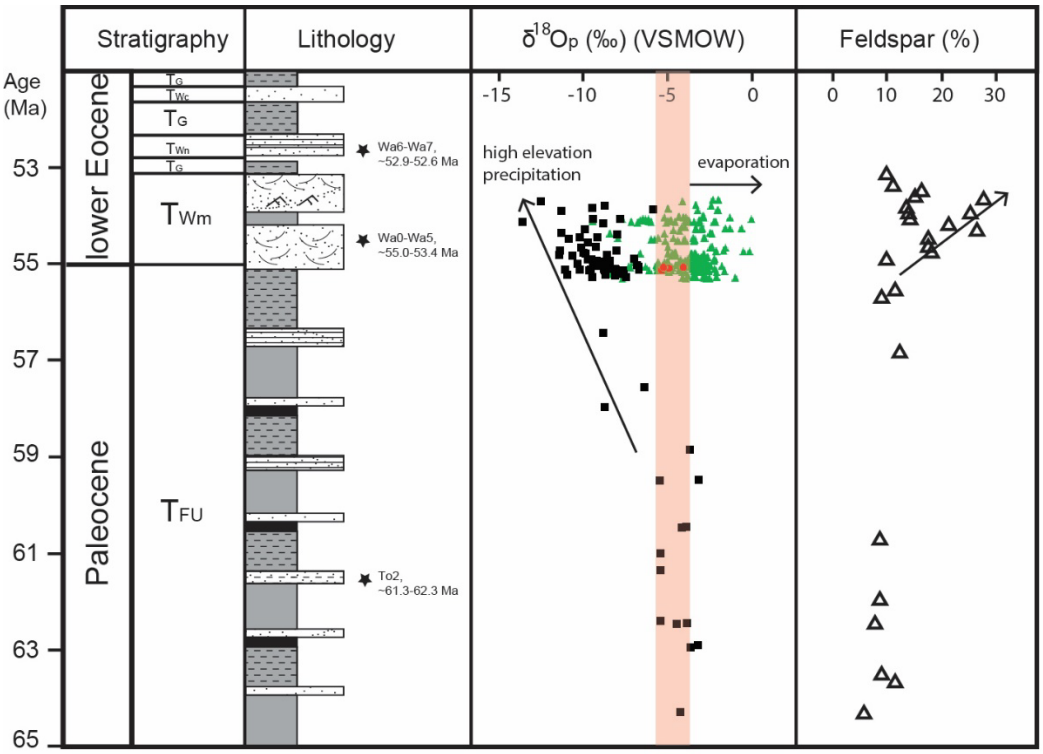

Figure 3-9 Temporal variations of calculated water $\delta^{18}O$ values using warm season carbonate precipitation temperature (35 °C) and abundance of feldspar grains in the Paleocene Fort Union Formation and lower Eocene Wasatch Formation. Stars represent stratigraphic levels of age constraints in the text.

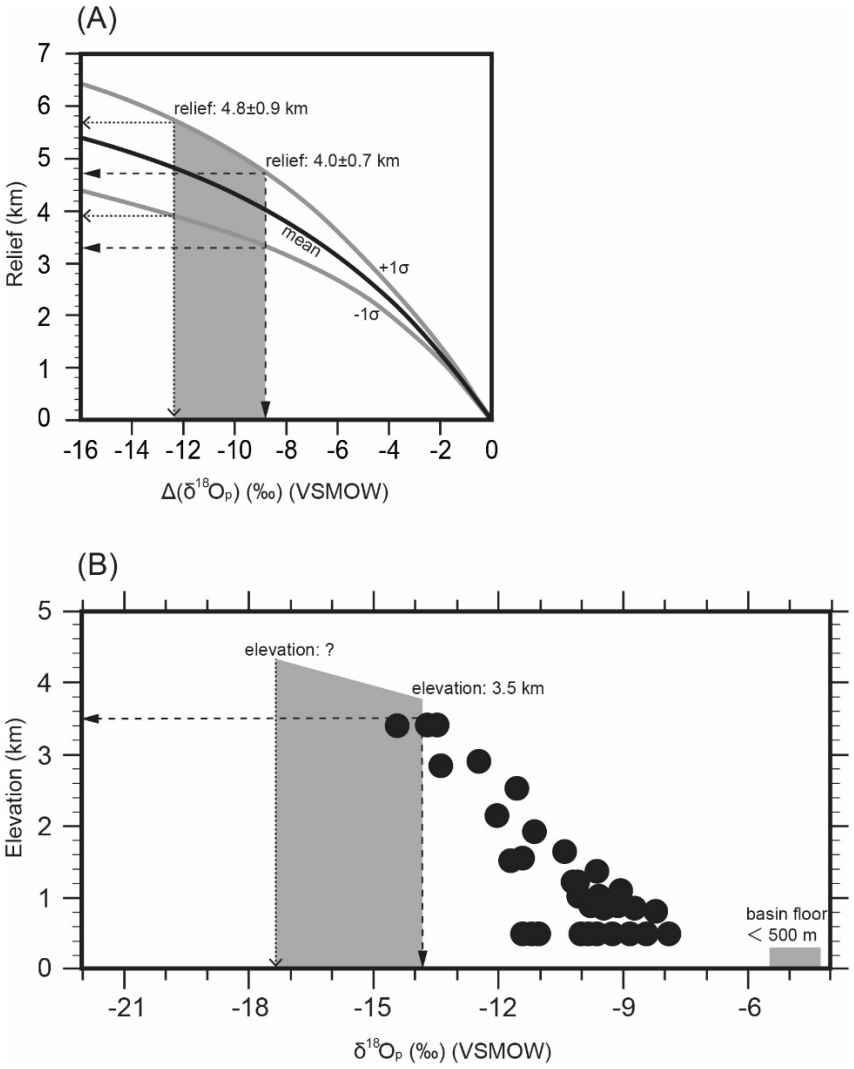

Figure 3-10 A: Paleorelief estimates based on the thermodynamic air-mass lifting Rayleigh condensation model by Rowley et al. (2007). B: Paleoelevation estimates based on the predicted Eocene precipitation $\delta^{18}O$ values at different elevations in the eastern flank of the Cordillera using isotope-enabled global climate model (GCM) (Feng et al., 2013), black dots represent GCM-simulated $\delta^{18}O_p$. Our mineral-derived $\delta^{18}O_p$ values suggest that during the earliest Eocene, the paleoelevation of the basin floor was less than 500 m, the paleoelevation of the Uinta Mountains was ~ 3.5 km based on warm season carbonate precipitation temperature (35 °C) ($\delta^{18}O_p$ = -13.8 ‰). Note that the GCM model does not have data for estimating the paleoelevation based on mean annual carbonate precipitation temperature (17 °C) ($\delta^{18}O_p$ = -17.4 ‰).

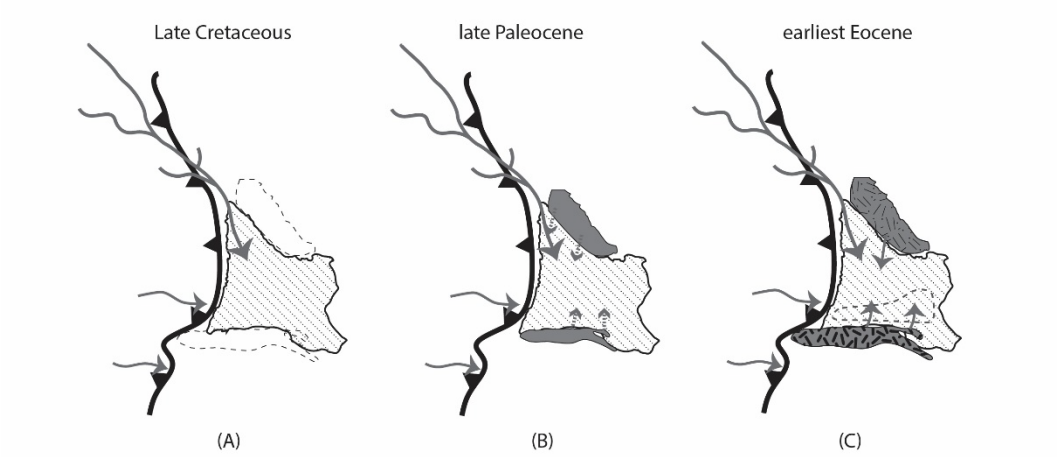

Figure 3-11 Inferred paleogeography evolution in the Greater Green River Basin. A: During the Late Cretaceous, the basin mainly had rivers draining east from the Cordillera hinterland (e.g., Hansen, 1965 and 1985; Steidtmann, 1969; Dorr Jr. et al., 1977; Stanley and Collinson, 1979; Moncure and Surdam, 1980; Cole, 1985; Sklenar and Anderson, 1985; Roehler, 1993); B: During the late Paleocene, the surface uplift of the Uinta Mountains and Wind River Range interfered the generally eastward-flowing river system by adding northward and southward rivers into the basin; C: During the earliest Eocene, the Wind River Range and the Uinta Mountains both gained high topography of ~3-4 km, braided rivers draining from these mountains dominated the drainage patterns in the basin (Surdam and Wolfbauer, 1975; Carroll et al., 2008; Davis et al., 2008; this study). Dashed grey circle represents the initial development of the Lake Gosiute during the early Eocene.

Table 3-1 Lithofacies and interpretations used in this study (Modified from Miall (1978) and DeCelles et al. (1991))

Facies code	Description	Interpretation
S_t	Fine- to medium-grained sandstone with trough cross-stratification	Migration of large 3D ripples (dunes) under moderately powerful unidirectional flows in large channels; lower flow regime
S_h	Fine- to medium-grained sandstone, horizontally bedded; usually well cemented	Upper plane bed conditions, or flash floods under unidirectional flows, either strong or very shallow
S_r	Very fine- to fine-grained sandstone with ripple lamination	Migration of small 2D and 3D ripples under weak unidirectional flows in shallow channels; lower flow regime
S_l	Very fine- to fine-grained sandstone with planar lamination	Planar bed flow; lower and upper flow regime
S_m	Massive very fine- to fine-grained sandstone	Deposition from small gravity flow
F_l	Shale (mudstone with planar lamination)	Deposition from suspension in overbank area or waning flood deposits
F_m	Massive mudstone, sometimes bioturbated	Deposition from suspension in ponds and overbank area or drape deposits
F_p	Massive mudstone with mottled colors, sometimes with carbonate concentration veins or nodules	Paleosol
C	Coal or carbonaceous mudstone	Swamp or stable floodplain deposits
L	Massive limestone	Lacustrine or groundwater deposits

Table 3-2 Modal petrographic point-counting parameters

Symbol	Description
Q_m	Monocrystalline quartz
Q_p	Polycrystalline quartz
Q_t	Total quartzose grains ($Q_m + Q_p + E$)
K	Potassium feldspar
P	Plagioclase feldspar
F	Total feldspar grains (K+ P)
E	Chert
SS	Sandstone
S	Siltstone
L	Total nonquartzose lithic grains ($L_v + L_s + L_c$)
L_t	Total lithic grains ($L_v + L_s + L_c + Q_p$)
L_s	Total sedimentary lithic grains ($SS + S + E + L_c$)
L_v	Volcanic lithic grains
L_c	Carbonate lithic grains
C	Carbonate cement
H	Hematite cement
X	Matrix
O	Porosity
Others	muscovite, biotite, glauconite, chlorite

Table 3-3 Modal petrographic point-counting data

Sample	Q_m (%)	Q_p (%)	E (%)	K (%)	P (%)	SS (%)	S (%)	L_c (%)	L_v (%)	X (%)	C (%)	H (%)	O (%)	Others (%)
FU-52.5	13.5	4.3	2.0	4.3	1.8	2.2	6.5	1.8	0.0	25.8	23.5	13.9	0.4	0.0
FU-104.5	28.1	5.3	1.1	6.0	6.9	3.8	3.3	0.7	0.9	6.5	30.5	5.1	1.3	0.4
FU-106	22.8	2.5	0.9	5.1	3.4	2.5	2.0	0.4	0.0	12.5	24.2	14.3	5.1	4.3
FU-153.5	13.6	2.7	0.7	2.7	4.0	2.7	4.4	1.3	1.1	20.0	28.0	13.3	5.3	0.2
FU-178	31.4	7.4	8.3	6.0	1.9	1.7	4.0	0.5	1.0	4.3	5.7	19.3	7.1	1.4
FU-225.5	26.0	4.8	3.3	4.8	2.9	2.4	3.3	0.7	0.5	3.3	24.8	19.5	3.3	0.5
FU-507.5	23.3	2.9	2.6	5.0	9.3	1.4	2.6	1.4	0.0	11.9	31.2	4.0	0.2	4.0
FU-659	25.2	4.5	3.8	1.9	6.9	0.7	2.9	0.0	0.0	5.5	22.1	22.6	1.0	2.9
FU-665	23.6	3.6	1.9	4.3	7.6	1.9	4.8	0.0	1.0	2.9	30.0	12.4	3.8	2.4
WMB-5	14.0	2.1	1.2	4.3	6.0	1.2	2.4	1.2	0.0	15.0	27.4	18.3	5.5	1.4
WMB-29	19.3	3.6	1.4	6.7	11.7	0.7	1.2	0.0	0.0	4.5	25.7	5.2	14.8	5.2
WMB-148	22.9	6.2	1.2	7.9	9.5	1.2	1.4	1.2	1.9	11.2	19.8	7.9	6.7	1.2
WMB-164.5	24.5	7.1	2.1	13.3	12.4	0.0	2.4	0.0	0.0	7.6	0.7	3.1	25.2	1.4
WMB-174	21.9	1.9	0.5	11.0	10.0	0.0	1.0	0.0	0.0	8.1	33.8	8.1	1.9	1.9
WMB-199	23.3	2.6	1.7	5.0	8.3	3.3	6.0	1.0	0.0	3.8	3.3	3.3	34.0	4.3
WMB-206	29.3	3.8	0.2	7.4	5.7	1.7	2.9	0.0	0.0	10.2	1.0	3.1	32.9	1.9
WLN-88.5	28.1	2.5	4.3	7.6	17.1	0.9	0.0	0.0	0.0	3.4	27.2	3.4	2.5	3.1
WLN-3	19.5	10.7	1.9	6.9	6.0	0.5	1.9	0.5	0.0	2.9	26.7	2.9	18.3	1.4
WLN-47	21.9	4.3	2.9	15.2	11.7	1.4	0.7	1.0	0.0	2.1	24.3	2.1	11.0	1.4
WLN-69	22.6	2.9	1.2	8.3	6.7	0.0	0.2	0.0	0.0	5.5	34.3	6.4	10.2	1.7
WLN-136	25.0	9.3	0.0	6.0	10.0	0.0	0.0	2.4	0.0	6.9	30.7	4.3	3.1	2.4

Sample	Q_m (%)	Q_p (%)	E (%)	K (%)	P (%)	SS (%)	S (%)	L_c (%)	L_v (%)	X (%)	C (%)	H (%)	O (%)	Others (%)
WLN-177	31.7	4.5	2.9	7.6	4.3	0.0	0.0	1.4	0.0	3.6	37.6	1.9	0.0	4.5
WLN-227	22.6	10.5	3.8	3.6	6.9	1.2	1.7	0.0	0.0	4.3	36.2	3.6	1.9	3.8

Table 3-4 Isotope values of different types of carbonate samples and calculated water isotope values

Sample ID	meter level (m)	$\delta^{18}O$ (‰)	$\delta^{13}C$ (‰)	water $\delta^{18}O$ (‰) (T=17 °C)	water $\delta^{18}O$ (‰) (T=35 °C)
sandstone cement					
FU-60.5	60.5	-8.7	-0.2	-8.0	-4.3
FU-168.5	168.5	-8.0	0.0	-7.3	-3.7
FU-173.0	173.0	-7.6	0.5	-6.9	-3.3
FU-209	209.0	-8.9	-2.5	-8.1	-4.5
FU-210.5	210.5	-8.2	-0.6	-7.5	-3.9
FU-213.5	213.5	-9.9	-4.3	-9.1	-5.5
FU-299.5	299.5	-9.9	-1.3	-9.1	-5.5
FU-329	329.0	-9.8	0.3	-9.1	-5.5
FU-371.5	371.5	-8.6	0.4	-7.8	-4.2
FU-373	373.0	-8.3	1.7	-7.6	-4.0
FU-451	451.0	-9.9	-0.2	-9.2	-5.6
FU-452.5	452.5	-7.6	-1.0	-6.8	-3.2
FU-503.0	503.0	-8.1	-0.2	-7.4	-3.8
FU-576	576.0	-13.2	-4.7	-12.5	-8.9
FU-609.5	609.5	-10.8	-1.0	-10.1	-6.5
WMB-15.5	795.5	-11.9	-1.2	-11.2	-7.6
WMB-16.5	796.5	-13.9	-3.7	-13.2	-9.6
WMB-25	805.0	-12.6	-6.5	-11.9	-8.3
WMB-37-cr	817.0	-15.5	-8.3	-14.8	-11.2
WMB-37	817.0	-13.2	-4.6	-12.4	-8.8
WMB-42	822.0	-12.1	-8.0	-11.4	-7.8
WMB-43	823.0	-12.1	-7.2	-11.4	-7.8
WMB-60	840.0	-12.2	-5.0	-11.5	-7.9
WMB-70	850.0	-12.2	-4.9	-11.5	-7.9
WMB-71	851.0	-12.1	-6.7	-11.4	-7.8
WMB-76	856.0	-13.2	-4.0	-12.5	-8.9
WMB-79	859.0	-15.5	-6.7	-14.8	-11.2
Wmb-80	860.0	-12.5	-8.5	-11.8	-8.2

Sample ID	meter level (m)	$\delta^{18}O$ (‰)	$\delta^{13}C$ (‰)	water $\delta^{18}O$ (‰) (T=17 °C)	water $\delta^{18}O$ (‰) (T=35 °C)
sandstone cement					
WMB-80.5	860.5	-11.2	-7.9	-10.4	-6.8
WMB-89.5	869.5	-12.6	-5.4	-11.9	-8.3
WMB-101.5	881.5	-11.1	-3.7	-10.4	-6.8
WMB-113	893.0	-13.9	-5.3	-13.2	-9.6
WMB-113.5	893.5	-13.5	-4.5	-12.8	-9.2
WMB-122	902.0	-14.8	-6.9	-14.1	-10.5
WMB-151.0	931.0	-13.3	-3.4	-12.5	-8.9
WMB-153	933.0	-13.7	-5.3	-13.0	-9.4
WMB-165	945.0	-14.2	-6.7	-13.5	-9.9
WMB-166	946.0	-14.0	-6.1	-13.3	-9.7
WMB-173.5	953.5	-11.4	-7.0	-10.7	-7.1
WMB-195.5	975.5	-15.2	-7.0	-14.4	-10.8
WMB-202	982.0	-16.0	-7.9	-15.2	-11.7
WMB2-10	850.0	-14.1	-6.3	-13.4	-9.8
WMB2-18	858.0	-14.1	-7.0	-13.3	-9.7
WMB2-18-cr	858.0	-14.7	-5.6	-14.0	-10.4
WMB2-28	868.0	-12.9	-4.5	-12.2	-8.6
WMB2-28-cr	868.0	-13.2	-6.8	-12.5	-8.9
WMB2-59.5	899.5	-13.7	-6.3	-13.0	-9.4
WMB2-60.7	900.7	-11.3	-7.5	-10.6	-7.0
WMB2-98.5	938.5	-12.9	-5.3	-12.1	-8.5
WMB2-141	981.0	-13.1	-5.2	-12.4	-8.8
WMB2-159	999.0	-14.3	-9.6	-13.6	-10.0
WMB2-161.8	1001.8	-14.5	-10.9	-13.7	-10.2
WMB2-178.5	1018.5	-15.9	-8.1	-15.2	-11.6
WMB2-182.3	1022.3	-12.5	-4.3	-11.7	-8.2
WMB2-202	1042.0	-14.6	-7.6	-13.9	-10.3
WMB2-212	1052.0	-13.7	-10.6	-13.0	-9.4
WMB2-248	1088.0	-14.2	-8.1	-13.5	-9.9
WMB2-278	1118.0	-15.3	-8.0	-14.6	-11.0
WMB2-290.2	1130.2	-13.6	-7.5	-12.9	-9.3
Wmb2-292	1132.0	-14.7	-8.1	-14.0	-10.4
WMB2-318	1158.0	-12.4	-6.5	-11.7	-8.1

Sample ID	meter level (m)	$\delta^{18}O$ (‰)	$\delta^{13}C$ (‰)	water $\delta^{18}O$ (‰) (T=17 °C)	water $\delta^{18}O$ (‰) (T=35 °C)
sandstone cement					
WMB2-329	1169.0	-15.8	-8.4	-15.0	-11.5
WMB2-361	1201.0	-14.4	-9.5	-13.7	-10.1
WLN-20.5	1250.5	-13.3	-4.4	-12.6	-9.0
WLN-33.0	1263.0	-18.1	-12.6	-17.4	-13.8
WLN-55.2	1285.2	-13.9	-7.5	-13.2	-9.6
WLN-56	1286.0	-12.3	-8.8	-11.5	-7.9
WLN-127	1357.0	-15.8	-11.2	-15.1	-11.5
WLN-136.5	1366.5	-10.3	-11.4	-9.6	-6.0
WLN-150	1380.0	-13.9	-9.1	-13.2	-9.6
WLN-168.8	1398.8	-13.2	-4.1	-12.5	-8.9
WLN-207.0	1437.0	-17.0	-4.2	-16.3	-12.7
mudstone cement					
WMB-4.0	784.0	-12.1	-4.9	-11.4	-7.8
WMB-6.0	786.0	-6.9	-7.5	-6.2	-2.6
WMB-6.5	786.5	-7.0	-9.8	-6.3	-2.7
WMB-7.0	787.0	-8.3	-8.6	-7.6	-3.9
WMB-8.0	788.0	-5.3	0.1	-4.6	-1.0
WMB-12.0	792.0	-8.5	-9.7	-7.8	-4.2
WMB-14.5	794.5	-6.9	-0.7	-6.2	-2.6
WMB-15.0	795.0	-7.2	0.0	-6.5	-2.9
WMB-17.0	797.0	-7.7	-0.1	-7.0	-3.4
WMB-17.5	797.5	-7.9	-2.2	-7.2	-3.5
WMB-18.5	798.5	-6.5	0.2	-5.7	-2.1
WMB-19.5	799.5	-7.3	-2.9	-6.5	-2.9
WMB-25.5	805.5	-8.2	-1.2	-7.4	-3.8
WMB-44.0	824.0	-12.8	-7.8	-12.1	-8.5
WMB-54.5	834.5	-9.3	-1.9	-8.6	-5.0
WMB-55.5	835.5	-8.5	-1.1	-7.8	-4.2
WMB-56.5	836.5	-6.5	-0.9	-5.7	-2.1
WMB-57.5	837.5	-7.4	-0.5	-6.6	-3.0
WMB-58.0	838.0	-7.3	0.0	-6.6	-3.0

Sample ID	meter level (m)	$\delta^{18}O$ (‰)	$\delta^{13}C$ (‰)	water $\delta^{18}O$ (‰) (T=17 °C)	water $\delta^{18}O$ (‰) (T=35 °C)
mudstone cement					
WMB-58.5	838.5	-7.6	0.3	-6.9	-3.3
WMB-61.5	841.5	-6.0	-0.2	-5.3	-1.6
WMB-62.5	842.5	-7.8	-0.8	-7.1	-3.5
WMB-66.5	846.5	-7.0	-0.2	-6.2	-2.6
WMB-67.0	847.0	-7.5	0.2	-6.8	-3.2
WMB-67.5	847.5	-7.3	0.2	-6.6	-3.0
WMB-68.0	848.0	-8.3	0.4	-7.6	-4.0
Wmb-70.3	850.3	-8.7	-8.6	-8.0	-4.4
WMB-71.5	851.5	-9.4	-3.1	-8.7	-5.1
WMB-72.0	852.0	-7.1	-2.4	-6.4	-2.7
WMB-72.5	852.5	-9.2	-5.0	-8.4	-4.8
WMB-73.0	853.0	-10.0	-3.4	-9.3	-5.7
WMB-73.5	853.5	-10.5	-4.0	-9.8	-6.2
WMB-79.5	859.5	-7.0	-0.5	-6.2	-2.6
WMB-82.5	862.5	-8.6	-0.7	-7.9	-4.3
WMB-88.0	868.0	-7.4	-4.6	-6.7	-3.1
WMB-88.8	868.8	-7.0	-3.2	-6.3	-2.7
WMB-90.5	870.5	-7.4	-4.2	-6.7	-3.1
WMB-91.5	871.5	-7.9	-2.9	-7.2	-3.6
WMB-92.0	872.0	-9.1	-3.2	-8.4	-4.8
WMB-92.5	872.5	-7.7	-5.8	-7.0	-3.4
WMB-93.0	873.0	-7.5	-4.0	-6.7	-3.1
WMB-95.5	875.5	-7.6	-0.7	-6.9	-3.3
WMB-102.5	882.5	-10.0	-8.3	-9.3	-5.7
WMB-103.5	883.5	-11.8	-8.1	-11.0	-7.4
WMB-105.5	885.5	-11.0	-6.4	-10.3	-6.7
WMB-107.5	887.5	-6.1	-0.3	-5.4	-1.8
WMB-108.5	888.5	-7.9	-1.3	-7.2	-3.6
WMB-109.0	889.0	-8.3	-0.6	-7.5	-3.9
WMB-109.5	889.5	-6.8	-1.4	-6.1	-2.5
WMB-110.0	890.0	-8.0	-1.7	-7.3	-3.7
WMB-110.5	890.5	-7.9	-0.7	-7.1	-3.5
WMB-120.0	900.0	-7.0	-2.2	-6.2	-2.6

Sample ID	meter level (m)	$\delta^{18}O$ (‰)	$\delta^{13}C$ (‰)	water $\delta^{18}O$ (‰) (T=17 °C)	water $\delta^{18}O$ (‰) (T=35 °C)
mudstone cement					
WMB-120.5	900.5	-7.3	-3.3	-6.6	-2.9
WMB-124.5	904.5	-8.5	-1.5	-7.7	-4.1
WMB-127.0	907.0	-7.8	-0.3	-7.0	-3.4
WMB-127.5	907.5	-7.1	-0.5	-6.4	-2.8
WMB-130.5	910.5	-9.4	-1.5	-8.7	-5.1
WMB-131.0	911.0	-8.5	-1.0	-7.8	-4.2
WMB-131.5	911.5	-7.4	-0.6	-6.6	-3.0
WMB-132.0	912.0	-8.1	-1.4	-7.4	-3.8
WMB-137.3	917.3	-10.0	-8.8	-9.2	-5.6
WMB-137.8	917.8	-9.5	-8.7	-8.7	-5.1
WMB-138.3	918.3	-11.4	-7.8	-10.7	-7.1
WMB-138.8	918.8	-9.6	-8.4	-8.9	-5.3
WMB-141.3	921.3	-8.2	-1.0	-7.5	-3.9
WMB-142.3	922.3	-7.6	-0.4	-6.9	-3.3
WMB-144.8	924.8	-8.2	-0.8	-7.4	-3.8
WMB-152.0	932.0	-8.1	-1.2	-7.3	-3.7
WMB-152.5	932.5	-7.7	-1.2	-7.0	-3.4
WMB-154.5	934.5	-8.4	-1.9	-7.6	-4.0
WMB-155.0	935.0	-7.5	-0.8	-6.7	-3.1
WMB-155.5	935.5	-7.5	-0.7	-6.8	-3.1
WMB-156.0	936.0	-7.4	-0.6	-6.6	-3.0
WMB-157.5	937.5	-6.6	-0.1	-5.9	-2.3
WMB-160.0	940.0	-7.8	-0.5	-7.0	-3.4
WMB-160.5	940.5	-8.2	0.1	-7.5	-3.9
WMB-161.0	941.0	-7.3	-1.3	-6.5	-2.9
WMB-161.5	941.5	-6.6	-2.3	-5.9	-2.3
WMB-162.0	942.0	-7.5	-0.5	-6.7	-3.1
WMB-171.0	951.0	-6.6	-2.2	-5.8	-2.2
WMB-171.5	951.5	-7.4	-1.7	-6.7	-3.1
WMB-183.5	963.5	-7.5	-6.9	-6.8	-3.2
WMB-184.5	964.5	-7.0	-1.3	-6.3	-2.7
WMB-192.5	972.5	-9.1	-2.8	-8.4	-4.8
WMB-193.0	973.0	-7.6	-3.6	-6.9	-3.3

Sample ID	meter level (m)	$\delta^{18}O$ (‰)	$\delta^{13}C$ (‰)	water $\delta^{18}O$ (‰) (T=17 °C)	water $\delta^{18}O$ (‰) (T=35 °C)
mudstone cement					
WMB-194.0	974.0	-8.9	-3.3	-8.2	-4.6
WMB-196.8	976.8	-9.1	-8.1	-8.4	-4.8
WMB2-28.8	868.8	-7.4	-0.5	-6.6	-3.0
WMB2-29.5	869.5	-6.6	0.1	-5.8	-2.2
WMB2-30.3	870.3	-7.2	0.0	-6.5	-2.9
WMB2-31.0	871.0	-7.9	-0.4	-7.2	-3.6
WMB2-31.8	871.8	-7.5	0.1	-6.8	-3.2
WMB2-32.5	872.5	-7.8	-0.5	-7.1	-3.5
WMB2-34.0	874.0	-7.8	0.1	-7.1	-3.4
WMB2-36.3	876.3	-11.6	-3.7	-10.9	-7.3
WMB2-40.0	880.0	-8.1	-1.3	-7.3	-3.7
Wmb2-46.0	886.0	-10.7	-2.3	-10.0	-6.4
Wmb2-49.0	889.0	-9.7	-1.0	-9.0	-5.4
WMB2-54.8	894.8	-7.8	-1.0	-7.1	-3.4
WMB2-56.3	896.3	-8.3	-7.9	-7.5	-3.9
WMB2-57.3	897.3	-10.1	-4.4	-9.3	-5.7
WMB2-57.7	897.7	-8.9	-2.2	-8.2	-4.6
WMB2-61.5	901.5	-8.6	-4.9	-7.9	-4.3
WMB2-66.5	906.5	-13.0	-7.0	-12.3	-8.7
WMB2-82.3	922.3	-8.4	-3.2	-7.6	-4.0
WMB2-83.0	923.0	-7.9	-2.4	-7.2	-3.5
WMB2-85.8	925.8	-9.4	-3.6	-8.7	-5.1
WMB2-88.0	928.0	-7.5	-1.2	-6.7	-3.1
WMB2-88.8	928.8	-8.7	-4.3	-7.9	-4.3
WMB2-97.5	937.5	-7.5	-2.4	-6.8	-3.1
WMB2-99.0	939.0	-7.1	-2.1	-6.4	-2.8
WMB2-99.7	939.7	-7.3	-1.3	-6.5	-2.9
WMB2-100.3	940.3	-7.4	-1.2	-6.7	-3.1
WMB2-105.7	945.7	-8.6	-3.1	-7.9	-4.3
WMB2-124.2	964.2	-7.4	-3.3	-6.7	-3.0
WMB2-125.0	965.0	-7.9	-3.6	-7.2	-3.6
WMB2-148.5	988.5	-7.2	-1.0	-6.5	-2.9
WMB2-153.0	993.0	-7.9	-0.3	-7.2	-3.6

Sample ID	meter level (m)	$\delta^{18}O$ (‰)	$\delta^{13}C$ (‰)	water $\delta^{18}O$ (‰) (T=17 °C)	water $\delta^{18}O$ (‰) (T=35 °C)
mudstone cement					
WMB2-153.7	993.7	-7.8	-5.4	-7.0	-3.4
WMB2-154.5	994.5	-9.1	-0.9	-8.4	-4.8
WMB2-155.2	995.2	-9.4	-2.4	-8.7	-5.1
WMB2-156.0	996.0	-8.9	-1.3	-8.2	-4.6
WMB2-156.7	996.7	-11.0	-3.5	-10.3	-6.7
WMB2-162.5	1002.5	-9.0	-9.3	-8.2	-4.6
WMB2-171.2	1011.2	-6.5	0.4	-5.7	-2.1
WMB2-172.0	1012.0	-4.5	1.4	-3.8	-0.1
WMB2-172.8	1012.8	-6.5	0.5	-5.8	-2.2
WMB2-173.5	1013.5	-4.8	-4.8	-4.1	-0.5
WMB2-175.8	1015.8	-6.0	0.2	-5.3	-1.7
WMB2-204.5	1044.5	-6.8	0.0	-6.1	-2.5
WMB2-205.3	1045.3	-5.9	0.9	-5.2	-1.6
WMB2-208.2	1048.2	-9.4	-2.7	-8.6	-5.0
WMB2-209.0	1049.0	-6.7	-6.4	-6.0	-2.4
WMB2-262.0	1102.0	-8.8	-9.5	-8.1	-4.5
WMB2-262.7	1102.7	-9.5	-4.0	-8.8	-5.2
WMB2-263.5	1103.5	-8.3	-1.1	-7.6	-4.0
WMB2-265.8	1105.8	-7.8	-0.7	-7.1	-3.5
WMB2-268.0	1108.0	-7.8	-3.7	-7.1	-3.4
WMB2-269.5	1109.5	-10.2	-11.0	-9.5	-5.9
WMB2-271.0	1111.0	-8.4	-1.2	-7.7	-4.1
WMB2-271.7	1111.7	-8.4	-1.4	-7.6	-4.0
WMB2-274.0	1114.0	-10.4	-3.8	-9.7	-6.1
WMB2-286.5	1126.5	-10.0	-8.7	-9.2	-5.6
WMB2-286.9	1126.9	-12.4	-9.5	-11.6	-8.1
WMB2-287.3	1127.3	-9.1	-11.8	-8.3	-4.7
WMB2-288.3	1128.3	-7.8	-1.8	-7.1	-3.5
WMB2-288.7	1128.7	-7.2	-1.0	-6.5	-2.9
WMB2-289.1	1129.1	-7.2	-0.9	-6.4	-2.8
WMB2-325.0	1165.0	-6.8	-4.3	-6.0	-2.4
WMB2-325.5	1165.5	-12.9	-7.2	-12.2	-8.6
WMB2-326.0	1166.0	-9.6	-10.1	-8.9	-5.3

Sample ID	meter level (m)	$\delta^{18}O$ (‰)	$\delta^{13}C$ (‰)	water $\delta^{18}O$ (‰) (T=17 °C)	water $\delta^{18}O$ (‰) (T=35 °C)
mudstone cement					
WMB2-327.5	1167.5	-6.9	0.1	-6.1	-2.5
WMB2-350.0	1190.0	-8.7	-1.2	-7.9	-4.3
WMB2-352.0	1192.0	-9.1	-16.5	-8.3	-4.7
WMB2-358.0	1198.0	-7.7	-1.4	-7.0	-3.4
WMB2-363.5	1203.5	-7.4	-7.2	-6.6	-3.0
WMB2-368.0	1208.0	-6.0	-0.2	-5.2	-1.6
WMB2-368.5	1208.5	-5.7	-2.4	-4.9	-1.3
WMB2-369.5	1209.5	-5.0	-3.3	-4.2	-0.6
WMB2-370.5	1210.5	-7.3	0.1	-6.6	-3.0
WMB2-371.0	1211.0	-7.7	-3.7	-7.0	-3.4
WMB2-376.0	1216.0	-8.4	-4.5	-7.6	-4.0
WMB2-377.0	1217.0	-8.6	-3.6	-7.8	-4.2
WLN-26.0	1256.0	-7.4	-1.6	-6.7	-3.1
WLN-27.3	1257.3	-11.2	-6.9	-10.5	-6.9
WLN-28.0	1258.0	-9.5	-3.5	-8.8	-5.2
WLN-28.5	1258.5	-10.4	-7.3	-9.7	-6.1
WLN-29.0	1259.0	-11.6	-7.2	-10.9	-7.3
WLN-29.5	1259.5	-8.9	-7.9	-8.2	-4.6
WLN-30.0	1260.0	-6.5	-1.7	-5.8	-2.2
WLN-34.5	1264.5	-7.8	-4.7	-7.1	-3.5
WLN-35.0	1265.0	-6.6	-3.6	-5.9	-2.3
WLN-35.5	1265.5	-8.3	-5.4	-7.6	-4.0
WLN-36.0	1266.0	-8.1	-5.2	-7.4	-3.8
WLN-36.5	1266.5	-8.2	-5.7	-7.5	-3.8
WLN-37.0	1267.0	-9.4	-4.7	-8.7	-5.1
WLN-37.5	1267.5	-10.5	-5.0	-9.8	-6.2
WLN-40.0	1270.0	-10.6	-10.6	-9.8	-6.2
WLN-40.5	1270.5	-13.9	-11.6	-13.2	-9.6
WLN-47.5	1277.5	-8.1	-6.5	-7.4	-3.8
WLN-48.3	1278.3	-7.5	0.0	-6.8	-3.2
WLN-49.0	1279.0	-8.3	-1.3	-7.6	-4.0
WLN-49.5	1279.5	-10.7	-5.2	-10.0	-6.4
WLN-50.0	1280.0	-11.0	-4.9	-10.3	-6.7

Sample ID	meter level (m)	$\delta^{18}O$ (‰)	$\delta^{13}C$ (‰)	water $\delta^{18}O$ (‰) (T=17 °C)	water $\delta^{18}O$ (‰) (T=35 °C)
mudstone cement					
WLN-50.5	1280.5	-9.2	-3.7	-8.5	-4.9
WLN-51.5	1281.5	-12.1	-8.9	-11.4	-7.8
WLN-52.5	1282.5	-10.6	-2.7	-9.8	-6.2
WLN-53.5	1283.5	-4.4	3.8	-3.6	0.0
WLN-54.0	1284.0	-10.9	-3.9	-10.2	-6.6
WLN-54.5	1284.5	-10.7	-2.1	-10.0	-6.4
WLN-66.5	1296.5	-7.2	-7.9	-6.5	-2.9
WLN-67.0	1297.0	-8.5	-0.5	-7.7	-4.1
WLN-70.0	1300.0	-9.6	-2.7	-8.8	-5.2
WLN-72.5	1302.5	-5.7	-4.1	-5.0	-1.3
WLN-73.5	1303.5	-8.3	-16.7	-7.6	-4.0
WLN-75.0	1305.0	-8.7	-16.0	-8.0	-4.4
WLN-82.5	1312.5	-7.3	-3.0	-6.6	-3.0
WLN-128.2	1358.2	-6.3	-5.4	-5.6	-2.0
WLN-129.0	1359.0	-6.4	-7.5	-5.7	-2.1
WLN-130.5	1360.5	-7.6	-1.2	-6.9	-3.3
WLN-142.5	1372.5	-9.4	-10.6	-8.6	-5.0
WLN-168.0	1398.0	-6.8	1.0	-6.0	-2.4
WLN-174.0	1404.0	-7.7	-0.2	-7.0	-3.3
WLN-205.5	1435.5	-8.5	-1.4	-7.8	-4.2
WLN-218.7	1448.7	-6.3	0.5	-5.6	-2.0
WLN-219.5	1449.5	-6.7	-0.1	-6.0	-2.4
pedogenic carbonate					
WMB-80.0	860.0	-9.8	-6.7		-5.5
WMB-96.5	876.5	-9.4	-7.6		-5.0
WMB-102	882.0	-9.7	-8.0		-5.4
WMB-104.5	884.5	-8.5	-6.6		-4.2

Sample ID	meter level (m)	$\delta^{18}O$ (‰)	$\delta^{13}C$ (‰)	water $\delta^{18}O$ (‰) (T=17 °C)	water $\delta^{18}O$ (‰) (T=35 °C)
10 samples from hand specimen FU-373					
FU-37301	373.0	-8.3	1.7	-7.6	-4.0
FU-37302	373.0	-8.4	1.8	-7.6	-4.0
FU-37303	373.0	-8.7	1.8	-8.0	-4.4
FU-37304	373.0	-8.7	1.6	-7.9	-4.3
FU-37305	373.0	-8.5	2.0	-7.8	-4.2
FU-37306	373.0	-8.1	2.0	-7.4	-3.8
FU-37307	373.0	-7.9	2.9	-7.2	-3.6
FU-37308	373.0	-8.3	1.6	-7.6	-4.0
FU-37309	373.0	-8.5	2.0	-7.8	-4.2
FU-37310	373.0	-8.8	1.5	-8.1	-4.5

Chapter 4 Continental hydroclimate during the late Paleocene-early Eocene greenhouse in the Greater Green River Basin, Southwestern Wyoming, U.S.A.

Abstract

Despite the fact that the late Paleocene to early Eocene (LPEE, ~59-50 Ma) is the most recent geologic analogue to future climate and environment when Earth's atmospheric CO_2 concentration (pCO_2) increases significantly due to fossil fuel burning, how high the atmospheric pCO_2 was and how wet or dry continental hydroclimate was during this warm period and its hyperthermals remain debated. In this study, we build a high-resolution record of paleosol morphology, bulk organic carbon isotope composition, and chemical index of alteration without potassium (CIA-K) in the Greater Green River Basin, western U.S.A., in order to examine the hydroclimate in the continental interior during the warm LPEE. We also reconstruct the atmospheric pCO_2 using carbon isotope compositions in paleosol carbonate nodules. Two negative carbon isotope excursions (CIEs) were recognized in our carbon isotope record, very likely representing two early Paleogene hyperthermal events: PETM and ETM-2. Our reconstructed atmospheric pCO_2 within the PETM is generally in the range of 600-1200 ppm, which is 2-3 times higher than preindustrial. Our estimated mean annual precipitation (MAP) based on CIA-K proxy was generally high (400-1600 mm) during the LPEE, but low (400-800 mm) during the hyperthermals. Poorly

drained green paleosols and/or water-logged histosols dominated the floodplain deposition during most of the time in the LPEE, while well drained red-brown paleosols and carbonate-rich calcisols only developed in the hyperthermals. Our record suggests that the continental climate was generally humid and warm during the LPEE, and transient drying happened during the hyperthermals.

Keywords: continental hydroclimate, bulk organic carbon, paleosol, PETM, atmospheric pCO_2, CIA-K, precipitation

4.1 Introduction

Continental hydroclimates of the late Paleocene-early Eocene (LPEE, 59-50 Ma) greenhouse are fundamental to the understanding of the potential impact of future global warming (e.g., McInerney and Wing, 2011). During this warm period, benthic foraminifera $\delta^{18}O$ values decreased at least 1.0 ‰, representing ~4 °C increase in ocean bottom temperature (Zachos et al., 2001). This period contains several short-term hyperthermal events and the warm climate culminated at the Early Eocene Climatic Optimum (EECO) during 52-50 Ma (Zachos et al., 2001). It has been suggested that the warm global climate during the LPEE was associated with injection of a very large mass of ^{13}C-depleted carbon into the atmosphere or ocean (e.g., Zachos et al., 2008). Possible sources of the carbon include: 1) deeply buried rocks that were liberated as methane and CO_2 by intrusive volcanisms (Svensen et al., 2004); 2) high methane fluxes from large marine gas hydrate capacitors as a result of increasing deep-sea water temperature

(e.g., Dickens, 2003); 3) metamorphic decarbonation of carbonate-rich pelagic sediments and release of CO_2 when the Tethyan oceanic crust was subducted during the India and Eurasia collision (e.g., Caldeira, 1992; Kent and Muttoni, 2008); or 4) repeated, large-scale releases of dissolved organic carbon from the ocean by ventilation of the ocean interior (e.g., Sexton et al., 2011).

Paleoclimate during the LPEE has been relatively well studied in the marine realm, however, the responses of continental climate and environment to such extreme climate conditions remain less well understood. Sedimentary basins in the western U.S.A. provide a rich archive of terrestrial hydroclimate for this warm period, and many studies have been conducted to examine the contemporaneous climatic and ecological responses based on paleopedology, stable isotopic analysis, and climate modeling (e.g., Koch et al., 1995; Bowen et al., 2001; Sewall and Sloan, 2006; Hren et al., 2010; Hyland and Sheldon, 2013; Hyland et al., 2013, Snell et al., 2013). However, most of these studies focus only on a short period of the early Paleogene, such as the most well studied Paleocene-Eocene Thermal Maximum (PETM) and Early Eocene Climatic Optimum (EECO) (e.g., Bowen et al., 2001, 2004; McInerney and Wing, 2011; Hyland et al., 2013). Up to now, long and continuous terrestrial climate records covering the entire early Paleogene are rare.

The hyperthermal events occurred during the LPEE warm period include the most dramatic PETM at ~55 Ma and smaller Eocene Thermal Maximum 2 and 3

(ETM-2, ETM-3) occurred at ~53.5 Ma and ~52.8 Ma, respectively (e.g., Zachos et al., 2001; Lourens et al., 2005; Sluijs et al., 2009; Abels et al., 2012; Schneider-Mor and Bowen, 2013). The PETM is characterized by a more than 1.0 ‰ negative excursion of deep-sea carbonate $\delta^{18}O$ values and ~4-8 °C increase of deep-sea temperature within a duration of ~100 kyr (e.g., Kennett and Stott, 1991; Röhl et al., 2000; Zachos et al., 2003; Tripati and Elderfield, 2005; Röhl et al., 2007). The PETM is also expressed as a ~3-8 ‰ negative Carbon Isotope Excursion (CIE) of the marine, atmospheric, and terrestrial carbon reservoirs (e.g., Kennett and Stott, 1991; Zachos et al., 2001; Koch et al., 2003; Pagani et al., 2006; Baczynski et al., 2016). In the Bighorn Basin in western U.S.A., the PETM and ETM-2 have been characterized by negative CIEs in isotope records of terrestrial soil carbonate and bulk organic matter (e.g., Koch et al., 1995; Stott et al. 1996; Wing et al. 2005; Hyland et al., 2013; Baczynski et al., 2016; Abels et al., 2016).

The paleoenvironmental condition in continental mid-latitude during the extreme hyperthermal events and the atmospheric pCO_2 during the LPEE have been debated. A global increase in wetland deposits during the PETM was used to suggest intensified precipitation (Sloan et al., 1992, 1999), which was supported by clay mineral assemblages that suggest wetter conditions (e.g., Robert and Kennett, 1994), and climate modeling that suggests wetter subtropical environment (e.g., Rind, 1998). However, other sedimentologic studies in Europe

suggest dry conditions (Schmitz et al., 2001; Schmitz and Pujalte, 2003), which is consistent with a paleosol morphology study and precipitation reconstruction in the Bighorn Basin in the western U.S.A. (Kraus et al., 2013). Based on paleosol carbon isotope records, Sinha and Stott (1994) proposed that the atmospheric pCO_2 during the LPEE was generally between 300 and 700 ppm. Paleosol carbon isotope studies in the Wind River Basin (Fan et al., 2011; Hyland et al., 2013) suggest that the atmospheric pCO_2 ranged from 350 to 1265 ppm during the EECO.

In order to improve our understanding of mid-latitude terrestrial responses to the global climate changes during the LPEE, we conducted a multi-method study on the early Paleogene floodplain deposits in the Greater Green River Basin in southwest Wyoming. Specifically, this study described paleosol morphology; built a high-resolution, continuous organic carbon isotope record that identifies major LPEE hyperthermal events present in our section; reconstructed pCO_2 levels using carbon isotope compositions of paleosol carbonates and organic materials, and mean annual precipitation (MAP) using the chemical index of alteration without potassium (CIA-K) of bulk sediments in the B-horizons of paleosols. The identification of the PETM and ETM-2 help to improve the age constraint of the lower Paleogene strata in the study area because the timings of PETM and other smaller hyperthermal events have been well constrained by

magnetostratigraphy in the nearby Bighorn Basin (e.g., Koch et al., 2003; Kraus and Riggins, 2007; Clyde et al., 2007).

4.2 Geologic setting

4.2.1 Tectonic background

The Greater Green River Basin was located in the Sevier foreland during the Late Cretaceous, and evolved into an isolated intermontane basin during the latest Cretaceous-early Eocene Laramide orogeny (Dickinson et al., 1988; DeCelles, 2004; Gao et al., 2016). The basin is bounded by the Sevier thrust belt to the west, the Wind River Range and Granite Mountains to the north, the Rawlins uplift and Sierra Madre Mountains to the east, and the Uinta Mountains to the south (Figure 4-1). The basin is divided into four structural and topographic subbasins including the Green River, Great Divide, Washakie, and Sand Wash basins by several intrabasinal anticlines, which are the Rock Springs uplift, the Wamsutter arch, and the Cherokee Ridge (Fidlar, 1950). This study followed the 1400-m-thick measured stratigraphic section presented in Chapter 3, which is located to the southeast of the Rock Springs Uplift (Figure 4-1).

4.2.2 Basin stratigraphy and age constraints

The studied lower Paleogene strata in the Greater Green River Basin include the Paleocene Fort Union Formation and the lowermost Eocene main body of the Wasatch Formation. The Fort Union Formation predominantly contains mudstone and paleosol with minor amount of thin sandstone and coal beds, which were

interpreted to be deposited in a distal floodplain environment (Gao and Fan, in review). The Wasatch Formation contains massive granule- to pebble-conglomerate and thick trough cross-stratified sandstone that were deposited in braided channels and mudstone and paleosols formed in floodplain environments (Gao and Fan, in review). The Wasatch Formation is overlain by the lacustrine Green River Formation (e.g., Shuster and Steidtmann, 1988; Roehler, 1992).

The age determination of the lower Paleogene sedimentary rocks in the study area is based mainly on land mammal fossil assemblages, which were calibrated to the absolute geologic time scale based on paleomagnetostratigraphy and radiometric dating of ash beds in other basins (e.g., Clyde et al., 1997). Mammal fossils of *Diacodon, Gelastops, Mixodectes, Paleotomus, Promioclaenus,* etc., typical to the early Torrejonian land mammal stage (To_2, ~61.3-62.3 Ma), were found in the Fort Union Formation ~8 km south of our studied locality (Rigby et al., 1980). Age-diagnostic fossils were previously documented at several stratigraphic levels in other measured sections of the Wasatch Formation near our studied section (Roehler, 1992). These stratigraphic levels can be correlated to our section based on their levels in the Paleocene and lowermost Eocene sequences and lithostratigraphic correlations. The presence of *Hyracotherium, Hyopsodus, Haplomylus, Diacodexis,* etc. in the main body of the Wasatch Formation in several localities places the deposition during the early and middle Wasatchian stage (Wa_0-Wa_5, ~55.0-53.4 Ma), and the presence of *Heptodon, Lambdotherium,*

Meniscotherium, etc. in the Niland Tongue of the Wasatch Formation, stratigraphically above our studied section, places the upper limit of the top of the main body of the Wasatch Formation to the late Wasatchian stage (Wa_6-Wa_7, ~52.9-52.6 Ma) (e.g., Roehler, 1992; Tauxe et al., 1994). The dating status of the whole basin is similar to the study site, with age constraints relying mainly on land mammal fossil assemblages and pollen biostratigraphy (e.g., Roehler, 1987; 1992; Honey, 1988; Woodburne, 2004), and paleomagnetostratigraphy and radiometric dating of volcanic ash beds conducted on some intervals of the Eocene strata (e.g., Mauger, 1977; Machlus et al., 2004).

4.3 Methods

Four types of data were collected to reconstruct the continental hydroclimate during the LPEE in the Greater Green River Basin, including paleosol morphology observations documenting the change in paleosol type; a high-resolution bulk organic carbon isotope record for the identification of hyperthermal events based on CIEs and estimated depositional ages; coupled carbon isotope compositions of paleosol carbonates and organic materials to reconstruct pCO_2; and CIA-K of paleosol B-horizons for the reconstruction of MAP. The paleosol classification and description in this study are mainly based on the field observations of soil texture, soil structure, mottled color and mineral accretions (e.g., Mack et al. 1993; Kraus et al., 2013).

4.3.1 Carbon isotope analysis

Carbon isotope analysis in this study includes bulk organic matter carbon isotopic analysis ($\delta^{13}C_{org}$), and carbonate carbon isotopic analysis ($\delta^{13}C_{cc}$). Bulk paleosol and mudstone samples were collected every 0.5-1.0 m from the floodplain facies throughout the measured section, and pedogenic carbonate nodules were collected where available. Fresh bulk paleosol and mudstone samples were collected after removing the surface layers to avoid any possible contamination from recent organic material. Pedogenic carbonate nodules were collected at a depth of >30 cm below the paleosol surface in order to exclude the influence of diffusing atmospheric CO_2. X-ray diffraction (XRD) analysis show that our carbonate samples are dominated by low-magnesium calcite, and cathodoluminescence microscope show that the carbonate samples are predominantly micritic, and dolomite and spars only present in the upper 200 m of the main body of Wasatch Formation (Gao and Fan, in review). Careful evaluation suggests these carbonates did not experience major diagenetic influence (Gao and Fan, in review).

For $\delta^{13}C_{org}$ analysis, the samples were examined under a microscope and any obvious modern organic matter was removed by hand picking. Samples were then powdered using a ceramic mortar and pestle and weighted into open silver capsules. Carbonate in the powdered samples was removed using hydrogen chloride fumigation method. Samples were loaded into silver capsules and wetted

by adding one drop of DI water. Open silver capsules were placed in a sealed desiccator containing a beaker of 12 N fuming HCl for at least four days, then dried in oven at 75 °C for at least 12 hours. Each silver capsule was then carefully placed in a tin capsule and tightly packed and loaded into a Costech ECS 4010 Analyzer, which was connected to a Delta V Advantage Mass Spectrometer via ConFlo IV, at the University of Texas at Arlington. The isotope ratios were calibrated using USGS 40, USGS 41, and an in-house standard. The precision of $\delta^{13}C_{org}$ is better than ±0.2 ‰ (1σ) based on repeated analysis of standards. The $\delta^{13}C_{org}$ values are reported relative to Vienna Pee Dee Belemnite (VPDB) (Table 4-1).

For $\delta^{13}C_{cc}$ analysis, the carbonate samples were powdered using a ceramic mortar and pestle. Powdered samples were weighed and loaded into sample vials. After flushing the vials using ultrapure helium, dehydrated phosphoric acid was injected into the vials to react with the samples at 70 °C. The $\delta^{13}C$ values of the resulted CO_2 were analyzed using a Gasbench II and a Delta V Advantage Mass Spectrometer at the University of Texas at Arlington. The isotope ratios are calibrated using NBS-19, NBS-18, and an in-house standard. The precision of $\delta^{13}C$ values is better than ±0.2 ‰ (1σ) based on repeated analysis of standards. All the isotope values of carbonate are reported relative to VPDB.

4.3.2 pCO_2 reconstruction

We followed Eq. (1) that was presented in Cerling (1999) for atmospheric pCO_2 reconstruction.

$$pCO_2(ppmv) = S_z\left(\frac{\delta^{13}C_s - 1.0044 * \delta^{13}C_r - 4.4}{\delta^{13}C_a - \delta^{13}C_s}\right) \quad (1)$$

Soil CO_2 is a mixture of atmospheric CO_2 and soil-respired CO_2 (produced by biological respiration) (Breecker and Retallack, 2014). S_z is the concentration of soil-respired CO_2 and is commonly assumed as summer minimum soil-respired CO_2 because soil carbonates are likely to precipitate preferentially during warm seasons (Breecker et al., 2009; Passey et al., 2010; Quade et al., 2013; Hough et al., 2014). $\delta^{13}C_s$ is determined from paleosol carbonate $\delta^{13}C_{cc}$ and the crystallization temperature (T) of the paleosol carbonate using the temperature-sensitive equilibrium isotope fraction factor between calcite and CO_2 Eq. (2) (Romanek et al., 1992):

$$\delta^{13}C_s = \frac{\delta^{13}C_{cc} + 1000}{\frac{(11.98 - 0.12T)}{1000} + 1} - 1000 \quad (2)$$

$\delta^{13}C_r$ is the carbon isotope composition of soil-respired CO_2, and was traditionally represented by paleosol $\delta^{13}C_{org}$ values (e.g., Cerling, 1992; Retallack, 2009). However, several studies have shown that bulk $\delta^{13}C_{org}$ values in modern soils are similar to litter near the surface, but increase with depth (e.g. Torn et al., 2002; Wynn et al., 2005; Wynn and Bird, 2007). Therefore organic carbon in soil B-horizons, which are typically sampled when working with paleosol carbonate,

have $\delta^{13}C$ values higher than the average biomass, and the $\delta^{13}C_r$ in Eq. (1) can be represented by measured $\delta^{13}C_{org}$ values minus 1 ‰ (Bowen and Beerling, 2004; Breecker, 2013). $\delta^{13}C_a$ is the estimated atmospheric carbon isotopic composition, which was -6.1 ‰ during the early Eocene (Tipple et al., 2010).

The least well constrained parameter in Eq. (1) is S(z), which varies both with depth and time (Breecker et al., 2009, 2013, 2014). Previous studies have suggested that S(z) can be derived from its relationship to depth of sampled soil horizon to the carbonate accumulation zone (Retallack, 2009), mean annual precipitation (MAP) (Cotton and Sheldon, 2012), and soil order (Breecker, 2013; Montañez, 2013). Breecker and Retallack (2014) compared these three approaches by applying them to Miocene paleosols from Montana, U.S.A., and Rusinga Island, Kenya, and suggested that the tabulated and revised soil order-based S(z) values are most reliable, thus we adopt this approach in our study.

4.3.3 MAP reconstruction

Bulk paleosol samples from the B-horizons were analyzed for major elements concentration using a Shimadzu EDX-7000 X-ray fluorescence (XRF) spectrometer at the University of Texas at Arlington. The reported weight percentages were calibrated using three USGS standards: SDO-1 (Devonian Ohio Shale), SBC-1 (Brush Creek Shale), and SGR-1 (Green River Shale) (Table 4-2, Table 4-3). The weight percentages were then recalculated to molar ratios, following Sheldon et al. (2002). Since the intensity of chemical weathering of

paleosols depends in part on precipitation, Sheldon et al. (2002) developed an empirical relationship (Eq. (3)) relating the mean annual precipitation (MAP) to the chemical index of alteration without potassium (CIA-K) using soil molecular oxide data from Marbut (1935):

$$\mathrm{CIA-K} = [\mathrm{Al_2O_3}/(\mathrm{Al_2O_3} + \mathrm{CaO} + \mathrm{Na_2O})] \times 100$$

$$\mathrm{MAP\,(millimeters/year)} = 221e^{0.0197*\mathrm{CIA-K}};\ r^2 = 0.72 \qquad (3)$$

The chemical index CIA-K, which omits potassium (K), is used here because diagenesis can yield elevated potassium (K) concentrations in paleosols. The error associated with the regression analysis is ±181 mm (Sheldon et al., 2002; Sheldon and Tabor, 2009).

4.4 Results

4.4.1 Paleosol description

Fort Union Formation

Many coal beds were developed in the floodplain facies of the Fort Union Formation (Figure 4-2). Based on the classification of paleosols in Mack et al. (1993), the coal beds are of histosol because each coal originates as a water-logged surface horizon containing a high concentration of plant debris, called histic epipedon (Soil Survey Staff, 1975; Buol, 1980). A typical succession that contains a coal bed (histosol) in the Fort Union Formation is illustrated in Figure 4-2. Below each coal bed is usually a sequence of mudstone with color changes from light grey to dark grey toward the coal, representing upward increase of

organic matter content. Above each coal bed is usually a short sequence of tan or greyish mudstone, which gradually change upward into very fine- to fine-grained and laminated sandstone.

Main body of the Wasatch Formation

Most of the paleosols in the main body of the Wasatch Formation are ancient analogs to vertisols based on their high clay content and vertic features including wedge-shaped peds, hummock and swale structure, and slickensides (e.g., Mack et al., 1993; Nettleton et al., 2000; Driese et al., 2005). Only several calcisols were identified in the bottom part of this formation based on the presence of carbonate nodules (e.g., Mack et al., 1993; Nettleton et al., 2000; Driese et al., 2005). Peds are structural units that consist of primary particles bound together by cementing agents like organic matter, clay, and hydrous oxides of iron and aluminum. Slickensides are smooth shear surfaces on the peds. Mineral accretions in soils include three types according to the degree of development: 1) masses that are least strongly developed, with irregular shape and diffusive boundaries; 2) accumulations with irregular to regular shape and localized inclusions of matrix material, and cannot be readily separated from the matrix; 3) nodules that are the most strongly developed, with sharp boundaries, and are readily physically separated from the matrix (Kraus et al., 2013). Colored mudstones typically represent the B-horizons of ancient soils, and commonly contain pedogenic carbonate nodules as well as other pedogenic minerals (Bown and Kraus, 1981,

1987). The B-horizons of our calcisols were identified based on the presence of carbonate nodules, and the B-horizons of our vertisols were identified based on the development of peds, clay coatings, and red and yellow mottled colors from accumulation of iron oxides (e.g., Mack et al., 1993; Daniels and Haering, 2006). Based on the different matrix colors of B-horizons, we further divide the vertisols into green paleosols and red-brown paleosols.

The lower 400 m of the main body of the Wasatch Formation mainly has green paleosols (Figure 4-2). Several paleosols often can be found in a thick sequence of mudstone, sometimes in one paleosol profile a downward increasing trend of ped size from less than 1 cm to up to 10 cm can be observed. The greenish color matrixes in the B-horizons are mottled to yellow or reddish color locally because of the iron oxides accumulation, and sometimes carbonate accumulations up to 10 cm can be observed (Figure 4-2c, d and e). Only several calcisols are present in the Wasatch Formation (Figure 4-2b), their B-horizons typically have gray color and do not have structures like peds or slickensides. The major differences between the upper 250 m of the main body of the Wasatch Formation and the lower 400 m are: 1) the green paleosols in the upper 250 m have more mottled colors including yellow, blue, purple and red (Figure 4-2g, h); 2) several red-brown paleosols are found in this part (Figure 4-2f); and 3) no calcisols are present.

4.4.2 Carbon record and MAP

The $\delta^{13}C_{org}$ values of the organic-rich carbonaceous shale that is usually accompanied with coal beds in the Paleocene Fort Union Formation vary between -23.2 ‰ and -26.5 ‰, with an average of -25.0 ‰ (Table 4-1, Figure 4-3). The $\delta^{13}C_{org}$ values of the paleosol B-horizons in the main body of the lower Eocene Wasatch Formation vary between -24.0 ‰ and -28.7 ‰, with an average of -26.2 ‰ (Table 4-1, Figure 4-3). The $\delta^{13}C_{org}$ values of the non-pedogenic mudstone samples have larger variations compared to the paleosols. In the Fort Union Formation, the $\delta^{13}C_{org}$ values of mudstone samples vary between -21.9 ‰ and -26.7 ‰, with an average of -24.7 ‰ (Table 4-1, Figure 4-3). In the main body of the Wasatch Formation, these $\delta^{13}C_{org}$ values vary between -22.5 ‰ and -29.4 ‰, with an average value of -26.2 ‰ (Table 4-1, Figure 4-3). At ~80 m above the base of the Wasatch Formation, the $\delta^{13}C_{org}$ values show a transient initial drop of ~4 ‰, and the CIE spans ~70 m on the record (Figure 4-3). A second CIE with lower magnitude, ~2 ‰, spanning ~100 m near the top of the main body of Wasatch Formation is also observed (Figure 4-3). Reconstructed atmospheric pCO_2 from four calcisols within the stratigraphic interval of the first CIE is of 600-1200 ppm. The estimated MAP throughout the Paleocene and the earliest Eocene is generally high, in the range of 400-1600 mm (Table 4-3, Figure 4-4). Low values (400-800 mm) occur at the stratigraphic levels of the two negative CIEs (Figure 4-4).

4.5 Discussion

4.5.1 Recognition of hyperthermals

Two short-term negative $\delta^{13}C_{org}$ excursions occurred in our record (Figure 4-3, Figure 4-4). The first one is of high magnitude, ~4 ‰, and occurred above the boundary of the Fort Union Formation and the Wasatch Formation, which is roughly at the Paleocene-Eocene boundary. The magnitude of this CIE is consistent with, or smaller than the magnitudes of CIEs of PETM in both marine and continental records. In marine benthic foraminifera record, the PETM is expressed as a ~3 ‰ CIE (e.g., Zachos et al., 2001). Continental records show that the CIE during the PETM has variable magnitude, depending on the type of samples studied. Such CIE records include a ~6 ‰ drop based on studies of bulk organic matter in the Paris Basin, France (Sinha et al., 1995; Magioncalda et al., 2001), a ~6-8 ‰ drop based on studies of paleosol carbonates in the Bighorn Basin (Bowen et al., 2001; Koch et al., 2003; Abels et al., 2016), a ~5 ‰ drop based on a study of mammalian tooth enamel in the Bighorn Basin (Secord et al., 2012), and a 4-5 ‰ drop based on studies of bulk organic matter and n-C_{29} alkane in leaf wax in the Bighorn Basin (Baczynski et al., 2013, 2016). The depositional duration of this CIE in our record seems also to match the duration of PETM in the Bighorn Basin. Our CIE spans ~70 m, while the stratigraphic interval of PETM in the Bighorn Basin varies between 40 m and 100 m depending on study location (Bowen et al., 2001; Koch et al., 2003; Secord et al., 2012; Baczynski et

al., 2013, 2016). Therefore, we suggest our first CIE is the PETM. The variations in CIE magnitude in different locations could reflect differences in soil properties and/or in the type of C3 vegetation (e.g., Cerling and Quade, 1993), the mixing of carbon from different sources (e.g., autochthonous or allochthonous), and different degrees of organic matter degradation (Baczynski et al., 2013, 2016).

The second CIE is of lower magnitude, ~2 ‰, which occurred after the Paleocene-Eocene boundary, but before 53 Ma based on the biostratigraphic age constraint of our studied strata (Figure 4-3, Figure 4-4). ETM-2 is the most pronounced PETM-like hyperthermal event that occurred during the early Eocene, and is expressed as a ~1 ‰ negative CIE in marine bulk sediment records (Zachos et al., 2010). In the continental environment, ETM-2 has been documented as a ~3 ‰ drop in the Bighorn Basin measured in paleosol carbonates (Abels et al., 2016). Our record does not show an ideal CIE that could precisely represent the ETM-2, but the timing and magnitude of the excursion indicate that it was likely ETM-2, or a combination of ETM-2 and other smaller hyperthermals that happened within the next ~500 kyr of ETM-2 (e.g., Cramer et al., 2003; Lourens et al., 2005).

We estimate the duration of PETM in the Greater Green River Basin and compare that with the nearby Bighorn Basin. Our measured section of the main body of the Wasatch Formation has a total thickness of ~650 m. Based on the land mammal fossil age constraints summarized in section 3.2, the time span of this

section is 1.5-2 myr. By assuming that the sedimentation rate did not change, our estimated sedimentation rate of the main body of the Wasatch Formation is 330-430 m/myr. Based on this estimated sedimentation rate, the PETM lasted for 160-200 kyrs in our study site. The PETM in the Bighorn Basin spans ~40 m (Kraus et al., 2013), and the sedimentation rate was ~470 m/myr in the basin during the early Eocene (Gingerich, 2000). Therefore, the PETM lasted for ~85 kyrs in the Bighorn Basin. Better constraints on the sedimentation rate are needed in order to resolve the duration of PETM more precisely in our study site.

4.5.2 Humid LPEE and transient drying during the hyperthermals

Our estimated MAP is relatively low, 400–800 mm, during the hyperthermals intervals, while the estimated MAP is 400-1600 mm during the entire LPEE (Figure 4-4), suggesting transient drying during the hyperthermals within the generally humid LPEE. Kraus et al. (2013) reconstructed the MAP in the Bighorn Basin based on a ~70 m thick interval of paleosols covering the PETM, their results show that the MAP values in the pre- and post-PETM intervals are generally high, in the range of 1100–1500 mm, and the values dropped to 800–1100 mm during the body of PETM. A dry PETM was also suggested from a sedimentology study in the Axehandle Basin in central Utah (Bowen and Bowen, 2008), and a leaf physiognomy study in the Bighorn Basin (Wing et al., 2005). Our records show consistent pattern but even drier hyperthermals than the Bighorn Basin (Kraus et al., 2013). The low MAP could be a possible cause of the

smaller magnitude of CIE during the PETM compared to the other terrestrial records, because a drier climate would contribute to higher $\delta^{13}C_{org}$ values through lower soil productivity and water stress effects on plant isotope compositions (Cerling and Quade, 1993; Ehleringer and Monson, 1993).

The development of different types of paleosols throughout our measured section also supports the inferred wet and dry conditions based on MAP estimates. During the Paleocene, the floodplains were generally water-logged and had histosols (coal beds) developed, indicating that the climate was wet. During the early Eocene, paleosol types within the hyperthermals are different compared to those not in the hyperthermals. Within the hyperthermals, well drained red-brown paleosols and calcisols developed, which is consistent with our low MAP values. Outside of the hyperthermals, the floodplain deposition was dominated by poorly drained green paleosols, indicating wet climate. Soil type representing wet paleoclimate changed from histosols during the Paleocene to green paleosols during the early Eocene, possibly reflecting a change in ecosystem when climate became very hot during the early Eocene.

The transient drying during the early Paleogene hyperthermals may be explained by the midlatitude bypass mechanism, which was proposed to explain the elevated runoff and Deuterium-enriched precipitation in the Arctic during the PETM (Pagani et al., 2006). Decreased meridional temperature gradients during the PETM might have reduced rainout of water vapor by synoptic eddies in the

middle latitudes, and increased moisture delivery to the high latitudes, because a decreased temperature gradient provides a smaller energy supply for synoptic eddies (Pierrehumbert, 2002; Pagani et al., 2006). This mechanism predicts temporally drier conditions during the PETM than other times in early Paleogene in the middle latitudes, and spatially drier conditions in the southerly sites than in the northerly sites in Wyoming during the PETM (Bowen and Bowen, 2008), which is supported by our reconstructed MAP during the PETM being lower in the Greater Green River Basin compared to the Bighorn Basin (Kraus et al., 2013). In addition, Bowen and Bowen (2008) found that the CIE in central Utah was ~2 ‰ smaller than that observed in the Bighorn Basin (Bowen et al., 2001) during the PETM, and suggested the smaller CIE could have been caused by drier conditions (Bowen et al., 2004; Bowen and Bowen, 2008). The speculative correlation of the PETM with a ~15-m-thick evaporite sequence deposited in the Flagstaff lake system in central Utah also supports a significant increase in regional aridity during the PETM (Bowen et al., 2008).

The transient drying during the early Paleogene hyperthermals, however, is contrary to climate model predictions. By using the Community Climate System Model (CCSM3) with atmospheric CO_2 concentrations of 4×, 8×, and 16× the preindustrial value, Winguth et al. (2010) demonstrated that precipitation during the PETM slightly increases, and evaporation minus precipitation slightly decreases in mid to high latitudes with increased surface temperatures, and

attributed the changes to responses to CO_2 radiative forcing (also seen in Sloan and Rea, 1996 and Shellito et al., 2003). Winguth et al. (2010) suggested a decrease in MAP from lower to higher mid-latitude in North America, and attributed the trend to decrease in monsoonal moisture transport from the south during the summer. It is very likely that the difference in model predictions and proxy data is caused by the model simulation overestimating CO_2 radiative forcing because our record show that the pCO_2 during the PETM was only 2-3 times higher, not at least 4 times higher than preindustrial. The difference could also be caused by the model simulation not taking full consideration of topography development in the western US during the early Paleogene.

4.6 Conclusions

This study reports a continental hydroclimate response to warm late Paleocene-early Eocene global climate and Eocene hyperthermals. At our site in the Greater Green River Basin, the PETM is represented by a ~4 ‰ negative CIE, and the ETM-2 is represented by a ~2 ‰ negative CIE in our bulk organic carbon isotope record. The reconstructed MAP during the entire LPEE is 400-1600 mm, with low values of 400-800 mm occurring during the PETM and ETM-2, and the reconstructed atmospheric pCO_2 within the PETM is 600-1200 ppm. Our records show that the continental hydroclimate in the Greater Green River Basin during the LPEE was generally warm and humid, but transient drying occurred during the hyperthermals. The humid LPEE climate promoted formation of poorly

drained green paleosols and water-logged histosols, but transient drying led to the development of well drained red-brown paleosols and carbonate-rich calcisols in the basin.

References

Abels, H.A., Clyde, W.C., Gingerich, P.D., Hilgen, F.J., Fricke, H.C., Bowen, G.J., and Lourens, L.J., 2012, Terrestrial carbon isotope excursions and biotic change during Palaeogene hyperthermals: Nature Geoscience, v. 5, p. 326-329.

Abels, H.A., van Yperen, A.E., Zachos, J.C., Lourens, L.J., Gingerich, P.D., and Bowen, G.J., 2016, Environmental impact and magnitude of paleosol carbonate carbon isotope excursions marking five early Eocene hyperthermals in the Bighorn Basin, Wyoming: Climate of the Past, v. 12, p. 1151.

Baczynski, A.A., McInerney, F.A., Wing, S.L., Kraus, M.J., Morse, P.E., Bloch, J.I., Chung, A.H., and Freeman, K.H., 2016, Distortion of carbon isotope excursion in bulk soil organic matter during the Paleocene-Eocene thermal maximum: Geological Society of America Bulletin, v. 128, p. 1352-1366.

Bowen, G.J., and Beerling, D.J., 2004, An integrated model for soil organic carbon and CO2: Implications for paleosol carbonate pCO2 paleobarometry: Global Biogeochemical Cycles, v. 18.

Bowen, G.J., and Bowen, B.B., 2008, Mechanisms of PETM global change constrained by a new record from central Utah: Geology, v. 36, p. 379-382.

Bowen, G.J., Koch, P.L., Gingerich, P.D., Norris, R.D., Bains, S., and Corfield, R.M., 2001, Refined isotope stratigraphy across the continental Paleocene-Eocene boundary on Polecat Bench in the northern Bighorn Basin: Paleocene-Eocene Stratigraphy and Biotic Change in the Bighorn and Clarks Fork Basins, Wyoming.University of Michigan Papers on Paleontology, v. 33, p. 73-88.

Bown, T.M., and Kraus, M.J., 1987, Integration of channel and floodplain suites, I. Developmental sequence and lateral relations of alluvial paleosols: Journal of Sedimentary Research, v. 57.

Bown, T.M., and Kraus, M.J., 1981, Lower Eocene alluvial paleosols (Willwood Formation, northwest Wyoming, USA) and their significance for paleoecology, paleoclimatology, and basin analysis: Palaeogeography, Palaeoclimatology, Palaeoecology, v. 34, p. 1-30.

Breecker, D., 2013, Quantifying and understanding the uncertainty of atmospheric CO2 concentrations determined from calcic paleosols: Geochemistry, Geophysics, Geosystems, v. 14, p. 3210-3220.

Breecker, D., and Retallack, G., 2014, Refining the pedogenic carbonate atmospheric CO 2 proxy and application to Miocene CO 2: Palaeogeography, Palaeoclimatology, Palaeoecology, v. 406, p. 1-8.

Breecker, D., Sharp, Z., and McFadden, L.D., 2009, Seasonal bias in the formation and stable isotopic composition of pedogenic carbonate in modern soils from central New Mexico, USA: Geological Society of America Bulletin, v. 121, p. 630-640.

Buol, S., Hole, F., and McCracken, R., 1980, Soil genesis and classification: Ames.

Cerling, T.E., 1992, Use of carbon isotopes in paleosols as an indicator of the P (CO2) of the paleoatmosphere: Global Biogeochemical Cycles, v. 6, p. 307-314.

Cerling, T.E., 1984, The stable isotopic composition of modern soil carbonate and its relationship to climate: Earth and Planetary Science Letters, v. 71, p. 229-240.

Cerling, T.E., and Harris, J.M., 1999, Carbon isotope fractionation between diet and bioapatite in ungulate mammals and implications for ecological and paleoecological studies: Oecologia, v. 120, p. 347-363.

Cerling, T.E., and Quade, J., 1993, Stable carbon and oxygen isotopes in soil carbonates: Climate Change in Continental Isotopic Records, p. 217-231.

Clyde, W.C., Hamzi, W., Finarelli, J.A., Wing, S.L., Schankler, D., and Chew, A., 2007, Basin-wide magnetostratigraphic framework for the Bighorn Basin, Wyoming: Geological Society of America Bulletin, v. 119, p. 848-859.

Clyde, W.C., Zonneveld, J., Stamatakos, J., Gunnell, G.F., and Bartels, W.S., 1997, Magnetostratigraphy across the Wasatchian/Bridgerian NALMA boundary (early to middle Eocene) in the western Green River basin, Wyoming: The Journal of Geology, v. 105, p. 657-670.

Cotton, J.M., and Sheldon, N.D., 2012, New constraints on using paleosols to reconstruct atmospheric pCO2: Geological Society of America Bulletin, v. 124, p. 1411-1423.

Cramer, B.S., Wright, J.D., Kent, D.V., and Aubry, M., 2003, Orbital climate forcing of δ13C excursions in the late Paleocene–early Eocene (chrons C24n–C25n): Paleoceanography, v. 18.

Daniels, W.L., and Haering, K.C., 2006, Concepts of Basic Soil Science: The Mid-Atlantic Nutrient Management Handbook, p. 31.

DeCelles, P.G., 2004, Late Jurassic to Eocene evolution of the Cordilleran thrust belt and foreland basin system, western USA: American Journal of Science, v. 304, p. 105-168.

Dickens, G.R., 2003, A methane trigger for rapid warming? Science, v. 299, p. 1017-1017.

Dickinson, W.R., Klute, M.A., Hayes, M.J., Janecke, S.U., Lundin, E.R., McKITTRICK, M.A., and Olivares, M.D., 1988, Paleogeographic and paleotectonic setting of Laramide sedimentary basins in the central Rocky Mountain region: Geological Society of America Bulletin, v. 100, p. 1023-1039.

Driese, S.G., Nordt, L.C., Lynn, W.C., Stiles, C.A., Mora, C.I., and Wilding, L.P., 2005, Distinguishing climate in the soil record using chemical trends in a Vertisol climosequence from the Texas Coast Prairie, and application to interpreting Paleozoic paleosols in the Appalachian Basin, USA: Journal of Sedimentary Research, v. 75, p. 339-349.

Ehleringer, J.R., and Monson, R.K., 1993, Evolutionary and ecological aspects of photosynthetic pathway variation: Annual Review of Ecology and Systematics, v. 24, p. 411-439.

Fan, M., DeCelles, P.G., Gehrels, G.E., Dettman, D.L., Quade, J., and Peyton, S.L., 2011, Sedimentology, detrital zircon geochronology, and stable isotope geochemistry of the lower Eocene strata in the Wind River Basin, central Wyoming: Geological Society of America Bulletin, v. 123, p. 979-996.

Feng, X., Peterson, J.C., Quideau, S.A., Virginia, R.A., Graham, R.C., Sonder, L.J., and Chadwick, O.A., 1999, Distribution, accumulation, and fluxes of soil carbon in four monoculture lysimeters at San Dimas Experimental Forest, California: Geochimica Et Cosmochimica Acta, v. 63, p. 1319-1333.

Fidlar, M.M., 1950, Structural Features of the Green River Basin.

Gao, M., Fan, M., and Moucha, R., 2016, Southwestward weakening of Wyoming lithosphere during the Laramide orogeny: Journal of Geophysical Research: Solid Earth, v. 121, p. 6219-6234.

Gingerich, P.D., 2000, Paleocene/Eocene boundary and continental vertebrate faunas of Europe and North America: Gff, v. 122, p. 57-59.

Honey, J., 1988, A mammalian fauna from the base of the Eocene Cathedral Bluffs Tongue of the Wasatch Formation: Cottonwood Creek Area, Southeast Wasatch Basin, Wyoming: US Geological Survey Bulletin C, v. 1669, p. 1-13.

Hough, B.G., Fan, M., and Passey, B.H., 2014, Calibration of the clumped isotope geothermometer in soil carbonate in Wyoming and Nebraska, USA: Implications for paleoelevation and paleoclimate reconstruction: Earth and Planetary Science Letters, v. 391, p. 110-120.

Hren, M.T., Pagani, M., Erwin, D.M., and Brandon, M., 2010, Biomarker reconstruction of the early Eocene paleotopography and paleoclimate of the northern Sierra Nevada: Geology, v. 38, p. 7-10.

Hyland, E.G., and Sheldon, N.D., 2013, Coupled CO 2-climate response during the early Eocene climatic optimum: Palaeogeography, Palaeoclimatology, Palaeoecology, v. 369, p. 125-135.

Hyland, E., Sheldon, N.D., and Fan, M., 2013, Terrestrial paleoenvironmental reconstructions indicate transient peak warming during the early Eocene climatic optimum: Geological Society of America Bulletin, v. 125, p. 1338-1348.

Kennett, J., and Stott, L., 1991, Abrupt deep sea warming, paleoceanographic changes and benthic extinctions at the end of the Paleocene.

Kent, D.V., and Muttoni, G., 2008, Equatorial convergence of India and early Cenozoic climate trends: Proceedings of the National Academy of Sciences of the United States of America, v. 105, p. 16065-16070, doi: 10.1073/pnas.0805382105 [doi].

Koch, P.L., Clyde, W.C., Hepple, R.P., Fogel, M.L., Wing, S.L., and Zachos, J.C., 2003, Carbon and oxygen isotope records from paleosols spanning the Paleocene-Eocene boundary, Bighorn Basin, Wyoming: Special Papers-Geological Society of America, p. 49-64.

Koch, P.L., Zachos, J.C., and Dettman, D.L., 1995, Stable isotope stratigraphy and paleoclimatology of the Paleogene Bighorn Basin (Wyoming, USA): Palaeogeography, Palaeoclimatology, Palaeoecology, v. 115, p. 61-89.

Kraus, M.J., McInerney, F.A., Wing, S.L., Secord, R., Baczynski, A.A., and Bloch, J.I., 2013, Paleohydrologic response to continental warming during the Paleocene–Eocene Thermal Maximum, Bighorn Basin, Wyoming: Palaeogeography, Palaeoclimatology, Palaeoecology, v. 370, p. 196-208.

Kraus, M.J., and Riggins, S., 2007, Transient drying during the Paleocene–Eocene Thermal Maximum (PETM): analysis of paleosols in the Bighorn Basin, Wyoming: Palaeogeography, Palaeoclimatology, Palaeoecology, v. 245, p. 444-461.

Lourens, L.J., Sluijs, A., Kroon, D., Zachos, J.C., Thomas, E., Röhl, U., Bowles, J., and Raffi, I., 2005, Astronomical pacing of late Palaeocene to early Eocene global warming events: Nature, v. 435, p. 1083-1087.

Machlus, M., Hemming, S.R., Olsen, P.E., and Christie-Blick, N., 2004, Eocene calibration of geomagnetic polarity time scale reevaluated: Evidence from the Green River Formation of Wyoming: Geology, v. 32, p. 137-140.

Mack, G.H., James, W.C., and Monger, H.C., 1993, Classification of paleosols: Geological Society of America Bulletin, v. 105, p. 129-136.

Marbut, C.F., and Baker, O.E., 1935, Atlas of American Agriculture: Soils of the United States: US Government Printing Office.

Mauger, R.L., 1977, K-Ar ages of biotites from tuffs in Eocene rocks of the Green River, Washakie, and Uinta basins, Utah, Wyoming, and Colorado: Rocky Mountain Geology, v. 15, p. 17-41.

Maynard, J., 1992, Chemistry of modern soils as a guide to interpreting Precambrian paleosols: The Journal of Geology, v. 100, p. 279-289.

McInerney, F.A., and Wing, S.L., 2011, The Paleocene-Eocene Thermal Maximum: a perturbation of carbon cycle, climate, and biosphere with implications for the future: Annual Review of Earth and Planetary Sciences, v. 39, p. 489-516.

Montanez, I.P., 2013, Modern soil system constraints on reconstructing deep-time atmospheric CO 2: Geochimica Et Cosmochimica Acta, v. 101, p. 57-75.

Nesbitt, H., and Young, G., 1982, Early Proterozoic climates and plate motions inferred from major element chemistry of lutites: Nature, v. 299, p. 715-717.

Nettleton, W., Olson, C., and Wysocki, D.A., 2000, Paleosol classification: problems and solutions: Catena, v. 41, p. 61-92.

Pagani, M., Caldeira, K., Archer, D., and Zachos, J.C., 2006, An ancient carbon mystery: Science-New York then Washington-, v. 314, p. 1556.

Pagani, M., Zachos, J.C., Freeman, K.H., Tipple, B., and Bohaty, S., 2005, Marked decline in atmospheric carbon dioxide concentrations during the Paleogene: Science (New York, N.Y.), v. 309, p. 600-603, doi: 1110063 [pii].

Passey, B.H., Levin, N.E., Cerling, T.E., Brown, F.H., and Eiler, J.M., 2010, High-temperature environments of human evolution in East Africa based on bond ordering in paleosol carbonates: Proceedings of the National Academy of Sciences of the United States of America, v. 107, p. 11245-11249, doi: 10.1073/pnas.1001824107 [doi].

Quade, J., Eiler, J., Daeron, M., and Achyuthan, H., 2013, The clumped isotope geothermometer in soil and paleosol carbonate: Geochimica Et Cosmochimica Acta, v. 105, p. 92-107.

Retallack, G.J., 2009, Greenhouse crises of the past 300 million years: Geological Society of America Bulletin, v. 121, p. 1441-1455.

Rigby, J.K., 1980, Swain Quarry of the Fort Union Formation, Middle Paleocene (Torrejonian), Carbon County, Wyoming, Geologic Setting and Mammalian Fauna: Evolutionary Monographs, University of Chicago.

Rind, D., 1998, Latitudinal temperature gradients and climate change: Journal of Geophysical Research: Atmospheres, v. 103, p. 5943-5971.

Robert, C., and Kennett, J.P., 1994, Antarctic subtropical humid episode at the Paleocene-Eocene boundary: Clay-mineral evidence: Geology, v. 22, p. 211-214.

Roehler, H.W., 1992, Correlation, Composition, Areal Distribution, and Thickness of Eocene Stratigraphic Units, Greater Green River Basin, Wyoming, Utah, and Colorado, .

Roehler, H.W., and Martin, P., 1987, Geological Investigations of the Vermillion Creek Coal Bed in the Eocene Niland Tongue of the Wasatch Formation, Sweetwater County, Wyoming, .

Röhl, U., Bralower, T., Norris, R., and Wefer, G., 2000, New chronology for the late Paleocene thermal maximum and its environmental implications: Geology, v. 28, p. 927-930.

Röhl, U., Westerhold, T., Bralower, T.J., and Zachos, J.C., 2007, On the duration of the Paleocene-Eocene thermal maximum (PETM): Geochemistry, Geophysics, Geosystems, v. 8.

Romanek, C.S., Grossman, E.L., and Morse, J.W., 1992, Carbon isotopic fractionation in synthetic aragonite and calcite: effects of temperature and precipitation rate: Geochimica Et Cosmochimica Acta, v. 56, p. 419-430.

Schmitz, B., and Andreasson, F.P., 2001, Air humidity and lake δ18O during the latest Paleocene–earliest Eocene in France from recent and fossil fresh-water and marine gastropod δ18O, δ13C, and 87Sr/86Sr: Geological Society of America Bulletin, v. 113, p. 774-789.

Schmitz, B., and Pujalte, V., 2003, Sea-level, humidity, and land-erosion records across the initial Eocene thermal maximum from a continental-marine transect in northern Spain: Geology, v. 31, p. 689-692.

Schneider-Mor, A., and Bowen, G.J., 2013, Coupled and decoupled responses of continental and marine organic-sedimentary systems through the Paleocene-Eocene thermal maximum, New Jersey margin, USA: Paleoceanography, v. 28, p. 105-115.

Secord, R., Bloch, J.I., Chester, S.G., Boyer, D.M., Wood, A.R., Wing, S.L., Kraus, M.J., McInerney, F.A., and Krigbaum, J., 2012, Evolution of the earliest horses driven by climate change in the Paleocene-Eocene Thermal Maximum: Science (New York, N.Y.), v. 335, p. 959-962, doi: 10.1126/science.1213859 [doi].

Sewall, J.O., and Sloan, L.C., 2006, Come a little bit closer: A high-resolution climate study of the early Paleogene Laramide foreland: Geology, v. 34, p. 81-84.

Sexton, P.F., Norris, R.D., Wilson, P.A., Pälike, H., Westerhold, T., Röhl, U., Bolton, C.T., and Gibbs, S., 2011, Eocene global warming events driven by ventilation of oceanic dissolved organic carbon: Nature, v. 471, p. 349-352.

Sheldon, N.D., Retallack, G.J., and Tanaka, S., 2002, Geochemical climofunctions from North American soils and application to paleosols

across the Eocene-Oligocene boundary in Oregon: The Journal of Geology, v. 110, p. 687-696.
Sheldon, N.D., and Tabor, N.J., 2009, Quantitative paleoenvironmental and paleoclimatic reconstruction using paleosols: Earth-Science Reviews, v. 95, p. 1-52.
Shellito, C.J., Lisa C.S., and Matthew H., 2003, Climate model sensitivity to atmospheric CO_2 levels in the Early–Middle Paleogene: Palaeogeography, Palaeoclimatology, Palaeoecology, v. 193, p. 113-123.
Shuster, M.W., and Steidtmann, J.R., 1988, Tectonic and sedimentary evolution of the northern Green River basin, western Wyoming: Geological Society of America Memoirs, v. 171, p. 515-530.
Sinha, A., and Stott, L.D., 1994, New atmospheric pCO2 estimates from palesols during the late Paleocene/early Eocene global warming interval: Global and Planetary Change, v. 9, p. 297-307.
Sloan, L.C., and Rea, D.K., 1996, "Atmospheric carbon dioxide and early Eocene climate: A general circulation modeling sensitivity study.": Palaeogeography, Palaeoclimatology, Palaeoecology, v. 119, p. 275-292.
Sloan, L.C., Huber, M., and Ewing, A., 1999, Polar stratospheric cloud forcing in a greenhouse world, *in* Reconstructing Ocean History: Springer, p. 273-293.
Sloan, L.C., Walker, J.C., Moore, T., Rea, D.K., and Zachos, J.C., 1992, Possible methane-induced polar warming in the early Eocene.
Sluijs, A., Schouten, S., Donders, T.H., Schoon, P.L., Röhl, U., Reichart, G., Sangiorgi, F., Kim, J., Damsté, J.S.S., and Brinkhuis, H., 2009, Warm and wet conditions in the Arctic region during Eocene Thermal Maximum 2: Nature Geoscience, v. 2, p. 777-780.
Snell, K.E., Thrasher, B.L., Eiler, J.M., Koch, P.L., Sloan, L.C., and Tabor, N.J., 2013, Hot summers in the Bighorn Basin during the early Paleogene: Geology, v. 41, p. 55-58.
Svensen, H., Planke, S., Malthe-Sørenssen, A., Jamtveit, B., Myklebust, R., Eidem, T.R., and Rey, S.S., 2004, Release of methane from a volcanic basin as a mechanism for initial Eocene global warming: Nature, v. 429, p. 542-545.
Tauxe, L., Gee, J., Gallet, Y., Pick, T., and Bown, T., 1994, Magnetostratigraphy of the Willwood Formation, Bighorn Basin, Wyoming: new constraints on the location of Paleocene/Eocene boundary: Earth and Planetary Science Letters, v. 125, p. 159-172.
Tipple, B.J., Meyers, S.R., and Pagani, M., 2010, Carbon isotope ratio of Cenozoic CO2: A comparative evaluation of available geochemical proxies: Paleoceanography, v. 25.

Torn, M.S., Lapenis, A.G., Timofeev, A., Fischer, M.L., Babikov, B.V., and Harden, J.W., 2002, Organic carbon and carbon isotopes in modern and 100-year-old-soil archives of the Russian steppe: Global Change Biology, v. 8, p. 941-953.

Tripati, A., and Elderfield, H., 2005, Deep-sea temperature and circulation changes at the Paleocene-Eocene Thermal Maximum: Science (New York, N.Y.), v. 308, p. 1894-1898, doi: 308/5730/1894 [pii].

Winguth, A., Shellito, C., Shields, C., and Winguth, C., 2010, Climate response at the Paleocene–Eocene thermal maximum to greenhouse gas forcing—a model study with CCSM3: Journal of Climate, v. 23, p. 2562-2584.

Woodburne, M.O., 2004, Late Cretaceous and Cenozoic mammals of North America: biostratigraphy and geochronology: Columbia University Press.

Wynn, J.G., and Bird, M.I., 2007, C4-derived soil organic carbon decomposes faster than its C3 counterpart in mixed C3/C4 soils: Global Change Biology, v. 13, p. 2206-2217.

Wynn, J.G., Bird, M.I., and Wong, V.N., 2005, Rayleigh distillation and the depth profile of 13 C/12 C ratios of soil organic carbon from soils of disparate texture in Iron Range National Park, Far North Queensland, Australia: Geochimica Et Cosmochimica Acta, v. 69, p. 1961-1973.

Zachos, J.C., Dickens, G.R., and Zeebe, R.E., 2008, An early Cenozoic perspective on greenhouse warming and carbon-cycle dynamics: Nature, v. 451, p. 279-283.

Zachos, J.C., McCarren, H., Murphy, B., Röhl, U., and Westerhold, T., 2010, Tempo and scale of late Paleocene and early Eocene carbon isotope cycles: Implications for the origin of hyperthermals: Earth and Planetary Science Letters, v. 299, p. 242-249.

Zachos, J., Pagani, M., Sloan, L., Thomas, E., and Billups, K., 2001, Trends, rhythms, and aberrations in global climate 65 Ma to present: Science (New York, N.Y.), v. 292, p. 686-693, doi: 10.1126/science.1059412 [doi].

Zachos, J.C., Wara, M.W., Bohaty, S., Delaney, M.L., Petrizzo, M.R., Brill, A., Bralower, T.J., and Premoli-Silva, I., 2003, A transient rise in tropical sea surface temperature during the Paleocene-Eocene thermal maximum: Science (New York, N.Y.), v. 302, p. 1551-1554, doi: 10.1126/science.1090110 [doi].

Figures and tables

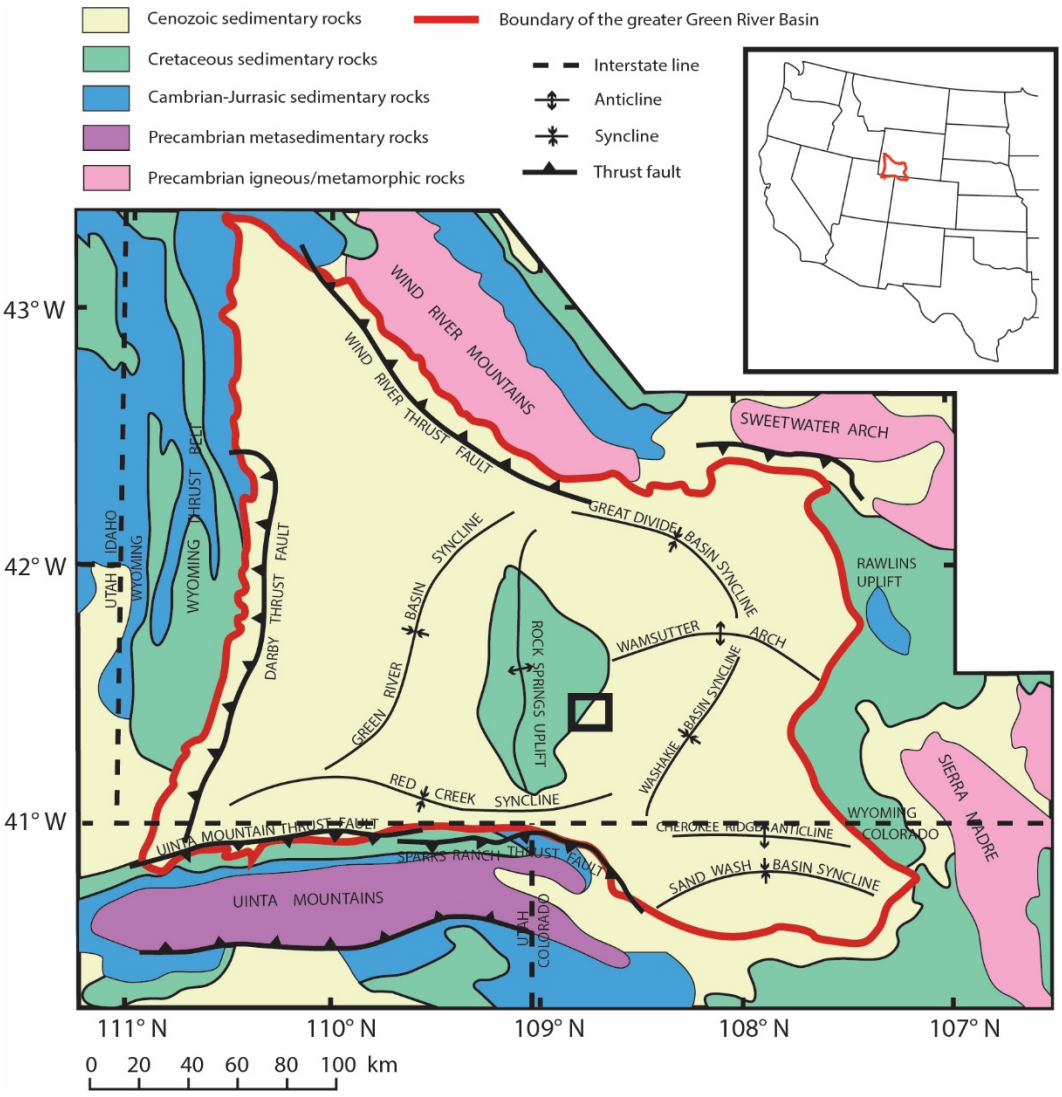

Figure 4-1 Location of the study area and major structural features in the Greater Green River Basin (Roehler, 1992). The black box represents the site of field work.

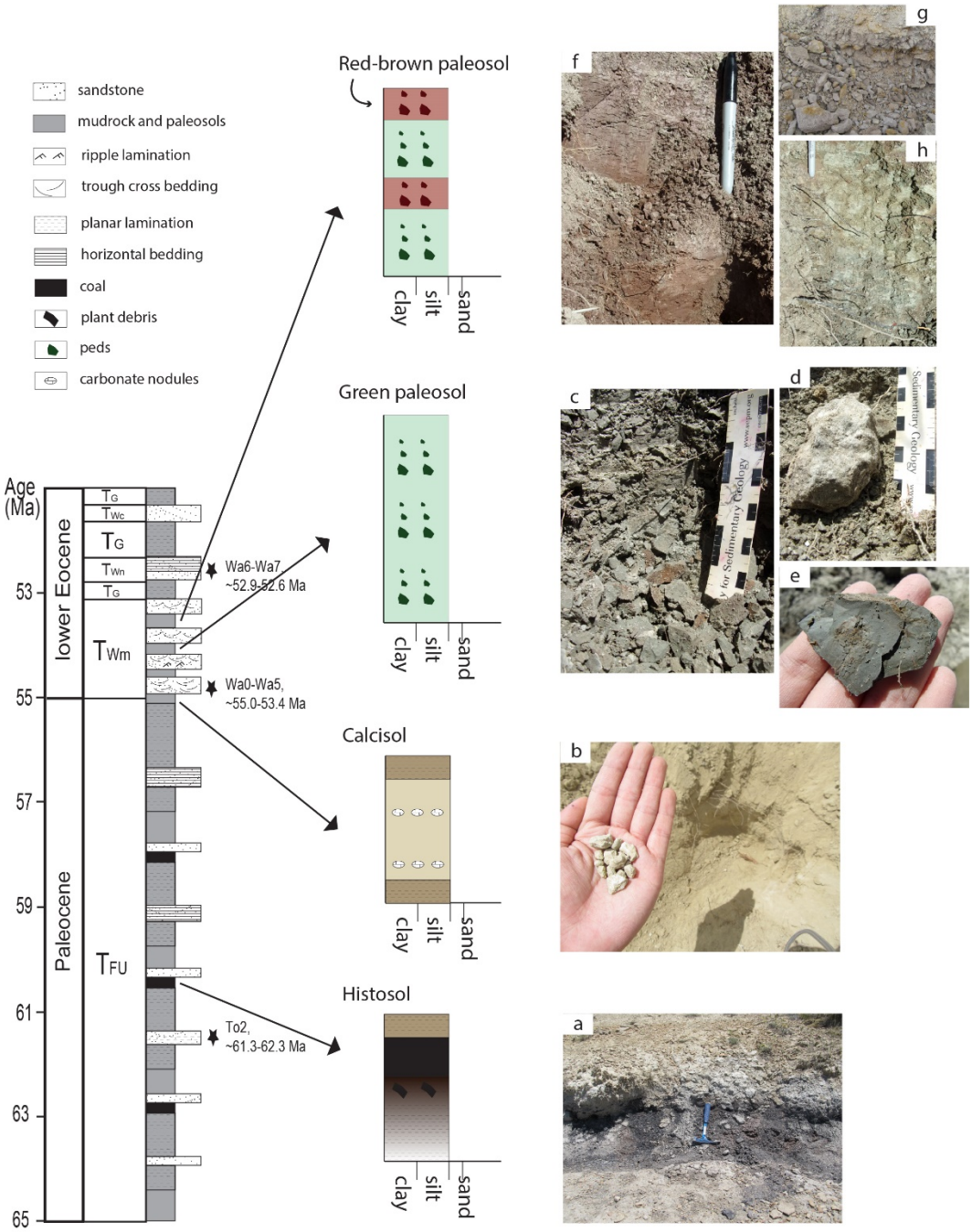

Figure 4-2 Typical paleosol types in the studied lower Paleogene strata. Field pictures: a), histosol (coal); b), calcisol showing small carbonate nodules; c) and e), peds with reddish coating in a green paleosol; d), carbonate accumulation (not a well-developed nodule) in a green paleosol; f), red paleosol; g) purple paleosol; h) green paleosol with blue mottled color. Nominations: T_{FU}, Fort Union

Formation; T_{Wm}, main body of the Wasatch Formation; T_{Wn}, Niland Tongue of the Wasatch Formation; T_{Wc}, Cathdrewl Tongue of the Wasatch Formation; T_G, Green River Formation. Numbers in circles next to the stratigraphic column represent the available land mammal fossil age constraints: ① Wa0-Wa5, ~55.0-53.4 Ma; ② Wa6-Wa7, ~52.9-52.6 Ma (see section 4.2.2).

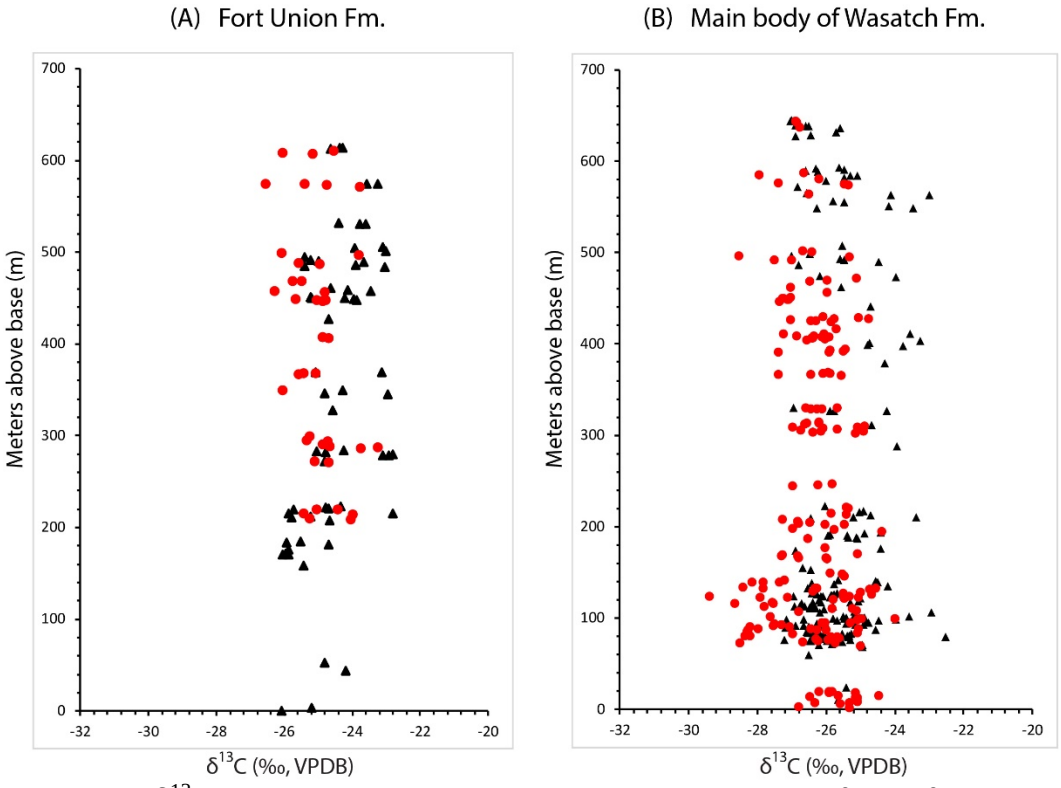

Figure 4-3 $\delta^{13}C_{org}$ values plotted versus height above the base of each formation. Red dots represent paleosol samples, black triangles represent mudstone samples.

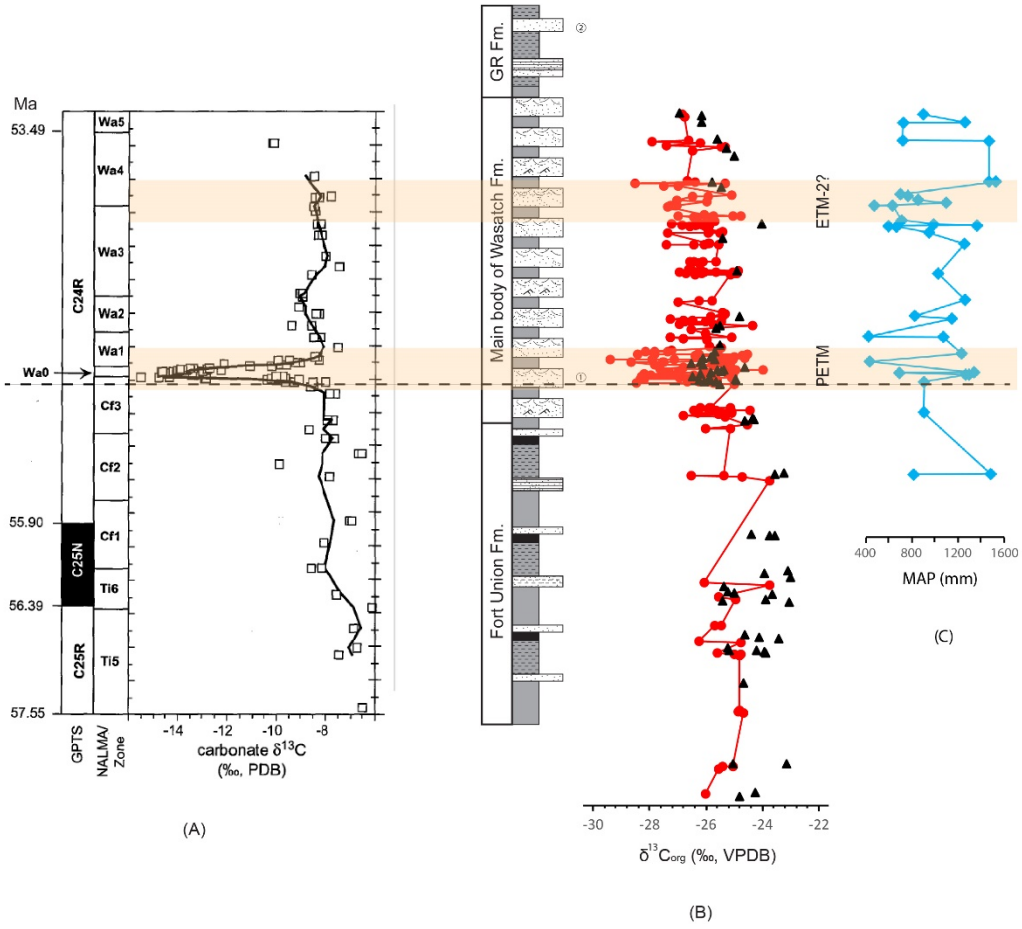

Figure 4-4 Carbon isotope record and MAP estimates for the late Paleocene-early Eocene hydroclimate. (A) Carbon isotope record from paleosol carbonates in the Bighorn Basin (Koch et al., 2003). (B) Carbon isotope record from bulk organic matter, this study, the data points for mudstone samples in Wasatch Formation are 5-point running averages of meter-level values. (C) MAP estimates, this study. Numbers in circles next to the stratigraphic column represent the available land mammal fossil age constraints: ① Wa0-Wa5, ~55.0-53.4 Ma; ② Wa6-Wa7, ~52.9-52.6 Ma (see section 4.2.2).

Table 4-1 Measured bulk organic carbon isotope ratios ($\delta^{13}C_{org}$)

paleosol			*mudstone*		
Formation	meter level (m)	$\delta^{13}C$ (‰)	Formation	meter level (m)	$\delta^{13}C$ (‰)
Fort Union	208.0	-24.0	Fort Union	0.0	-26.1
Fort Union	208.5	-25.2	Fort Union	3.2	-25.2
Fort Union	212.7	-24.0	Fort Union	44.0	-24.2
Fort Union	214.0	-25.4	Fort Union	53.0	-24.8
Fort Union	218.0	-24.4	Fort Union	158.0	-25.4
Fort Union	219.0	-25.0	Fort Union	170.0	-25.9
Fort Union	270.0	-24.7	Fort Union	170.5	-26.1
Fort Union	271.0	-25.1	Fort Union	171.5	-26.0
Fort Union	285.5	-23.7	Fort Union	176.0	-25.9
Fort Union	286.5	-23.2	Fort Union	181.0	-24.7
Fort Union	287.0	-24.6	Fort Union	183.5	-25.9
Fort Union	288.5	-24.7	Fort Union	185.0	-25.5
Fort Union	289.0	-24.9	Fort Union	207.5	-24.7
Fort Union	291.5	-24.7	Fort Union	211.3	-25.8
Fort Union	293.0	-24.7	Fort Union	212.0	-25.2
Fort Union	293.5	-25.3	Fort Union	215.0	-22.8
Fort Union	298.0	-25.2	Fort Union	215.5	-25.9
Fort Union	348.0	-26.0	Fort Union	220.0	-25.7
Fort Union	365.5	-25.5	Fort Union	221.0	-24.7
Fort Union	367.0	-25.4	Fort Union	221.8	-24.8
Fort Union	367.5	-25.1	Fort Union	222.5	-24.3
Fort Union	405.2	-24.7	Fort Union	271.5	-24.8
Fort Union	406.0	-24.8	Fort Union	278.0	-22.9
Fort Union	406.8	-24.8	Fort Union	279.0	-23.1
Fort Union	445.5	-24.8	Fort Union	279.5	-22.8
Fort Union	446.5	-24.8	Fort Union	282.2	-24.8
Fort Union	447.0	-25.0	Fort Union	283.0	-25.1
Fort Union	447.5	-25.6	Fort Union	284.5	-24.3
Fort Union	455.5	-24.8	Fort Union	328.0	-24.6
Fort Union	456.0	-26.3	Fort Union	345.5	-23.0
Fort Union	467.0	-25.7	Fort Union	346.0	-24.8
Fort Union	467.5	-25.5	Fort Union	349.3	-24.3
Fort Union	486.0	-24.9	Fort Union	369.0	-25.1

paleosol			*mudstone*		
Formation	meter level (m)	$\delta^{13}C$ (‰)	Formation	meter level (m)	$\delta^{13}C$ (‰)
Fort Union	487.0	-25.6	Fort Union	369.5	-23.1
Fort Union	496.0	-23.8	Fort Union	426.5	-24.7
Fort Union	498.0	-26.0	Fort Union	448.0	-23.9
Fort Union	570.0	-23.7	Fort Union	448.5	-23.9
Fort Union	572.5	-24.7	Fort Union	449.5	-25.2
Fort Union	573.0	-26.5	Fort Union	450.0	-24.2
Fort Union	573.5	-25.4	Fort Union	451.0	-25.2
Fort Union	606.5	-25.1	Fort Union	457.5	-23.5
Fort Union	607.0	-26.0	Fort Union	459.0	-24.1
Fort Union	609.0	-24.5	Fort Union	460.5	-24.6
Wasatch	1.0	-25.3	Fort Union	484.0	-23.1
Wasatch	2.0	-26.8	Fort Union	485.0	-25.4
Wasatch	6.0	-25.6	Fort Union	485.5	-23.9
Wasatch	6.5	-25.3	Fort Union	489.0	-23.7
Wasatch	7.0	-26.3	Fort Union	490.0	-25.0
Wasatch	8.0	-25.1	Fort Union	491.5	-25.2
Wasatch	12.0	-25.1	Fort Union	494.7	-25.4
Wasatch	12.5	-25.1	Fort Union	501.5	-23.0
Wasatch	14.0	-26.5	Fort Union	504.5	-23.9
Wasatch	14.5	-24.5	Fort Union	506.0	-23.1
Wasatch	15.0	-25.6	Fort Union	530.5	-23.6
Wasatch	17.5	-25.9	Fort Union	531.0	-23.8
Wasatch	18.0	-25.1	Fort Union	531.5	-24.4
Wasatch	18.5	-26.2	Fort Union	574.0	-23.6
Wasatch	19.0	-25.9	Fort Union	574.8	-23.2
Wasatch	19.5	-25.8	Fort Union	612.5	-24.6
Wasatch	68.8	-25.0	Fort Union	613.3	-24.3
Wasatch	72.0	-28.5	Fort Union	614.0	-24.4
Wasatch	72.5	-25.7	Wasatch	10.5	-25.7
Wasatch	73.3	-26.7	Wasatch	23.5	-25.4
Wasatch	74.8	-26.2	Wasatch	59.2	-26.5
Wasatch	75.5	-25.9	Wasatch	68.8	-24.9
Wasatch	77.0	-26.3	Wasatch	69.5	-25.0
Wasatch	77.7	-25.6	Wasatch	70.3	-25.0
Wasatch	78.5	-25.7	Wasatch	71.0	-26.2

paleosol			*mudstone*		
Formation	meter level (m)	$\delta^{13}C$ (‰)	Formation	meter level (m)	$\delta^{13}C$ (‰)
Wasatch	79.2	-25.8	Wasatch	71.8	-25.8
Wasatch	79.5	-28.2	Wasatch	73.5	-25.5
Wasatch	79.8	-28.3	Wasatch	73.8	-25.8
Wasatch	82.3	-27.0	Wasatch	74.0	-25.8
Wasatch	83.8	-28.3	Wasatch	74.3	-25.8
Wasatch	83.8	-25.1	Wasatch	74.5	-26.4
Wasatch	84.0	-28.3	Wasatch	74.8	-26.5
Wasatch	86.3	-26.0	Wasatch	75.0	-25.8
Wasatch	86.5	-26.3	Wasatch	75.3	-26.0
Wasatch	86.8	-26.0	Wasatch	75.5	-26.5
Wasatch	87.0	-28.3	Wasatch	75.8	-25.7
Wasatch	87.5	-28.0	Wasatch	76.0	-27.2
Wasatch	87.8	-25.0	Wasatch	76.3	-25.9
Wasatch	88.3	-26.4	Wasatch	76.5	-25.3
Wasatch	90.5	-27.1	Wasatch	77.0	-26.3
Wasatch	90.5	-28.2	Wasatch	77.3	-25.8
Wasatch	91.3	-27.5	Wasatch	77.8	-26.1
Wasatch	92.0	-27.3	Wasatch	78.5	-26.0
Wasatch	93.0	-27.5	Wasatch	78.8	-26.2
Wasatch	94.3	-26.1	Wasatch	78.9	-22.5
Wasatch	94.5	-25.3	Wasatch	80.0	-25.4
Wasatch	94.8	-26.0	Wasatch	80.3	-25.3
Wasatch	97.3	-25.1	Wasatch	80.5	-25.4
Wasatch	98.8	-25.0	Wasatch	82.3	-25.5
Wasatch	99.0	-24.0	Wasatch	82.5	-26.3
Wasatch	101.5	-27.6	Wasatch	82.8	-26.1
Wasatch	106.5	-26.8	Wasatch	83.0	-25.3
Wasatch	107.9	-25.1	Wasatch	83.3	-26.2
Wasatch	109.6	-25.2	Wasatch	83.5	-26.5
Wasatch	110.3	-25.8	Wasatch	84.3	-26.4
Wasatch	111.8	-27.8	Wasatch	84.5	-26.6
Wasatch	115.4	-28.7	Wasatch	85.3	-26.5
Wasatch	115.7	-27.5	Wasatch	86.7	-26.5
Wasatch	117.2	-27.5	Wasatch	87.3	-24.6
Wasatch	120.1	-25.8	Wasatch	89.5	-27.2

paleosol			*mudstone*		
Formation	meter level (m)	$\delta^{13}C$ (‰)	Formation	meter level (m)	$\delta^{13}C$ (‰)
Wasatch	120.8	-25.5	Wasatch	90.0	-26.5
Wasatch	121.6	-27.1	Wasatch	90.9	-26.2
Wasatch	122.3	-25.0	Wasatch	91.5	-26.7
Wasatch	122.5	-27.9	Wasatch	91.8	-26.9
Wasatch	122.8	-29.4	Wasatch	92.3	-26.1
Wasatch	123.0	-25.5	Wasatch	92.5	-25.2
Wasatch	123.8	-25.3	Wasatch	92.8	-26.0
Wasatch	125.8	-24.7	Wasatch	93.3	-24.9
Wasatch	126.5	-25.5	Wasatch	93.5	-26.3
Wasatch	127.2	-25.0	Wasatch	93.8	-25.4
Wasatch	128.8	-26.4	Wasatch	94.8	-24.8
Wasatch	131.3	-24.7	Wasatch	95.5	-26.0
Wasatch	131.8	-26.2	Wasatch	96.3	-24.9
Wasatch	132.0	-26.3	Wasatch	97.0	-24.5
Wasatch	132.3	-24.6	Wasatch	97.7	-25.7
Wasatch	132.5	-27.8	Wasatch	98.0	-27.2
Wasatch	133.0	-28.4	Wasatch	98.3	-24.0
Wasatch	138.5	-27.8	Wasatch	98.5	-26.7
Wasatch	138.8	-27.3	Wasatch	99.3	-25.5
Wasatch	139.0	-28.1	Wasatch	99.5	-25.8
Wasatch	140.8	-27.2	Wasatch	100.3	-24.9
Wasatch	145.7	-25.5	Wasatch	100.7	-25.2
Wasatch	147.7	-25.5	Wasatch	100.8	-25.4
Wasatch	148.3	-25.9	Wasatch	101.0	-25.0
Wasatch	164.2	-26.0	Wasatch	101.3	-23.6
Wasatch	165.0	-26.0	Wasatch	101.8	-25.5
Wasatch	165.8	-26.8	Wasatch	105.7	-22.9
Wasatch	167.3	-26.8	Wasatch	106.5	-26.2
Wasatch	168.0	-27.3	Wasatch	106.8	-25.2
Wasatch	168.8	-27.3	Wasatch	109.8	-26.1
Wasatch	169.5	-25.1	Wasatch	110.0	-26.5
Wasatch	177.0	-26.0	Wasatch	110.3	-26.3
Wasatch	186.2	-26.5	Wasatch	112.0	-26.5
Wasatch	194.5	-24.4	Wasatch	112.3	-26.4
Wasatch	196.7	-25.8	Wasatch	112.5	-26.6

paleosol			*mudstone*		
Formation	meter level (m)	$\delta^{13}C$ (‰)	Formation	meter level (m)	$\delta^{13}C$ (‰)
Wasatch	197.5	-27.0	Wasatch	112.8	-25.8
Wasatch	201.8	-25.5	Wasatch	113.0	-26.9
Wasatch	202.5	-26.0	Wasatch	113.3	-26.8
Wasatch	203.2	-26.8	Wasatch	115.9	-26.4
Wasatch	204.0	-26.5	Wasatch	116.2	-26.7
Wasatch	205.5	-26.8	Wasatch	116.4	-26.4
Wasatch	207.0	-27.3	Wasatch	116.7	-26.1
Wasatch	213.5	-25.4	Wasatch	116.9	-25.3
Wasatch	214.3	-25.8	Wasatch	117.7	-26.4
Wasatch	220.0	-25.4	Wasatch	118.4	-25.1
Wasatch	220.8	-25.4	Wasatch	118.9	-26.2
Wasatch	243.8	-27.0	Wasatch	122.0	-25.0
Wasatch	245.3	-26.2	Wasatch	123.1	-25.9
Wasatch	246.8	-25.8	Wasatch	123.8	-27.0
Wasatch	302.0	-25.1	Wasatch	124.0	-26.1
Wasatch	302.7	-26.4	Wasatch	124.3	-26.2
Wasatch	303.5	-24.9	Wasatch	124.8	-25.4
Wasatch	304.2	-26.1	Wasatch	125.0	-25.8
Wasatch	305.0	-26.7	Wasatch	125.3	-25.9
Wasatch	305.8	-25.0	Wasatch	125.5	-26.3
Wasatch	306.5	-25.7	Wasatch	125.9	-25.8
Wasatch	307.3	-26.1	Wasatch	126.8	-25.7
Wasatch	308.0	-25.1	Wasatch	127.0	-25.5
Wasatch	308.7	-27.0	Wasatch	127.3	-25.5
Wasatch	309.5	-24.9	Wasatch	127.5	-26.4
Wasatch	311.7	-26.6	Wasatch	132.8	-26.6
Wasatch	312.5	-26.2	Wasatch	135.2	-24.2
Wasatch	313.3	-26.5	Wasatch	137.5	-25.8
Wasatch	314.0	-26.2	Wasatch	138.3	-26.4
Wasatch	328.0	-26.3	Wasatch	139.7	-24.5
Wasatch	328.3	-26.1	Wasatch	140.3	-24.6
Wasatch	328.7	-26.4	Wasatch	141.3	-25.7
Wasatch	329.1	-26.6	Wasatch	153.0	-26.5
Wasatch	329.5	-25.7	Wasatch	155.0	-26.7
Wasatch	365.0	-25.6	Wasatch	174.0	-26.9

paleosol			*mudstone*		
Formation	meter level (m)	$\delta^{13}C$ (‰)	Formation	meter level (m)	$\delta^{13}C$ (‰)
Wasatch	366.0	-26.4	Wasatch	176.3	-24.4
Wasatch	366.5	-27.4	Wasatch	187.0	-25.1
Wasatch	367.0	-26.1	Wasatch	187.8	-25.1
Wasatch	367.5	-25.9	Wasatch	188.5	-25.4
Wasatch	368.0	-25.9	Wasatch	190.0	-26.0
Wasatch	390.5	-27.4	Wasatch	190.7	-25.4
Wasatch	391.0	-25.9	Wasatch	191.5	-25.9
Wasatch	391.5	-25.5	Wasatch	193.0	-24.9
Wasatch	392.5	-25.9	Wasatch	193.7	-24.4
Wasatch	393.5	-25.4	Wasatch	209.0	-26.5
Wasatch	404.0	-26.6	Wasatch	209.8	-23.4
Wasatch	405.0	-26.0	Wasatch	210.5	-25.2
Wasatch	406.0	-26.4	Wasatch	212.0	-24.7
Wasatch	406.5	-26.4	Wasatch	215.8	-25.0
Wasatch	407.0	-26.1	Wasatch	217.3	-24.9
Wasatch	407.5	-25.9	Wasatch	222.3	-26.0
Wasatch	408.0	-26.8	Wasatch	288.0	-24.0
Wasatch	408.5	-26.3	Wasatch	311.0	-24.7
Wasatch	410.0	-26.1	Wasatch	326.5	-24.2
Wasatch	410.5	-27.2	Wasatch	326.9	-25.8
Wasatch	416.0	-25.7	Wasatch	327.3	-25.9
Wasatch	424.0	-25.9	Wasatch	330.2	-26.9
Wasatch	424.5	-26.5	Wasatch	378.5	-24.3
Wasatch	425.0	-26.3	Wasatch	398.0	-23.8
Wasatch	426.0	-27.0	Wasatch	399.0	-24.8
Wasatch	427.0	-25.7	Wasatch	401.0	-24.7
Wasatch	427.5	-24.8	Wasatch	403.5	-23.3
Wasatch	428.0	-25.0	Wasatch	411.0	-23.6
Wasatch	429.0	-26.1	Wasatch	440.5	-24.7
Wasatch	446.0	-27.3	Wasatch	461.5	-25.6
Wasatch	448.0	-27.1	Wasatch	473.0	-24.0
Wasatch	448.5	-27.1	Wasatch	474.5	-26.2
Wasatch	449.0	-27.2	Wasatch	487.0	-26.8
Wasatch	449.5	-27.3	Wasatch	490.0	-24.5
Wasatch	450.0	-27.0	Wasatch	492.5	-25.5

paleosol			*mudstone*		
Formation	meter level (m)	$\delta^{13}C$ (‰)	Formation	meter level (m)	$\delta^{13}C$ (‰)
Wasatch	456.5	-26.0	Wasatch	493.5	-25.6
Wasatch	461.0	-27.0	Wasatch	496.0	-27.0
Wasatch	468.5	-26.5	Wasatch	499.0	-26.5
Wasatch	469.5	-26.0	Wasatch	507.0	-25.6
Wasatch	471.0	-25.1	Wasatch	548.2	-23.5
Wasatch	491.0	-27.0	Wasatch	549.0	-26.3
Wasatch	491.5	-27.5	Wasatch	550.5	-24.2
Wasatch	495.0	-25.3	Wasatch	555.0	-25.5
Wasatch	495.5	-28.5	Wasatch	556.5	-25.8
Wasatch	500.0	-26.4	Wasatch	562.5	-23.0
Wasatch	501.0	-26.7	Wasatch	563.2	-24.1
Wasatch	564.0	-26.5	Wasatch	565.5	-26.6
Wasatch	573.0	-25.3	Wasatch	571.5	-26.8
Wasatch	574.5	-25.5	Wasatch	579.0	-26.0
Wasatch	576.0	-27.4	Wasatch	582.0	-25.5
Wasatch	580.5	-26.2	Wasatch	583.5	-25.1
Wasatch	585.0	-27.9	Wasatch	584.3	-25.3
Wasatch	586.5	-26.6	Wasatch	588.8	-26.2
Wasatch	637.2	-26.8	Wasatch	589.5	-26.6
Wasatch	642.5	-26.8	Wasatch	590.3	-25.5
Wasatch	643.2	-26.9	Wasatch	591.8	-26.3
			Wasatch	592.5	-25.6
			Wasatch	627.0	-26.9
			Wasatch	628.5	-26.5
			Wasatch	631.5	-25.7
			Wasatch	636.5	-25.6
			Wasatch	638.0	-26.6
			Wasatch	638.7	-26.5
			Wasatch	639.5	-26.9
			Wasatch	640.0	-26.9
			Wasatch	641.0	-26.9
			Wasatch	644.0	-27.0
			Wasatch	645.5	-27.0

Table 4-2 Analyzed external standards used for calibration curve in Shimadzu EDX-7000 analyses of shales

	Certified/Preferred Values [a]			*Average (N = 5)* [b]						*Standard Deviation (N = 5)* [c]			*RSD (%)* [d]		
	SDO-1	**SBC-1**	**SGR-1**	**SDO-1**	**% error**	**SBC-1**	**% error**	**SGR-1**	**% error**	**SDO-1**	**SBC-1**	**SGR-1**	**SDO-1**	**SBC-1**	**SGR-1**
Na_2O	0.38	0.15	2.99	0.12	69.21	0.18	17.33	0.41	86.25	0.03	0.03	0.03	22.22	14.20	7.06
MgO	1.54	2.6	4.44	1.34	13.31	2.56	0.83	4.45	0.29	0.17	0.19	0.21	13.03	7.45	4.72
Al_2O_3	12.27	21	6.52	12.49	1.80	20.92	1.27	6.28	3.68	0.02	0.01	0.02	0.13	0.06	0.33
SiO_2	49.28	47.64	28.2	48.87	0.83	47.73	0.31	29.26	3.75	0.27	0.26	0.21	0.55	0.55	0.70
K_2O	3.35	3.45	1.66	3.27	2.39	3.54	5.66	1.71	2.89	0.04	0.04	0.03	1.16	1.07	1.70
CaO	1.05	2.95	8.38	1.46	39.05	2.63	3.87	8.35	0.32	0.001	0.001	0.000	0.068	0.038	0.000
TiO_2	0.71	0.855	0.253	0.72	0.70	0.85	2.37	0.26	1.98	0.02	0.03	0.01	3.36	3.30	4.65
Fe_2O_3	9.34	9.71	3.03	9.25	0.99	9.79	2.61	3.05	0.59	0.02	0.02	0.01	0.26	0.25	0.43

[a]USGS standards SDO-1 (Devonian Ohio Shale), SBC-1 (Brush Creek Shale), and SGR-1 (Green River Shale) were used.

[b]Accuracy: All of the results from the different runs are averaged here and their accuracy relative to their standard reference values is reported as % error. The percentage error for each element is calculated:

$$\%error = \frac{Difference\ between\ measured\ and\ certified\ concentration}{Certified\ concentration\ of\ the\ element} \times 100$$

[c]Standard Deviation: The standard deviation is calculated, where x_a is the average concentration, x is the element concentration, and n is the number of measurements, as follows:

$$\sigma = \frac{\sqrt{\sum(x - x_a)^2}}{n - 1}$$

[d]Precision: the precision of a sample with respect to each element is represented by the relative standard deviation (RSD), calculated as follows:

$$RSD\,(\%) = \frac{100\sigma}{x_a}$$

Table 4-3 Results of major elements weight percentages and calculated CIA-K, MAP

Formation	Meter level	MgO	Al_2O_3	SiO_2	K_2O	CaO	TiO_2	Fe_2O_3	Na_2O	CIA-K	MAP
	(m)	wt.%	wt.%	wt.%	wt.%	wt.%	wt.%	wt.%	wt.%		(mm)
Wasatch	7.0	1.74	12.11	57.36	2.23	4.60	0.44	4.71	0.12	72	912
Wasatch	72.0	2.96	11.58	68.00	2.98	3.53	0.43	4.47	0.97	72	913
Wasatch	87.0	3.06	14.40	60.26	4.56	1.07	0.61	7.84	0.87	88	1255
Wasatch	87.3	2.61	13.53	58.84	4.30	1.00	0.55	6.05	0.63	89	1283
Wasatch	91.3	3.13	10.09	63.32	2.13	5.73	0.37	3.43	1.13	60	714
Wasatch	92.0	2.39	13.30	76.63	3.38	0.86	0.48	3.30	0.49	91	1321
Wasatch	115.4	1.72	6.95	40.25	1.56	10.28	0.16	1.29	0.79	39	473
Wasatch	132.5	3.13	14.50	62.12	3.98	1.01	0.51	5.75	1.19	87	1222
Wasatch	168.0	2.84	11.08	69.50	2.35	1.76	0.49	3.68	1.00	80	1070
Wasatch	168.8	9.22	7.89	45.22	1.84	8.10	0.30	2.45	5.14	37	461
Wasatch	207.0	3.44	13.95	73.30	4.00	1.31	0.50	4.22	1.47	83	1142
Wasatch	212.8	3.67	11.51	64.30	2.66	4.00	0.48	4.16	1.48	68	839
Wasatch	246.8	2.41	11.07	74.04	1.80	1.04	0.44	2.73	0.48	88	1248
Wasatch	303.3	3.37	12.34	66.70	2.73	2.07	0.50	3.34	1.38	78	1031
Wasatch	366.5	2.66	12.84	69.43	2.98	1.21	0.51	4.67	0.60	88	1243
Wasatch	390.5	3.32	12.53	62.62	2.76	3.20	0.54	4.27	1.15	74	954
Wasatch	403.5	4.09	11.82	55.02	3.13	6.79	0.42	4.90	1.79	58	692

Formation	Meter level	MgO	Al_2O_3	SiO_2	K_2O	CaO	TiO_2	Fe_2O_3	Na_2O	CIA-K	MAP
	(m)	wt.%	wt.%	wt.%	wt.%	wt.%	wt.%	wt.%	wt.%		(mm)
Wasatch	405.0	4.33	10.19	53.51	2.49	7.06	0.38	4.25	2.01	53	627
Wasatch	406.0	2.34	12.70	70.43	2.85	0.65	0.50	4.62	0.51	92	1344
Wasatch	408.5	3.59	11.81	71.25	2.56	2.33	0.49	3.14	1.34	76	994
Wasatch	417.0	3.65	12.08	54.21	3.24	6.36	0.48	5.07	1.39	61	734
Wasatch	448.0	3.24	9.69	59.15	1.34	6.48	0.39	2.27	1.32	55	658
Wasatch	448.5	3.03	8.09	49.53	1.23	9.66	0.29	1.78	1.24	43	512
Wasatch	454.5	2.34	14.30	54.60	2.06	2.77	0.62	6.94	0.55	81	1093
Wasatch	460.5	1.17	2.78	bdl	bdl	0.00	bdl	0.00	1.23	69	865
Wasatch	469.5	2.79	11.82	65.44	2.03	5.68	0.41	3.14	0.88	64	785
Wasatch	472.5	2.74	11.80	58.72	2.25	6.88	0.41	3.36	0.96	60	722
Wasatch	499.5	1.12	11.50	65.74	1.78	0.34	0.56	8.27	0.00	97	1497
Wasatch	500.0	2.03	15.99	73.66	3.41	0.58	0.64	2.52	0.22	95	1443
Wasatch	586.5	1.85	13.58	70.40	3.07	0.41	0.57	6.38	0.27	95	1444
Wasatch	588.0	5.94	12.58	54.13	2.91	5.10	0.43	3.65	2.80	61	741
Wasatch	625.5	2.60	10.38	56.08	1.11	5.65	0.43	4.24	0.78	62	746
Wasatch	626.2	3.24	14.48	58.34	2.25	1.06	0.72	6.91	0.94	88	1249
Wasatch	643.2	3.63	12.26	64.72	1.64	3.40	0.54	3.92	1.41	72	910
Fort Union	573.0	1.49	13.96	46.01	1.43	6.73	0.35	2.63	0.05	67	832
Fort Union	573.5	2.49	16.54	70.59	3.28	0.39	0.57	3.14	0.35	96	1456

Chapter 5 Conclusions

This dissertation addresses the tectonic processes and continental hydroclimate during the Laramide deformation in the central Rocky Mountains, western U.S.A., with focus on the Greater Green River Basin in southwestern Wyoming. In Chapter 2, we used a 2D flexural basin subsidence modeling method to explore the mechanism and processes of the Laramide deformation in the entire central Rocky Mountains. In Chapter 3, we focused on one of the Laramide intermontane basins—the Greater Green River Basin—to study how the Sevier-Laramide transition during the latest Cretaceous to earliest Eocene influenced the evolution of sedimentary basins and the regional drainage patterns, and when and how high the basin-bounding Laramide mountain ranges were uplifted. In Chapter 4, we explored the continental hydroclimate in the Greater Green River Basin during the late Paleocene-early Eocene (LPEE), which is the most recent geologic analogue to future climate and environment when Earth's atmospheric CO_2 concentration (pCO_2) increases significantly due to fossil fuel burning.

In Chapter 2, we found that the stiffness of Wyoming lithosphere varied slightly in the studied basins, including the Powder River Basin, the Bighorn Basin, the Wind River Basin, and the Greater Green River Basin, during the ~30 Myr duration of the Laramide deformation, and spatially decreased from northeastern Wyoming (T_e=32–46 km) to southwestern Wyoming (T_e=6–9 km).

We attributed this southwestward weakening of the Wyoming lithosphere to the combined effect of bending stresses, crust–mantle decoupling and end loads. We also found that the increase of equivalent load height of major Laramide ranges accelerated during the early Eocene, and we attributed this acceleration to both dynamic and isostatic effects associated with slab rollback. Our modeling results agree with the two-stage history of Laramide deformation proposed by Fan and Carrapa (2014), and help elucidate the geodynamic processes that influenced the stiffness of the Wyoming lithosphere and thereby controlled the surface deformation patterns. During the Late Cretaceous, our study area was located in the foreland of the thin–skinned Sevier fold–and–thrust belt (e.g., Livaccari, 1991; DeCelles, 2004). During the latest Cretaceous–Paleocene, the intra–plate compressional strain induced by the low angle subduction of the Farallon oceanic plate caused the uplift of the Laramide mountain ranges, and the combination of the bending stresses induced by the topographic load of the Sevier fold–and–thrust belt, the crust–mantle decoupling initiated by the overthickened Sevier hinterland, and the end loads due to the low angle subduction of the Farallon oceanic plate at the western edge of the thick Wyoming craton, caused the southwestward weakening of Wyoming lithosphere. During the early Eocene, the rollback or removal of the flat slab (e.g., Liu et al., 2008; Liu et al., 2010; Liu and Gurnis, 2010) caused the acceleration of uplift by both dynamic and isostatic effects.

In Chapter 3, the results of our depositional environment, sediment provenance and oxygen isotope paleoaltimetry studies suggest that the high topography of the Uinta Mountains (>3.5 km) was established by 53 Ma, which was 4-6 Myr earlier than previously thought. The earliest Eocene surface uplift of the Uinta Mountains changed the drainage pattern in the southern Greater Green River Basin, with depositional changed from low-energy distal floodplain of a meandering river during the Paleocene to high-energy, braided rivers during the earliest Eocene, and Precambrian basement-derived feldspar grains sourced from the Uinta Mountains were dispersed into the basin by northward flowing rivers. Significant surface uplift of the Uinta Mountains caused precipitation with low $\delta^{18}O$ values during the earliest Eocene, and such water arrived the basin and was documented by the low $\delta^{18}O$ values of authigenic carbonate minerals. The results of this study put the timing of the establishment of high topography of the Uinta Mountains in the same period as the establishment of high topography of the Wind River Range (Fan et al., 2011), and the Bighorn Mountains (Fan and Dettman, 2009), supporting a previous hypothesis that the Laramide ranges experienced accelerated deformation during the late Paleocene-early Eocene (Fan and Carrapa, 2014; Gao et al., 2016).

In Chapter 4, a long and continuous carbon isotope record was built in the Greater Green River Basin using bulk organic matter in order to fill the gap of rare continental records for the warm LPEE climate. The Paleocene-Eocene

Thermal Maximum (PETM), which has been relatively well studied in limited localities including the Bighorn Basin in northern Wyoming and the Axehandle Basin in central Utah (e.g., Bowen et al., 2001; Koch et al., 2003; Bowen and Bowen, 2008), was identified in our record as a ~4 ‰ negative carbon isotope excursion (CIE). Our reconstructed atmospheric pCO_2 within the PETM based on the carbon isotope compositions of paleosol carbonates and accompanied organic matter is 600-1200 ppm, 2-3 times higher than the preindustrial value. Our reconstructed mean annual precipitation (MAP) using the chemical index of alteration without potassium (CIA-K) proxy indicate generally humid climate during the LPEE, and transient dry hyperthermals. This observation seems to support a previously proposed hypothesis that the moisture delivery to high latitudes was enhanced during the PETM due to decreased meridional temperature gradients, leading to dry conditions in the middle latitudes and wet conditions in the high latitudes (Pagani et al., 2006; Bowen and Bowen, 2008).

Biographical Information

Min Gao obtained her Bachelor degree in Geological Engineering from the Shandong University of Science and Technology in China in 2009, and her Master degree in Mineral Resources Prospecting and Exploration from the China University of Geosciences (Beijing) in 2012. She then furthered her doctorate education in Earth and Environmental Sciences under the supervision of Dr. Majie Fan at the University of Texas at Arlington. Her research involves field-based, laboratory, and numerical modeling approaches to unravel tectonic processes, basin evolutions, and associated climatic and environmental changes from sedimentary archives. The research tools she uses mainly include basin subsidence modeling, sedimentology and petrography, and stable isotope geochemistry.